17:00:28 OCA PAD INITIATION - PROJECT HEADER INFORMATION 01/19/94

Active

Project #: E-25-W41 Cost share #: Rev #: 0
Center # : 10/24-6-R8038-0A0 Center shr #: OCA file #:
Work type : RES
Contract#: AGMT DTD 940113 Mod #: Document : AGR
Prime #: NAS9-19011 Contract entity: GTRC

Subprojects ? : N CFDA:
Main project #: PE #:

Project unit: MECH ENGR Unit code: 02.010.126
Project director(s):
ABDEL-KHALIK S I MECH ENGR (404)894-3719

Sponsor/division names: JOHNSON RES & DEVELOPMT CO / SYMRNA, GA
Sponsor/division codes: 259 / 008

Award period: 940111 to 940711 (performance) 940711 (reports)

Sponsor amount	New this change	Total to date
Contract value	23,330.00	23,330.00
Funded	23,330.00	23,330.00
Cost sharing amount		0.00

Does subcontracting plan apply ?: N

Title: MANNED SPACECRAFT EXTERNAL THERMAL CONTROL USING THE JOHNSON TUBE HEAT PUMP

PROJECT ADMINISTRATION DATA

OCA contact: E. Faith Gleason 894-4820

Sponsor technical contact	Sponsor issuing office
BARBARA MCCORD (404)438-2201	LINDA MOORE (404)438-2201
JOHNSON RESEARCH & DEVELOPMENT CO. 1640 ROSWELL ST., SUITE J SMYRNA, GA 30080	JOHNSON RESEARCH & DEVELOPMENT CO. 1640 ROSWELL ST., SUITE J SMYRNA, GA 30080

Security class (U,C,S,TS) : U ONR resident rep. is ACO (Y/N): N
Defense priority rating : ? N/A supplemental sheet
Equipment title vests with: Sponsor GIT
TITLE TO EQUIPMENT NOT ADDRESSED IN GA TECH STANDARD AGREEMENT.
Administrative comments -
INITIATION OF SUBCONTRACT UNDER NASA PRIME.

GEORGIA INSTITUTE OF TECHNOLOGY
OFFICE OF CONTRACT ADMINISTRATION

NOTICE OF PROJECT CLOSEOUT

Closeout Notice Date 10/24/94

Project No. E-25-W41 Center No. 10/24-6-R8038-0A0

Project Director ABDEL-KHALIK S I School/Lab MECH ENGR

Sponsor JOHNSON RES & DEVELOPMT CO/SYMRNA, GA

Contract/Grant No. AGMT DTD 940113 Contract Entity GTRC

Prime Contract No. NAS9-19011

Title MANNED SPACECRAFT EXTERNAL THERMAL CONTROL USING THE JOHNSON TUBE HEAT PU

Effective Completion Date 940711 (Performance) 940711 (Reports)

Closeout Actions Required:	Y/N	Date Submitted
Final Invoice or Copy of Final Invoice	Y	
Final Report of Inventions and/or Subcontracts	Y	
Government Property Inventory & Related Certificate	N	
Classified Material Certificate	N	
Release and Assignment	Y	
Other	N	

Comments

Subproject Under Main Project No.

Continues Project No.

Distribution Required:

Project Director	Y
Administrative Network Representative	Y
GTRI Accounting/Grants and Contracts	Y
Procurement/Supply Services	Y
Research Property Managment	Y
Research Security Services	N
Reports Coordinator (OCA)	Y
GTRC	Y
Project File	Y
Other	N
	N

NOTE: Final Patent Questionnaire sent to PDPI.

E25-W41

JRDC-NAS-JT3

MANNED SPACECRAFT EXTERNAL THERMAL CONTROL USING THE JOHNSON TUBE™ HEAT PUMP

NASA SBIR Contract NAS 9-19011
Final Report

L. G. Johnson, B. N. McCord, and J. R. Muller

Johnson Research and Development Co., Inc.
1640 Roswell St., Suite J
Smyrna, GA 30080

and

S. I. Abdel Khalik, S. M. Ghiaasiaan, S. M. Jeter, and M.F. Dowling

George W. Woodruff School of Mechanical Engineering
Georgia Institute of Technology
Atlanta, GA 30332

July 9, 1994

SUMMARY

The goal of this research was to establish the practical feasibility of utilizing the Johnson Tube^{TM} heat pump (U.S. Patent 4,724,683) for external thermal control of manned spacecraft. The primary objectives were:

1. Develop detailed computer models to theoretically predict the behavior of the Johnson Tube^{TM} heat pump.
2. Perform parametric calculations using these models to predict the sensitivity of the Johnson Tube^{TM} heat pump performance to various parameters.
3. Construct a proof-of-concept experimental apparatus to test the actual performance of the device.

Theoretical and experimental work has been conducted to accomplish these objectives.

Two-phase thermal hydraulic models for flow in the nozzle, drift tube, and diffuser based on either a homogeneous equilibrium model, a dynamic slip model, or a fully separated flow model have been developed. These models have been incorporated into a general thermodynamic model of the Johnson Tube^{TM} heat pump.

Parametric studies have been performed to quantify the effects of various parameters on the performance of the Johnson Tube^{TM}. The results indicate that COPs near those for a Carnot cycle can be theoretically achieved. The actual performance is significantly affected by both frictional losses in the system and the heat transfer effectiveness in the regenerator section.

An experimental facility has been constructed to test component performance. The data show an increase in temperature drop across the nozzle with increasing inlet temperature, as predicted theoretically. However, while the model predicts a slight increase in temperature drop with decreasing inlet pressure, the experiment yielded the opposite results. The latter is attributed to other than homogeneous behavior of the working fluid.

A proof-of-concept experimental facility has been constructed and tested. Experimental results showed that homogeneous flow is critical to the performance of the Johnson Tube^{TM}. Enhanced heat transfer in the regenerator section is necessary to achieve the desired operation of the device. To approach Carnot efficiency the device must be improved by optimizing the various Johnson Tube^{TM} components in accordance with model predictions. Enhancement of the regenerator heat transfer will be necessary to approach Carnot efficiency.

In conclusion, extensive theoretical analyses have shown the Johnson Tube^{TM} heat pump to be a highly efficient device, suitable for external thermal control of manned spacecraft. Experimental results suggest that various components must be optimized to achieve the desired operation of the device. The work outlined in the Phase II proposal is crucial to enhance the Johnson Tube^{TM} heat pump performance to approach the ideal Carnot efficiency. The device can be adapted for use in space for thermal control and refrigeration. In addition, the device has widespread applications for commercial and residential space conditioning and refrigeration.

TABLE OF CONTENTS

LIST OF TABLES

LIST OF FIGURES

I. INTRODUCTION AND PURPOSE OF WORK

I.A. Conventional Vapor Compression Systems

The Carnot cycle offers maximum thermodynamic efficiency for a heat engine operating between two temperatures [1]. However, the vapor compression cycle is traditionally treated as the ideal cycle for practical heat pumps and refrigerators because of the multiple barriers to a practical Carnot cycle. A primary limitation to a practical Carnot cycle has been the virtual inability to mechanically compress or expand (at a reasonable rate and efficiency) a mixture of liquid and vapor [1]. The vapor compression cycle circumvents these problems; however, it has a relatively low coefficient of performance (COP). This inefficiency occurs because the vapor is compressed well into the superheat region. In addition much of the heat rejection takes place above the condensing temperature and consequently well above the heat sink temperature. The vapor compression cycle also makes no attempt to regain work from the expanding fluid.

In addition to the relatively low COP of vapor compression systems, R-12, the standard refrigerant commonly used in such systems, must be phased out by the year 2000 (Montreal Protocol 1987) due to environmental concerns related to ozone depletion. The new refrigerant R-134a, which will replace R-12, is nonazeotropic, but has a global warming potential 420 times that of CO_2 [2]. Therefore, environmentally compatible classes of working fluids and/or alternative refrigeration technologies must be developed.

The Johnson Tube^{TM} heat pump (U.S. Patent 4,724,683) [3] is an innovative device which promises significant improvement over existing heat pump technology due to its high efficiency and simplicity. More importantly, it can be operated with a wide range of working fluids, including water, eliminating the need for ozone-depleting chlorofluorocarbons (CFCs) and other replacement refrigerants with high global warming potential. It can potentially replace devices which use the vapor compression cycle for future heat pump, refrigeration, and space conditioning applications. The goal of the present research is to establish the practical feasibility of utilizing the Johnson Tube™ heat pump for external thermal control of manned spacecraft.

I.B. The Johnson Tube™ Heat Pump

Figure 1 schematically depicts the key features of the Johnson Tube™ heat pump as utilized in a conceptual refrigeration cycle. The thermodynamic states of the fluid are depicted in Figure 2. The device consists of a pump, a convergent-divergent nozzle, a drift tube, a convergent-divergent diffuser, and an annular regenerative heat exchange channel which jackets the drift tube.

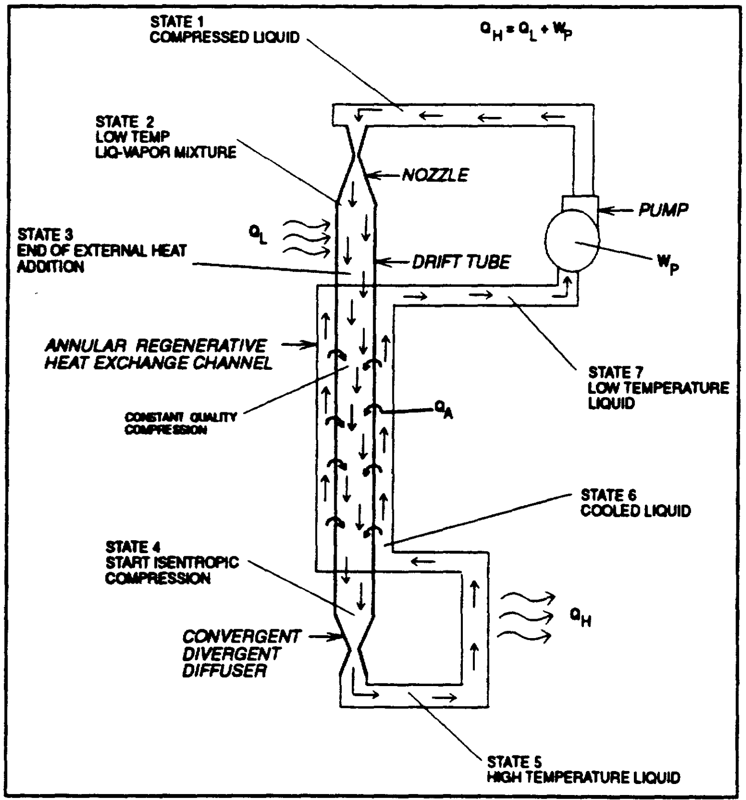

Figure 1: *Johnson Tube™ Heat Pump*

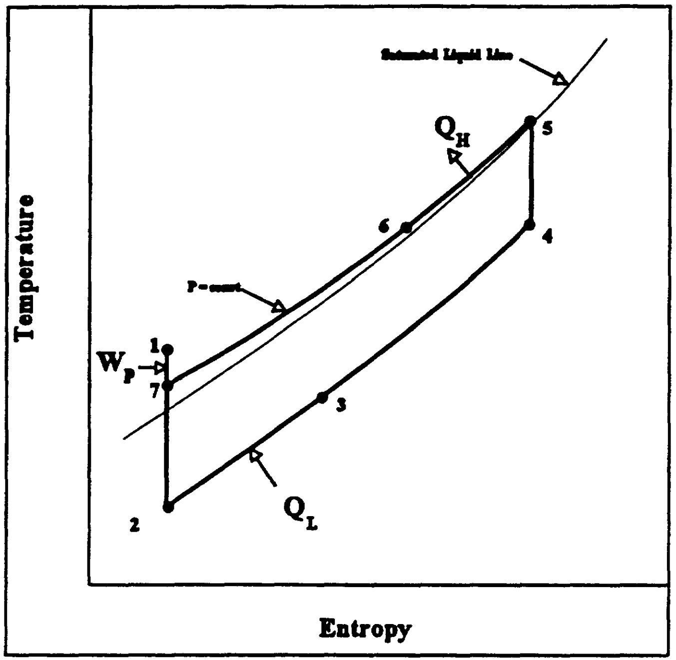

Figure 2: *Temperature-Entropy Diagram for Johnson Tube™ Heat Pump*

Referring to Figure 2, the main processes in an ideal Johnson Tube™ heat cycle are:

1. **Isentropic compression of a single phase liquid in the pump from State 7 to State 1.**

2. **Isentropic expansion, acceleration and flashing in the nozzle from State 1 to State 2.**

   The working fluid in a high-pressure liquid state (State 1 in Figure 2) jets through the nozzle, where it undergoes decompression, flashing, and acceleration. The working fluid temperature is significantly decreased as its velocity is increased. In a properly designed nozzle, flashing produces a homogeneous mixture of liquid and vapor (State 2). Thus, the two phase mixture exiting the nozzle will be a low quality, low pressure, cooled mixture with high kinetic energy (velocity). (See Figure 3).

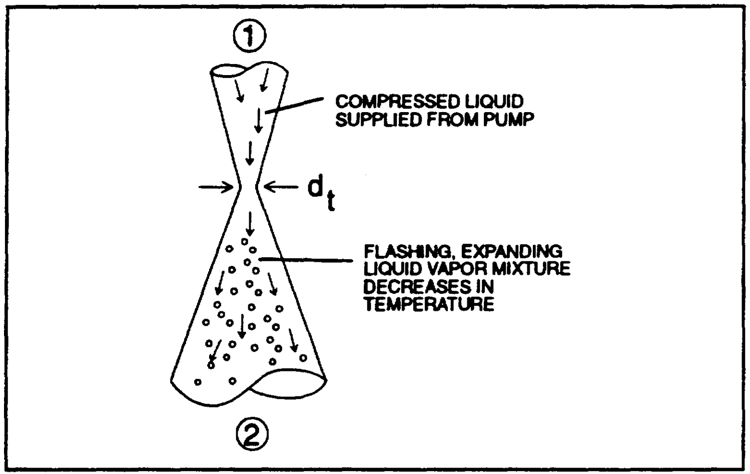

Figure 3: *Isentropic Acceleration and Flashing in the Nozzle*

3. **External thermal load addition at nearly constant quality from State 2 to State 3.**

   The low temperature vapor-liquid droplet mixture (State 2) absorbs the thermal load, Q_L, (i.e. from the refrigerated compartment in a chiller) reaching State 3. It is possible for the heat addition process to be performed in a manner that maintains nearly constant quality between States 2 and 3; the pressure and temperature at State 3 will be higher than those at State 2. Another, more favorable option for the heat addition process is to integrate it within the latter part of the nozzle expansion process. In this case, the temperature (and pressure) at States 2 and 3 would be the same. (See Figure 4).

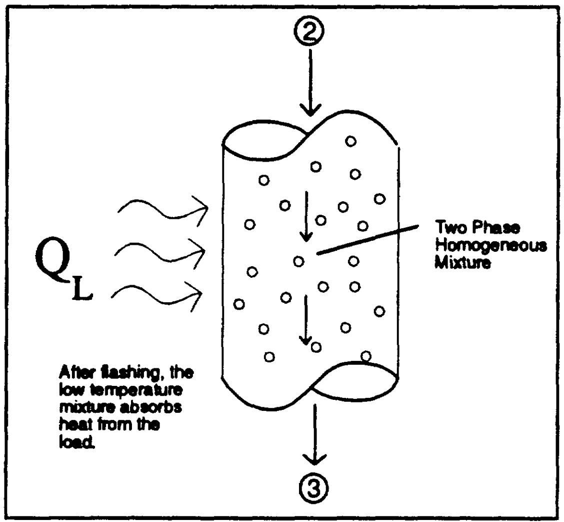

Figure 4: *External Thermal Load Addition*

4. Regenerative heat exchange in the drift tube from State 3 to State 4.

The two-phase mixture flows through the drift channel (diffuser) which also acts as a counter-current heat exchanger. The two-phase mixture flowing inside the drift channel is heated by the counter-flowing liquid within the annular jacket. Simultaneously, the mixture is decelerated and compressed towards State 4 (see Figure 5). The drift channel configuration can be chosen for optimal heat transfer and compression by the deceleration (diffusion) process. One possible method would hold the vapor quality in the two-phase mixture approximately constant between States 3 and 4, so that the thermal energy transferred to the mixture results in an increase in its pressure without further vaporization.

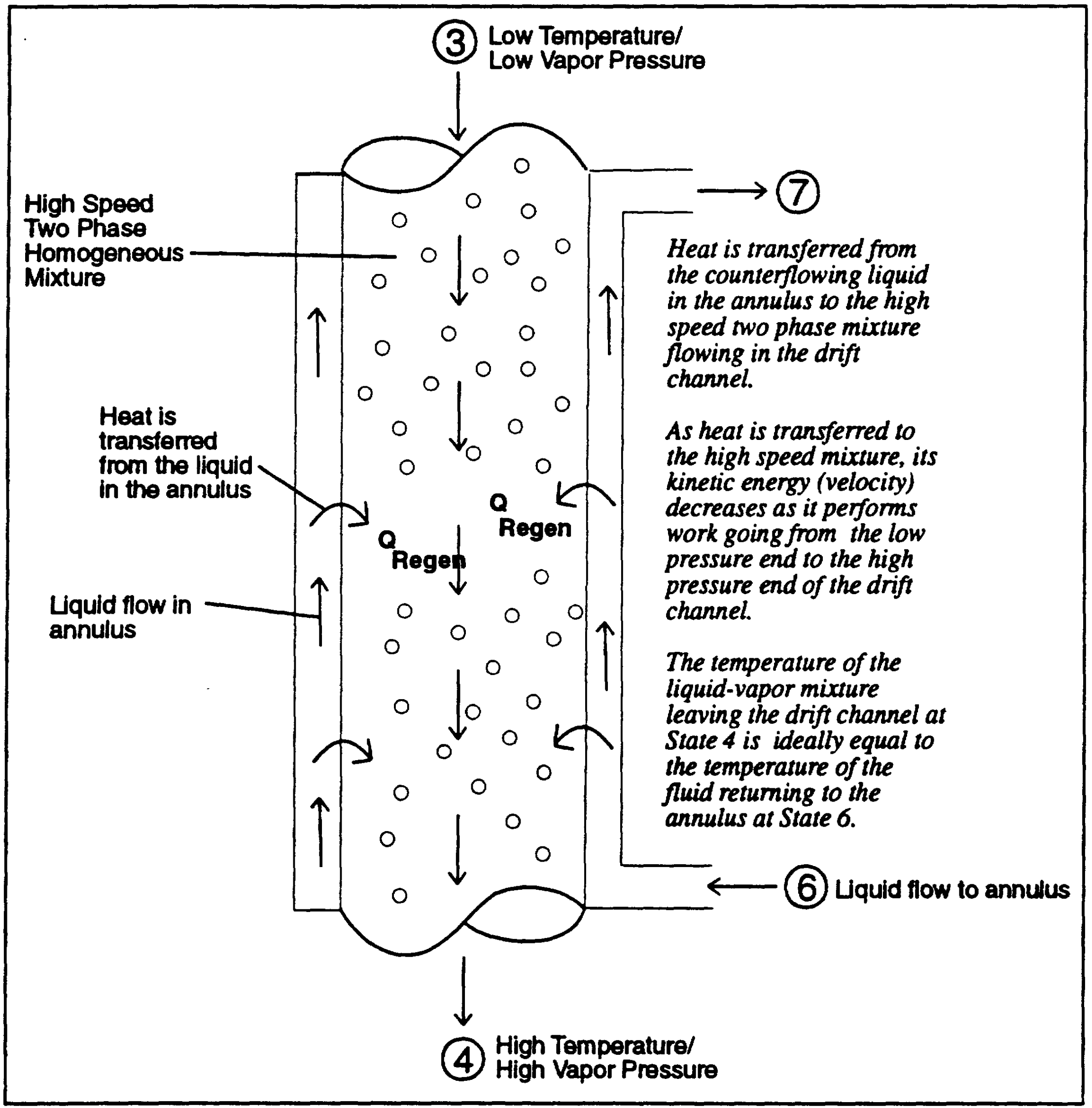

Heat is transferred from the counterflowing liquid in the annulus to the high speed two phase mixture flowing in the drift channel.

As heat is transferred to the high speed mixture, its kinetic energy (velocity) decreases as it performs work going from the low pressure end to the high pressure end of the drift channel.

The temperature of the liquid-vapor mixture leaving the drift channel at State 4 is ideally equal to the temperature of the fluid returning to the annulus at State 6.

Figure 5: *Regenerative Heat Exchange in the Drift Tube*

5. Complete condensation and deceleration in the isentropic diffuser from State 4 to State 5.

The final segment of the drift channel (between States 4 and 5) is an isentropic diffuser. In this section, the fluid is fully decelerated and condensed, resulting in increased pressure and temperature. The temperature rise of the liquid is a consequence of the latent heat released during the condensation process. Residual kinetic energy of the fluid is recovered as potential energy as the fluid's velocity decreases and its pressure increases in the diffuser. (See Figure 6).

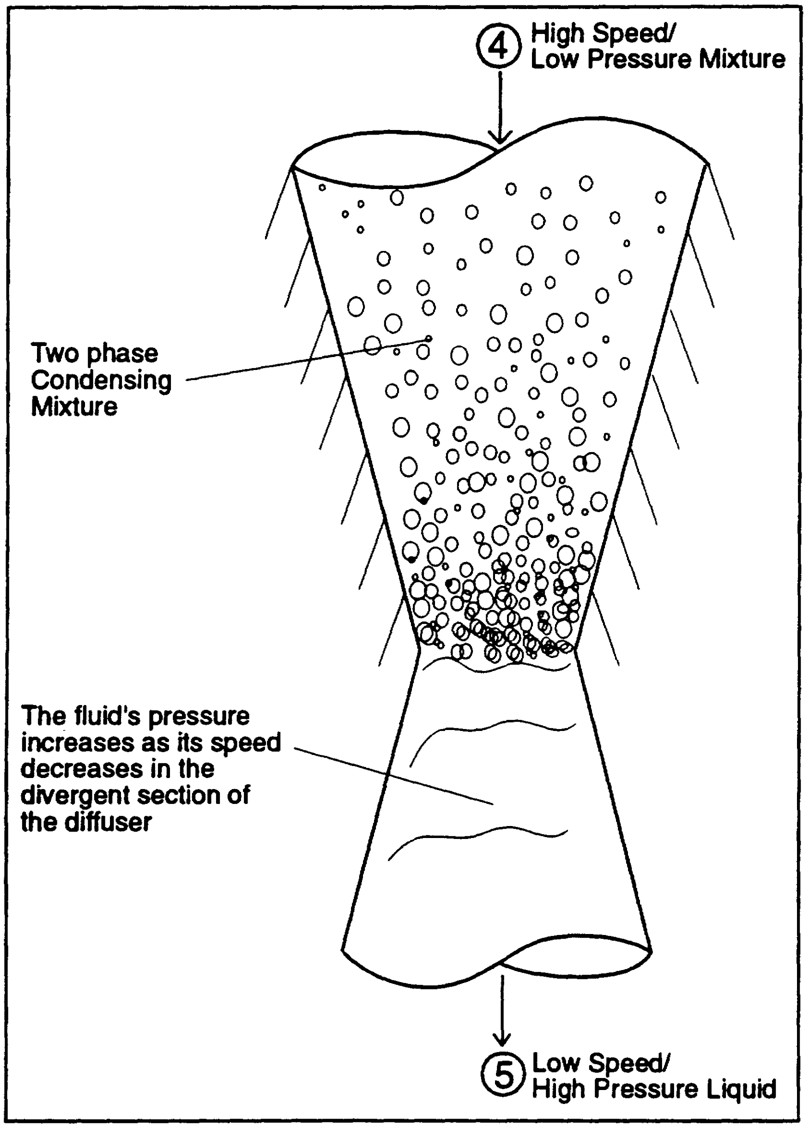

Figure 6: *Complete Condensation and Deceleration in the Isentropic Diffuser*

6. **Heat rejection to the environment at constant pressure from State 5 to State 6.**

   The warm liquid exiting the diffuser is cooled by the heat sink (the ambient for a chiller or the interior for a heat pump), rejecting Q_H and reaching State 6. (See Figure 7).

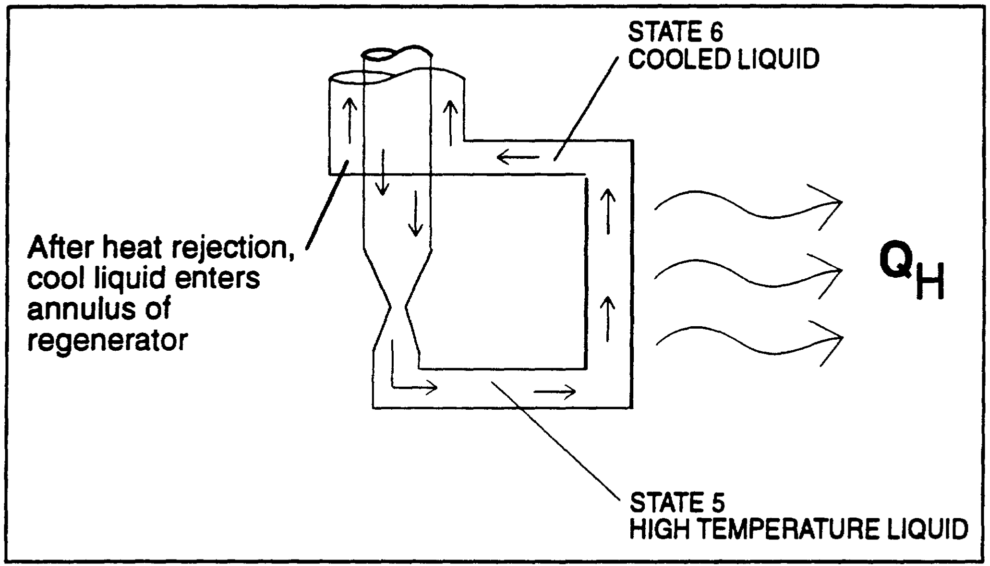

Figure 7: *Heat Rejection to the Environment*

7. **Regenerative constant pressure heat exchange from State 6 to State 7.**

   As illustrated in Figure 5, the liquid working fluid leaving the heat rejection process (State 6) is further cooled as it flows up through the outside of the annular jacket, transferring heat to the two-phase mixture within the drift channel. The fluid reaches the pump inlet (State 7), completing the cycle.

I.C. Discussion

In contrast to the vapor compression cycle, recuperative heat exchange in the Johnson Tube^{TM} heat pump confines external heat input to temperatures just below the heat source temperature and heat rejection to temperatures just above the heat sink temperature. This favorable temperature profile combined with the recovery of kinetic energy from the expanding fluid yields a cycle that approaches the efficiency of the Carnot cycle without its practical difficulties. Friction and irreversibilities are expected to have a relatively comparable impact on both the vapor compression cycle and the Johnson cycle. Therefore, the efficiency improvement of an actual Johnson Tube™ heat pump over existing systems should be roughly equivalent to the improvement of an ideal Carnot over an ideal vapor compression cycle operating between the same two temperatures. The physical configuration of this device also offers greater flexibility in selecting working fluids (i.e. few critical mechanical or electrical components need be immersed in the fluid and sealing and tribological concerns are minimized since there is no vapor compressor).

II. SPECIFIC GOALS OF WORK

The objective of the present research is to determine the practical engineering feasibility of utilizing the Johnson Tube™ heat pump concept for external thermal control of manned spacecraft. The following specific goals were developed to accomplish that objective:

1. Develop a general one-dimensional computer model for the heat transfer and flow characteristics of the two-phase liquid/vapor mixture in the drift tube and the combined performance of the drift tube and heat exchanger.
2. Perform parametric calculations using the computer code developed above to quantify the effects of various design and operational parameters, including nozzle characteristics, on the performance of the drift tube and heat exchanger.
3. Develop a general thermodynamic computer model for the Johnson Tube™ heat pump which includes non-ideal processes.
4. Perform parametric calculations using the above models to evaluate the sensitivity of the Johnson Tube™ heat pump performance to various design and operational parameters. Determine overall cycle performance and operating characteristics.
5. Design, construct and instrument a proof-of-concept test apparatus.
6. Develop a test plan and run tests. Evaluate data as obtained. Compare experimental data with performance predicted by computer models developed above.
7. Determine whether device is feasible for thermal control in manned spacecraft.

Theoretical and experimental work has been performed to accomplish the above objectives. Theoretical work is described in Section III, while the experimental work is presented in Section IV; the results are presented in Sections V and VI, respectively. Conclusions derived from the Phase I effort are presented in Section VII.

III. THEORETICAL WORK

III.A. Two-Phase Flow Models

Detailed state of the art two-phase thermal-hydraulic models for flow in the various components of the Johnson Tube™ have been developed. In addition, an overall thermodynamic model for the entire cycle including non-ideal processes has been developed. The two-phase models are described in Section III.A, while the thermodynamic model is presented in Section III.B below.

III.A.1. Introduction

The operation of the Johnson Tube™ involves complex two-phase flow processes. Experience with multi-fluid systems, such as water cooled reactors in recent years has shown that, in dealing with complex systems, first-principle modeling is the best approach. Large computer system codes based on first-principle modeling of transients in nuclear reactor systems have been remarkably successful in predicting experiments [9,10,11]. Mechanistic models also provide useful tools for parametric and sensitivity calculations, identification of key physical parameters governing the model processes, scaling, designing experimental test matrices, and analysis of experimental data.

In what follows, models for flow in the nozzle of the Johnson Tube™ are discussed in Section III.A.2. Two-phase flow conservation equations are then presented in Section III.A.3, where the homogeneous equilibrium mixture (HEM) model is presented in Section III.A.3.a, followed by the discussion of the seven and six-equation separated flow models in Sections

III.A.3.b and III.A.3.c, respectively. Conservation equations for the dynamic slip model are presented in Section III.A.3.d.

The constitutive and closure relations needed for the solution of these conservation equations are discussed in Section III.A.4. Thus, wall friction and heat transfer are addressed in Sections III.A.4.a and III.A.4.b, respectively, followed by a discussion of flow regimes in Section III.A.4.c. Liquid-vapor interphase forces are then discussed in Section III.A.4.d, followed by a discussion of interphase heat and mass transfer in Section III.A.4.e. Thermodynamic relations and properties are discussed in Section III.A.4.f. Finally, the numerical solution method is presented in Section III.A.5.

III.A.2. Nozzle flow models

The nozzle in the Johnson Tube™ is designed to support critical (choked) flow of an initially compressed (subcooled) liquid. This choked flow is accompanied by flashing and atomization of the fluid.

Two-phase critical flow has been extensively studied in the past, primarily due to its important role during loss-of-coolant-accidents in nuclear reactors. Models, with various levels of mechanistic details, have been suggested by many authors. The key parameter to predict in these models is the critical mass flux. The existing critical flow models can be divided into three broad groups. The first group of models are based on simple thermodynamic analyses, and do not account for any form of non-equilibrium [6,7,12]. These models are evidently appropriate for rough estimates. Models in the second group combine thermodynamic and fluid mechanical representations, and account for thermal and/or mechanical non-equilibrium [4,5,13]. These semi-empirical models have been particularly popular and successful. The third, and most recent group of models attempts to predict the critical flow rate by obtaining the relevant limiting solutions for the flow conservation equations [14,15]. These models, although based on sound theory, do not appear to be more accurate than the second group of models in predicting experimental data. Furthermore, they are computationally expensive.

In this work, three different algorithms for calculating the critical flow are provided as options. The first, the homogeneous equilibrium isentropic model(referred to in reference [11] as the "isoenthalpic" model), is the simplest and most consistent thermodynamic model. The second model, due to Henry and Fauske [5], belongs to the above-described second group of critical flow models, and is among the most widely-used methods for calculating two-phase choked flow. Both of these models are applied using empirical, polynomial-type curvefits for water-steam mixtures borrowed from [11], as will be discussed later. The third, due to Leung and Grolmes [7], provides a fast and approximate algorithm for calculating two-phase critical flow based on the homogeneous equilibrium isentropic model. These models are briefly described in the following paragraphs.

The homogeneous equilibrium isentropic model assumes: (a) the flow through the nozzle is isentropic, and (b) should the flow become two-phase, the liquid and vapor phases remain saturated with respect to the local pressure. The isentropic flow assumption is applied to the mixture, and not to either phase separately. This model, being based on equilibrium thermodynamic analyses, is conservative. It is, however, self consistent, is applicable to all fluids, and its range of applicability is unlimited.

The Henry-Fauske model [5] can be applied to the critical flow of an initially saturated liquid through a nozzle. This model assumes: (a) liquid and vapor do not exchange heat and mass while flowing through the nozzle throat, (b) each phase undergoes an isentropic expansion. Liquid and vapor are assumed to have different velocities, and the slip ratio at the throat is found by assuming that the derivative of the slip ratio with respect to pressure is zero at the throat. The model has been extended to include initially subcooled liquid as well [11].

The model of Leung and Grolmes [7] addresses the flashing critical flow of an initially subcooled liquid through a nozzle. It is based on the assumption of isentropic, homogeneous and equilibrium two-phase flow. However, by using an approximate equation of state for the saturated two-phase mixture, an approximate closed form solution is obtained for the critical flow rate.

Application of either of the isentropic or the Henry-Fauske models in their original forms involves iterative solution of several equations, accompanied with calculation of thermodynamic properties. Such calculations are obviously computationally expensive. In order to reduce computations, the developers of the computer code RETRAN [11] have devised curvefits for the predictions of the above three models, deriving explicit empirical correlations for water, in the following generic form:

$$G_{cr}=f(P_0,\hat{h}_0) \tag{1}$$

where G_{cr} is the critical mass flux at the throat,and P_0 and $\hat{h}_0$ represent the stagnation pressure and enthalpy at the nozzle inlet, respectively. The functions representing the right hand side of the above equation are in polynomial form. These empirical correlations, it is emphasized, are only applicable to water.

The empirical correlations of RETRAN-03 [11] are utilized in this work for calculating the critical nozzle flow for water. As mentioned earlier, the aforementioned "isoenthalpic" and Henry-Fauske models are both included.

III.A.3. Conservation equations

The analysis represented by the conservation equations to be described below starts from the throat of the nozzle, where z = 0 (see Figure 8). The flow is assumed to be steady and one-dimensional everywhere. The conservation equations are written for variable cross-sectional flow area [16,17], in accordance with the design features of the Johnson Tube™. The assumption of one-dimensional flow is realistic since, as noted elsewhere in this report, the drift channel is composed of long tubular components with only mild variations of flow cross-sectional area in the drift channel segment.

Except for the homogeneous equilibrium mixture model, The working fluid is assumed to contain a small amount of noncondensible gas. The liquid phase is assumed impermeable to the noncondensible gas. Furthermore, the noncondensible gas is assumed to remain locally well-mixed and at thermal equilibrium with the vapor.

The segment of the Johnson Tube™ where the drift tube is jacketed by the countercurrent liquid flow channel represents a countercurrent heat exchanger. The energy conservation equations representing the two countercurrent streams are thus coupled, and must be numerically solved simultaneously.

III.A.3.a. Homogeneous equilibrium mixture (HEM) model

Figure 8 is a schematic of the drift tube. The mass conservation equation for the two-phase mixture conservation equations can be represented as (see Nomenclature for the definition of parameters):

$$\frac{d}{dz}(\rho_h UA) = 0 \tag{2}$$

the mixture momentum equation is:

$$-\frac{dP}{dz}=\rho_h g\sin\theta+F_{WM}+\frac{1}{A}\frac{d}{dz}(\rho_h U^2 A) \tag{3}$$

where θ is the angle of inclination with respect to the horizontal plane, defined positive when flow is upward.

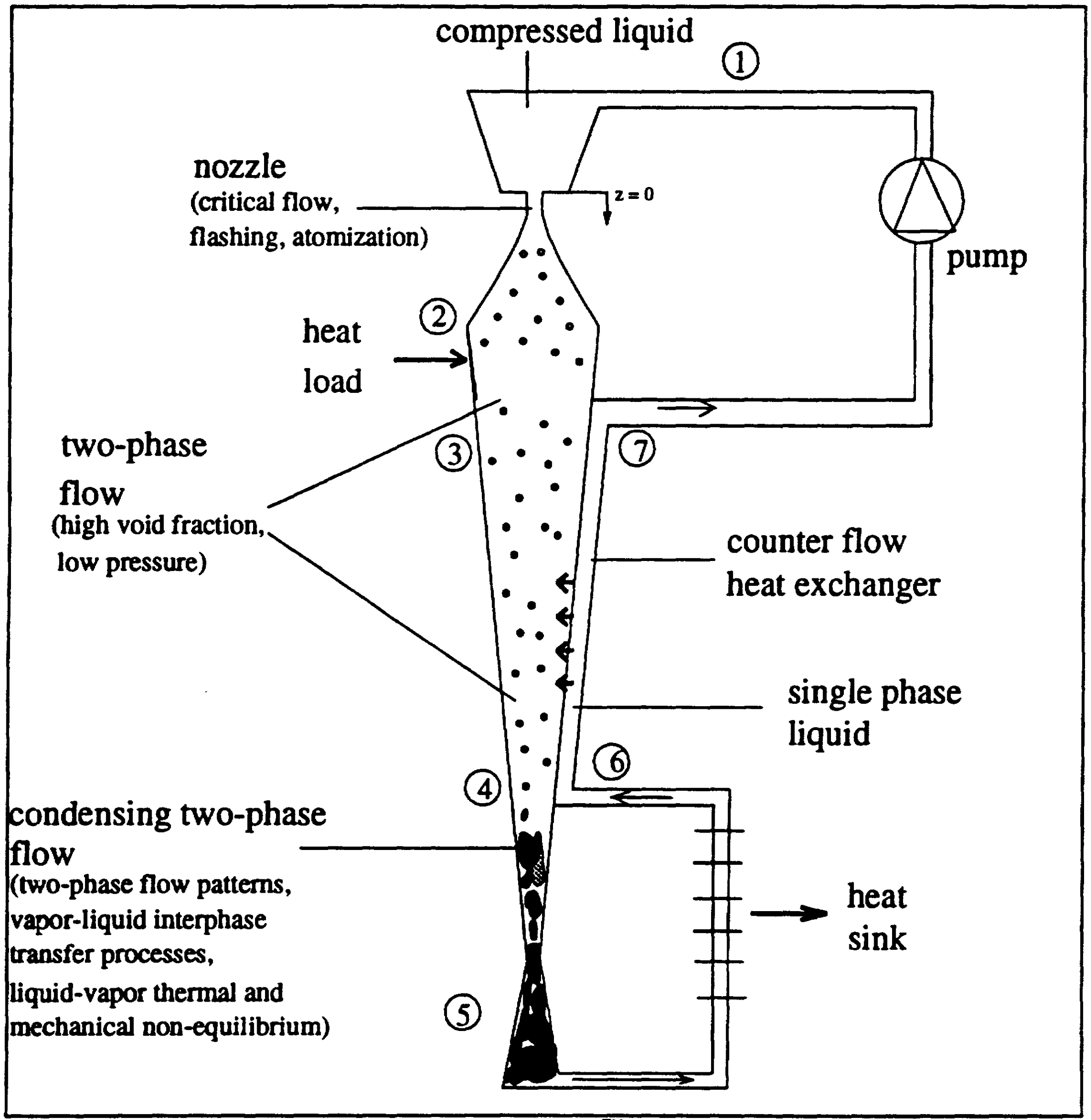

Figure 8: *Johnson Tube™ Heat Pump Cycle*

The homogeneous mixture density is defined as:

$$\rho_h = \left[\frac{x}{\rho_g} + \frac{(1-x)}{\rho_f} \right]^{-1} \tag{4}$$

The energy conservation equation for the drift channel can be written as:

$$\rho_h U \frac{de}{dz} = \frac{\wp}{A} q'' \tag{5}$$

where e represents the total enthalpy, defined as:

$$e = x\hat{h}_g + (1-x)\hat{h}_f + \frac{1}{2}U^2 \tag{6}$$

The parameter q" is the heat flux, i.e. heat flow rate per unit surface area, provided to the channel. Referring to Figure 8, it thus represents the heat load in the segment between Points 2 and 3, and the heat transfer between the fluid in the drift channel and the liquid in the jacket between Points 3 and 4. Between the latter two points, Equation (5) should be solved simultaneously with the energy conservation equation for the fluid in the jacket:

$$\dot{m}_{tot} c_{P,L} \frac{dT_{L,J}}{dz} = \wp q'' \tag{7}$$

III.A.3.b. Seven-equation separated flow model

In this approach, the liquid and gas phases are represented by separate mass, momentum, and energy equations, and thermal and mechanical nonequilibrium are both rigorously accounted for.

The two-phase mixture mass conservation equation is written as:

$$\frac{d}{dz}\{[\alpha\rho_G U_G+(1-\alpha)\rho_L U_L]A\}=0 \tag{8}$$

Mass conservation for the vapor-noncondensible mixture is represented by:

$$\frac{1}{A}\frac{d}{dz}(\alpha\rho_G U_G A)=\Gamma_{evap}-\Gamma_{cond} \tag{9}$$

where Γ_{evap} and Γ_{cond} represent evaporation and condensation rates, per unit mixture volume, respectively.

The mass conservation for the noncondensible gas is represented by:

$$\frac{d}{dz}(\alpha\rho_G U_G x_n)=0 \tag{10}$$

where x_n represents the mass fraction of the noncondensible in the vapor-noncondensible mixture.

The quality, x, and void fraction, α are related according to

$$\alpha=\frac{x}{x+\frac{\rho_G}{\rho_L}(1-x)\frac{U_G}{U_L}} \tag{11}$$

The vapor-noncondensible mixture density, ρ_G, can be represented as the summation of partial densities of the vapor and noncondensible, according to:

$$\rho_G=\rho_v+\rho_n \tag{12}$$

where the partial densities are related to pressure, P, according to:

$$\rho_v=\rho_g(P_v) \tag{13}$$

$$\rho_n=\frac{P-P_g}{\frac{\mathbf{R}}{M_n}T} \tag{14}$$

where P_g is the partial pressure of vapor, and $\mathbf{R}$ is the universal gas constant.

Momentum conservation for the gas phase, and the two-phase mixture, are represented by the following two equations, respectively:

$$\begin{aligned}-\alpha\frac{dP}{dz}=\alpha\rho_G g\sin(\theta)+F_{WG}+\frac{1}{A}\frac{d}{dz}[A\rho_G\alpha U_G^2]+K(U_G-U_L)+\Gamma_{cond}U_G-\Gamma_{evap}U_L\\+\rho_c C_{VM}\alpha_d\left(U_G\frac{dU_G}{dz}-U_L\frac{dU_L}{dz}\right)\end{aligned} \tag{15}$$

$$-\frac{dP}{dz}=[\alpha\rho_G+(1-\alpha)\rho_L]g\sin\theta+F_{WM}+\frac{1}{A}\frac{d}{dz}\{A[\alpha\rho_G U_G^2+(1-\alpha)\rho_L U_L^2]\} \tag{16}$$

where F_{WM} and F_{WG} are the wall friction forces, per unit length, imposed on the two-phase mixture and the gas phase, respectively, and K the interphase momentum transfer coefficient, represents the interphase drag force. The mass exchanged due to phase change, as noted, is assumed to represent the velocity of the donor phase. The last term on the right hand side of Equation (15) represents the virtual mass force.

Finally, the energy conservation equations for the two-phase mixture and the gas phase are represented by:

$$\frac{d}{dz}\{A\left[\rho_L(1-\alpha)U_L e_L+\rho_G\alpha U_G e_G\right]\}=\wp q'' \tag{17}$$

$$\frac{d}{dz}\left[A\rho_G U_G e_G\right]=A\left(\Gamma_{evap}-\Gamma_{cond}\right)e_{G,i}+A\wp'' q''_{i,G} \tag{18}$$

where the gas and liquid total specific enthalpies are defined as:

$$e_G=\hat{h}_G+\frac{1}{2}U_G^2 \tag{19}$$

$$e_L=\hat{h}_L+\frac{1}{2}U_L^2 \tag{20}$$

The gas enthalpy is given by:

$$\hat{h}_G=(1-x_n)\hat{h}_v+x_n\hat{h}_n \tag{21}$$

The parameter $e_{G,i}$ represents the specific enthaply of the mass exchanged due to evaporation or condensation, as it crosses the gas-side interphase boundary, and is obtained from:

$$e_L=\hat{h}_f+\frac{1}{2}U_L^2 \tag{25}$$

where the subscript f represents saturated liquid with respect to the local pressure.

Similarly, when the vapor in the gas phase is assumed saturated, the mixture energy conservation is represented by Equation (17), where ρ_L and e_L represent the local subcooled or superheated liquid, and

$$\rho_G=\rho_g+\rho_n \tag{26}$$

where ρ_g is the density of vapor at saturation with respect to the partial pressure of vapor in the vapor-noncondensible mixture. In equation (17), the gas total specific enthalpy, e_G, is found from Equation (19), where:

$$\hat{h}_G=\hat{h}_g+\hat{h}_n \tag{27}$$

where $\hat{h}_g$ is the vapor specific enthalpy, at saturation with respect to the local vapor partial pressure.

III.A.3.d. Dynamic slip model

This model is in fact a five-equation separated flow model, and is based on the assumption that the two phases remain saturated and hence at thermal equilibrium. Unequal phasic velocities are assumed, however.

The mixture mass conservation can be represented by Equation (8) and the noncondensible mass conservation is represented by Equation (10). The momentum conservation equations are represented by Equations (15) and (16). The mixture energy conservation is also represented by Equation (17), where liquid and vapor are now both saturated.

III.A.3.e. Thermodynamic relations

In order to simplify the analysis, in the derivation of partial derivatives of properties, the noncondensible gas and vapor are assumed to behave as ideal gases. Using the state variables P and x_n, which are provided by the solution of the conservation equations, when the gas mixture is saturated, the local gas mixture temperature and density can be found from

$$T_G=T_{sat}(P_v) \tag{28}$$

$$\rho_G=\frac{P-P_v}{\frac{\mathbf{R}}{M_n}T_G}+\rho_G^{*}$$

where $P_v = P(1 - X_n)$. The noncondensible mole fraction in the gas phase, X_n, is related to the noncondensible mass fraction according to:

$$X_n=\frac{\frac{x_n}{M_n}}{\frac{x_n}{M_n}+\frac{(1-x_n)}{M_v}} \tag{30}$$

The expansion of the left hand sides of the conservation equations, which is performed to facilitate the numerical solution as explained later, requires that the z-derivatives of some of the fluid properties be replaced with their equivalent derivatives with respect to the state variables P and x_n. This is done by applying the chain rule, and using appropriate thermodynamic approximations. From Equation (29):

$$\frac{d\rho_G}{dz}=\left(\frac{\partial\rho_G}{\partial P}\right)_{x_n}\left(\frac{dP}{dz}\right)+\left[\left(\frac{\partial\rho_G}{\partial X_n}\right)\left(\frac{\partial X_n}{\partial x_n}\right)\right]_P\frac{dx_n}{dz} \tag{31}$$

To further manipulate this equation, assume that the vapor is an ideal gas, and apply Clausius's relation:

$$\frac{\partial T_{sat}}{\partial P}=\frac{T_{sat}v_{fg}}{\hat{h}_{fg}} \tag{32}$$

It can then be shown that:

$$\left(\frac{\partial\rho_G}{\partial P}\right)_{x_n}=\frac{M_G}{\mathbf{R}T^*_{sat}}\left[1-P_v\left(\frac{v_{fg}}{\hat{h}_{fg}}\right)^*\right] \tag{33}$$

$$\left(\frac{\partial\rho_G}{\partial X_n}\right)_P=\frac{P}{\mathbf{R}T^*_{sat}}\left[(M_n-M_v)+PM_G\left(\frac{v_{fg}}{\hat{h}_{fg}}\right)^*\right] \tag{34}$$

where all parameters with the superscript *, correspond to the local vapor partial pressure $(1 - X_n)P$, and

$$M_G=M_v(1-X_n)+M_nX_n \tag{35}$$

it can be easily shown that

$$\frac{\partial X_n}{\partial x_n} = \frac{\frac{M_n}{M_v}}{[x_n + (1-x_n)\frac{M_n}{M_v}]^2} \tag{36}$$

Similarly, it can be shown that

$$\frac{d\hat{h}_G}{dz} = (\frac{\partial \hat{h}_G}{\partial P})_{x_n} \frac{dP}{dz} + (\frac{\partial \hat{h}_G}{\partial x_n})_P \frac{dx_n}{dz} \tag{37}$$

where,

$$(\frac{\partial \hat{h}_G}{\partial P})_{x_n} = (1-X_n)\,(1-x_n)\,(\frac{\partial \hat{h}_g}{\partial P})^{*} + C_{P_n}(\frac{T_{sat}v_{fg}}{\hat{h}_{fg}})^{*}(1-X_N)\,x_n \tag{38}$$

$$(\frac{\partial \hat{h}_G}{\partial x_n})_P = \hat{h}_n - x_n C_{P_n}(\frac{T_{sat}v_{fg}}{\hat{h}_{fg}})^{*} P \frac{\partial X_n}{\partial x_n} - \hat{h}_g - P(1-x_n)\,(\frac{\partial X_n}{\partial x_n})\,(\frac{\partial \hat{h}_g}{\partial P})^{*} \tag{39}$$

When the gas phase is not saturated with vapor, $\hat{h}_G$ itself is a state variable. Partial derivatives of ρ_G with respect to the three state variables P, x_n, and $\hat{h}_G$ are derived using ideal gas relations.

III.A.3.f. Conservation equations in expanded form

Parametric and design calculations can be performed in two ways. In the first method, the geometry of the drift channel cross-sectional area, and its axial variations, are assumed known, and conservation equations are solved, thereby calculating the pressure distribution along the drift channel. In the second method, the pressure distribution along the drift channel is assumed known, and the channel cross-sectional area is treated as an unknown.

The differential conservation equations presented in sections III.A.3.a through III.A.3.d were expanded using the above thermodynamic relations, and were represented as:

$$\mathbf{A}Y=C \tag{40}$$

where Y represents a column vector whose elements are the z-derivatives of the state variables. For the HEM model, when the drift channel flow area is assumed known, one has:

$$Y=\left(\frac{dP}{dz},\ \frac{dx}{dz},\ \frac{dU}{dz},\ \frac{dT_{l,J}}{dz}\right)^{T} \tag{41}$$

When the pressure is known *dP/dz* is replaced with *dA/dz*. The parameter *A* represents a 4x4 matrix, and C represents a column vector with four elements.

For the seven-equation separated flow model, when the drift channel flow area is assumed known:

$$Y=\left(\frac{dP}{dz},\ \frac{d\alpha}{dz},\ \frac{dU_G}{dz},\ \frac{dU_L}{dz},\ \frac{d\hat{h}_v}{dz},\ \frac{d\hat{h}_L}{dz},\ \frac{dT_{L,J}}{dz},\ \frac{dx_n}{dz}\right)^{T} \tag{42}$$

When pressure is assumed known, *dP/dz* is replaced in Equation (41) with *dA/dz*. The parameter *A* is then a 8x8 square matrix, and the column vector C has eight elements.

For the dynamic slip model:

$$Y=\left(\frac{dP}{dz},\ \frac{d\alpha}{dz},\ \frac{dU_G}{dz},\ \frac{dU_L}{dz},\ \frac{dT_{L,J}}{dz},\ \frac{dx_n}{dz}\right)^T \tag{43}$$

where, once again, *dP/dz* is replaced with *dA/dz* when the pressure distribution along the drift channel is assumed known.

Elements of matrix the *A* and vector C, for the case where the drift channel flow area is assumed known for homogeneous equilibrium, seven-equation separated-flow, and dynamic slip models are listed in Appendix A.3. The six-equation separated flow models are not presented for brevity.

III.A.4. Closure relations

III.A.4.a. Wall friction

Wall friction is treated using the empirical correlation of Soliman et al. [18]. Accordingly, using the Lockhart-Martinelli correlation [19], one has:

$$F_{WM}=\Phi_G^2\left(\frac{dP}{dz}\right)_{Fric,G} \tag{44}$$

where:

$$\left(\frac{dP}{dz}\right)_{Fric,G}=2\frac{f_G}{D}\frac{(Gx)^2}{\rho_G} \tag{45}$$

where G is the two-phase mixture mass flux.

The two-phase multiplier Φ_G is found from (Soliman et al. [18]):

$$\Phi_G=1+2.85X_{tt}^{0.523} \tag{46}$$

where X_{tt}, the Martinelli factor, is defined as

$$X_{tt}=\left[\frac{(\frac{dP}{dz})_{Fric,L}}{(\frac{dP}{dz})_{Fric,G}}\right]^{\frac{1}{2}} \tag{47}$$

where,

$$\left(\frac{dP}{dz}\right)_{Fric,L}=2\frac{f_L}{D}\frac{[G(1-x)]^2}{\rho_L} \tag{48}$$

$$\left(\frac{dP}{dz}\right)_{Fric,G}=2\frac{f_G}{D}\frac{[Gx]^2}{\rho_G}$$

The Fanning friction factors, f_L and f_G, are obtained by assuming only liquid and gas phases flow in the channel, respectively, and using the following correlations.

$$\begin{array}{lll} f=0.079Re^{-0.25} & for & 4000 < Re < 30,000 \\ f=0.046Re^{-0.2} & for & Re > 30,000 \end{array} \tag{50}$$

The phasic wall friction forces are represented as follows:

$$F_{WG}=\alpha F_{WM} \tag{51}$$

$$F_{WL}=(1-\alpha)F_{WM} \tag{52}$$

Equation (52) is needed only when the liquid-phase momentum equation is included in the conservation equations.

III.A.4.b. Wall heat transfer

In the drift tube the fluid is mostly a mixture of vapor dispersed droplets. The convective heat transfer coefficients are calculated using either of the following correlations, both of which apply to two-phase forced convective boiling.

The two-phase heat transfer coefficient can be obtained using Chen's correlation [19,20]. Accordingly, the heat transfer coefficient is assumed to have two components, one accounting for forced convection, the other representing nucleate boiling [19,20]:

$$h_T=h_C+h_{NB} \tag{53}$$

where h_C and h_{NB} are calculated as follows:

$$h_C=0.023\left(\frac{G(1-x)D_T}{\mu_L}\right)^{0.8}(Pr_L)^{0.4}\frac{k_L}{D_T}F \tag{54}$$

where [21]

$$\begin{aligned} F &= 1 && for \quad \frac{1}{X_{tt}}<0.1 \\ F &= 2.35\left(0.213+\frac{1}{X_{tt}}\right)^{0.736} && for \quad \frac{1}{X_{tt}}>0.1 \end{aligned} \tag{55}$$

$$\frac{1}{X_{tt}}=\left(\frac{x}{1-x}\right)^{0.9}\left(\frac{\rho_f}{\rho_g}\right)^{0.5}\left(\frac{\mu_g}{\mu_f}\right)^{0.1} \tag{56}$$

and

$$h_{NB}=S(0.00122)\left[\frac{(k^{0.79}c_p^{0.45}\rho^{0.49})_f}{\sigma^{0.5}\mu_f^{0.29}h_{fg}^{0.24}\rho_g^{0.24}}\right]\Delta T_{sat}^{0.24}\Delta P^{0.75} \tag{57}$$

where $\Delta T_{sat} = T_{wall} - T_{sat}$, $\Delta P = P_{sat}(T_{wall}) - P_{sat}(T_G)$, and [21]

$$S=\frac{1}{1+2.53\times 10^{-6}\,Re^{1.17}} \tag{58}$$

where in the above equation:

$$Re=\left(\frac{G(1-x))D_T}{\mu_f}\right)F^{1.25}$$

The correlation due to Klimenko [22,23] is represented by

$$h_T=\frac{Nu\ k_L}{L_c} \tag{60}$$

where

$$Nu=0.087Re^{0.6}Pr_L^{1/6}\left(\frac{\rho_G}{\rho_L}\right)^{0.2}\left(\frac{k_w}{k_L}\right)^{0.09} \tag{61}$$

The Reynolds number in this correlation is defined as:

$$Re=\frac{U_m L_c}{\nu_L} \tag{62}$$

where U_m is the homogeneous mixture velocity defined as

$$U_m=\frac{G}{\rho_h} \tag{63}$$

and L_c is the Laplace constant:

$$L_c=[\frac{\sigma}{g(\rho_L-\rho_G)}]^{1/2} \tag{64}$$

The above equations represent the two-phase component of Klimenko's correlation [22,23]. An additional component which accounts for pure liquid forced convection, is small for our cases of interest and has been neglected.

Single-phase liquid flows in the jacket. The convective heat transfer coefficient here is obtained from the following correlations.

$$h_{L,J}=\frac{Nu\ k_{L,J}}{D_h} \tag{65}$$

where D_h is the hydraulic diameter of the jacket. Since the flow is always turbulent (Re > 2300), we use Gnielinski's correlation [24]

$$Nu_{D_h}=\frac{(f/8)\,(Re_{D_h}-1000)\,Pr_{L,J}}{1+12.7\,(f/8)^{1/2}\,(Pr_{L,J}^{2/3}-1)} \tag{66}$$

where Re_{D_h} is the jacket Reynolds number, and

$$f=(0.79\ln(Re_{D_h})-1.64)^{-2} \tag{67}$$

The regenerative heat transfer rate, per unit channel length, between the drift tube and the jacket (see Equations (5) and (7)) is then calculated from:

$$\wp q''=\frac{2\pi\,(T_{L,J}-T_T)}{\frac{1}{R_{L,J}h_{L,J}}+\frac{\ln(R_{L,J}/R_T)}{k_{wall}}+\frac{1}{R_T h_T}} \tag{68}$$

where T_{LJ} and T_T are the local jacket and drift tube mean fluid temperatures, respectively, k_{wall} is the thermal conductivity of the drift tube, and R_T and R_{LJ} are the inner and outer radii of the drift tube, respectively. Equation (68) assumes a circular drift tube cross section. For other geometries, however, it can be easily modified.

III.A.4.c. Two-phase flow regimes

The flow regime over most of the drift tube is annular-dispersed droplet, except near the bottom (near point 4 in Figure 8), where massive condensation occurs.

Bubbly, dispersed bubbly, churn, and annular-dispersed regimes are considered. The flow regime is assumed to be bubbly churn when $\alpha < 0.3$ [25,26], and as long as [26]:

$$j_L+j_G < 4\left\{\frac{D_T^{0.249}(\sigma/\rho_L)^{0.089}}{\nu_L^{0.072}}\left[\frac{g\Delta\rho}{\rho_L}\right]^{0.446}\right\} \tag{69}$$

where $\Delta\rho = \rho_L - \rho_G$, and the liquid and gas superficial velocities are defined as

$$j_L=\frac{G(1-x)}{\rho_L A} \tag{70}$$

$$j_G=\frac{Gx}{\rho_G A} \tag{71}$$

Rayleigh-Taylor instability and aerodynamic forces limit the bubble size in this regime. The maximum stable bubble size allowed by Rayleigh-Taylor instability is [27]:

$$d_B=4L_c \tag{72}$$

where L_c is the Laplace constant (Equation (64)). The maximum bubble diameter allowed by the aerodynamic dispersion mechanism can be represented by a critical Weber number:

$$We_{Cr}=\frac{\rho_L(U_G-U_L)^2 d_B}{\sigma} \tag{73}$$

Bubble diameter in the bubbly regime is chosen to be the smaller value obtained from Equations (72) and (73), where, in Equation (73), $We_{Cr} = 3$ is assumed.

When Equation (69) is violated, and as long as $\alpha < 0.52$ [28], dispersed-bubbly regime prevails where turbulent break-up mechanism maintains small spherical bubbles. The bubble diameter in this regime is obtained from [26,29]:

$$d_B = \left[\frac{0.4\sigma}{g\Delta\rho} \right]^{1/2} \tag{74}$$

Bubbly regime leads to churn flow when $\alpha = 0.3$. Dispersed bubbly also leads to churn flow when $\alpha = 0.52$. Churn flow regime is assumed to persist as long as $\alpha < 0.7$ [25]. Bubble diameter in churn regime is calculated using Equation (72).

The specific interfacial surface area, namely, the interfacial surface area per unit two-phase mixture volume, is calculated in bubbly, dispersed bubbly, and churn regimes from:

$$\rho'' = \frac{6\alpha}{d_B} \tag{75}$$

The annular-dispersed droplet regime is treated by using a user-specified interpolation parameter, which determines which regime, annular or dispersed-droplet, is predominant. This approach is adopted to provide flexibility in simulating the experimental data. Thus , when $\alpha > 0.7$, we assume:

$$\rho'' = \xi \rho''_{disp} + (1-\xi)\, \rho''_{ann} \tag{76}$$

where $0 \leq \xi \leq 1$ is the user-specified interpolation parameter, and

$$\rho''_{disp}=\frac{6\,(1-\alpha)}{d_D} \tag{77}$$

$$\rho''_{ann}=\frac{4\,(D_T-2\delta)}{D_T^2} \tag{78}$$

where d_D is the diameter of the droplets in a purely dispersed droplet regime, and δ is the film thickness in a purely annular flow regime.

The dispersed droplet diameter is calculated from:

$$d_D=\min\{L_c,\ \frac{\sigma We_{cr}}{\rho_G(U_G-U_L)^2}\} \tag{79}$$

where We_{Cr} = 12 [25].

The liquid film thickness corresponding to a purely annular flow regime is found from:

$$\delta=\frac{D_T}{2}(1-\sqrt{\alpha}) \tag{80}$$

Equations (80) and (80) assumes circular drift tube cross-section, and can be easily modified to represent other geometries.

III.A.4.d. Liquid-gas interphase forces

In bubbly, dispersed bubbly, and churn regimes, where liquid is the continuous phase, the interphase momentum transfer coefficient, K, is obtained from:

$$K=\frac{3}{4}\alpha\rho_L C_D\frac{|U_G-U_L|}{d_B} \tag{81}$$

where C_D is the drag coefficient for bubbles, which will be discussed later in this section.

In annular-dispersed droplet, in accordance with the discussion in the previous section, we interpolate between a purely annular and a purely dispersed-droplet regime, using the user-specified interpolation parameter $0 \leq \xi \leq 1$, as follows:

$$K=\xi K_{disp}+(1-\xi)K_{ann} \tag{82}$$

where

$$K_{disp}=\frac{3}{4}(1-\alpha)\rho_G C_D\frac{|U_G-U_L|}{d_D} \tag{83}$$

$$K_{ann}=\rho''_{ann}c_{fi,ann}\frac{1}{2}\rho_G|U_G-U_L| \tag{84}$$

where ρ''_{ann} is found from (78) and from [30]:

$$c_{fi,ann}=0.005[1+75(1-\alpha)] \tag{85}$$

The droplet and bubble drag coefficient, C_D, is calculated using the empirical correlations of Ishii and Zuber [25]. First consider bubbly and dispersed bubbly regimes. The viscous flow regime and its associated drag coefficient are represented by:

$$d_B\left[\frac{\rho_L g\Delta\rho}{\mu_L^2}\right]^{1/3}\leq 69.3 \tag{86}$$

$$C_D=\frac{24}{Re_B}(1+0.1Re_B^{0.75}) \tag{87}$$

where

$$Re_B=\rho_L d_B\frac{|U_G-U_L|}{\mu_M} \tag{88}$$

The mixture viscosity, μ_M, is found from

$$\mu_M=\frac{\mu_L}{(1-\alpha)} \tag{89}$$

when Equation (86) is violated, then [25]:

$$C_D=\frac{2}{3}d_B\left[\frac{g\Delta\rho}{\sigma}\right]^{1/2}\left\{\frac{1+17.67[f(\alpha)]^{6/7}}{18.67[f(\alpha)]}\right\}^2 \tag{90}$$

where $f(\alpha) = (1 - \alpha)^{3/2}$.

For churn flow regime, one can write [25]:

$$C_D=\frac{8}{3}(1-\alpha)^2 \tag{91}$$

For dispersed droplets, Equations (86) through (89) are modified as follows [25]. In viscous flow regime:

$$d_D\left[\frac{\rho_G g \Delta\rho}{\mu_G^2}\right]^{1/3} \leq 69.3 \tag{92}$$

$$C_D=\frac{24}{Re_D}\left(1+0.1Re_D^{0.75}\right) \tag{93}$$

where

$$Re_D=\rho_G d_D\frac{|U_G-U_L|}{\mu_M} \tag{94}$$

$$\mu_M=\frac{\mu_G}{\alpha^{2.5}} \tag{95}$$

When equation (92) is violated in the dispersed-droplet regime, then Equation (90) is used, where, d_B is replaced with d_D, and $f(\alpha) = \alpha^3$.

The virtual mass coefficient, C_{VM}, is found from the following correlation [31], which is assumed to apply to bubbly and churn regimes:

$$C_{vm}=0.5+1.39\alpha \tag{96}$$

In annular-dispersed regimes $C_{vm} = 0$ is assumed since $\rho_G \ll \rho_L$.

III.A.4.e. Heat and mass transfer at the liquid-gas interphase

Phase Change Mass Transfer

In calculating evaporation or condensation mass fluxes, distinction is made between essentially pure vapor and vapor-noncondensible mixture.

When $x_n \leq 0.0025$ or $T_L > T_{sat}(P_v)$ pure vapor is assumed. The phase-change mass flow rate, per unit two-phase mixture volume, is then calculated from [32]:

$$\Gamma = -\rho''\dot{m}'' \qquad (97)$$

where $\dot{m}''$ represents the condensation mass flux at the interphase and is governed by

$$\dot{m}'' = \frac{q''_{i,G} + q''_{i,L}}{\hat{h}_{fg}} \qquad (98)$$

where

$$q''_{i,G} = \dot{h}_G (T_{sat} - T_G) \qquad (99)$$

$$q''_{i,L} = \dot{h}_L (T_{sat} - T_L) \qquad (100)$$

When $\Gamma > 0$, then $\Gamma_{evap} = \Gamma$ and $\Gamma_{cond} = 0$, otherwise $\Gamma_{evap} = 0$ and $\Gamma_{cond} = -\Gamma$. Parameters $\dot{h}_G$ and $\dot{h}_L$ represent heat transfer coefficients in the presence of high mass transfer, and are found from

$$\dot{h}_G=\frac{-\dot{m}''c_{P,G}}{\exp\left(\frac{-\dot{m}''c_{P,G}}{h_G}\right)-1} \tag{101}$$

$$\dot{h}_L=\frac{\dot{m}''c_{P,L}}{\exp\left(\frac{\dot{m}''c_{P,L}}{h_L}\right)-1} \tag{102}$$

Liquid and gas side heat transfer coefficients, h_L and h_G both depend on the flow regime, as will be explained later.

In annular-dispersed regime the phase-change mass flux is obtained by interpolating between the pure annular and pure droplet dispersed regimes, using the aforementioned user-specified interpolation parameter ξ, according to:

$$\Gamma=\xi\Gamma_{disp}+(1-\xi)\Gamma_{ann} \tag{103}$$

When $x_n \geq 0.0025$ and $T_L < T_{sat}(P_v)$, condensation in the presence of noncondensibles is modelled as follows. Energy balance at the interphase requires that [32]:

$$\dot{m}''h_{fg}+\dot{h}_L(T_L-T_i)+\dot{h}_G(T_G-T_i)=0 \tag{104}$$

where T_i is the interphase temperature. Diffusion of vapor in the gas phase requires that

$$\dot{m}''=-K_G\ln\left(\frac{x_n}{1-x_{v,i}}\right) \tag{105}$$

where K_G is the gas-side mass transfer coefficient. The vapor mass fraction at the interphase, $x_{v,i}$, is related to the interphase temperature according to:

$$x_{v,i}=\frac{X_{v,i}M_v}{X_{v,i}M_v+(1-X_{v,i})M_n} \tag{106}$$

$$X_{v,i}=\frac{P_{sat}(T_i)}{P} \tag{107}$$

Thus, when condensation in the presence of noncondensibles occurs, Equations (101), (102), and (104) through (107) are simultaneously solved for T_i, $\dot{m}''$, $\bar{h}_G$, $\bar{h}_L$, $x_{v,i}$, and $X_{v,i}$.

Heat and Mass Transfer Coefficients

The correlations to be described below are well-accepted steady-state correlations, and are provided as the default option.

First consider the gas-side transfer correlations. Using the analogy between convective heat and mass transfer processes, heat and mass transfer coefficients can be obtained using similar correlations as follows.

In bubbly and churn regimes, the correlation of Kronig and Brink [33] is used for calculating the gas-side heat and mass transfer coefficients:

$$Nu_G=\frac{h_G d_B}{k_G}=17.9 \tag{108}$$

$$Sh_G=\frac{K_G d_B}{\rho_G D}=17.9 \tag{109}$$

where *D* is the molecular diffusion coefficient for the vapor-noncondensible pair.

In the pure dispersed regime, the well-known Ranz-Marshall correlation is used [34]:

$$Nu_G=\frac{h_G d_D}{k_G}=2.0+0.6Re_D^{1/2}Pr_G^{1/3} \tag{110}$$

$$Sh_G=\frac{K_G d_D}{\rho_G D}=2.0+0.6Re_D^{1/2}Sc_G^{1/3} \tag{111}$$

where the gas side Schmidt number is defined as:

$$Sc=\frac{\nu_G}{D} \tag{112}$$

Finally, in the pure annular regime, we use the Dittus-Bolter correlation [22], and write:

$$Nu_G=\frac{h_G D_T\sqrt{\alpha}}{k_G}=0.023Re_G^{0.8}Pr_G^{0.33} \tag{113}$$

$$Sh_G=\frac{K_G D_T\sqrt{\alpha}}{\rho_G D}=0.023Re_G^{0.8}Sc_G^{0.33} \tag{114}$$

where

$$Re_G=\frac{\rho_G U_G D_T\sqrt{\alpha}}{\mu_G} \tag{115}$$

The default liquid-side heat transfer correlations are now presented.

In bubbly and churn regimes, we use the surface renewal model [35], and write:

$$h_L=2\left[\frac{k_L\rho_L c_{P,L}}{\pi t^*}\right]^{1/2} \tag{116}$$

where t* represents the bubble surface renewal period, and is estimated from

$$t^*=\frac{d_B}{0.1|U_G-U_L|} \tag{117}$$

In the above equations t* has been represented by the bubble recirculation period, and the liquid velocity at the bubble surface has been assumed to be 0.1 times the slip velocity. For purely dispersed droplet regime, the liquid-side heat transfer coefficient is calculated based on the average heat flux at the surface of a droplet which is initially at a uniform temperature equal to T_L, and is exposed to an environment at T_i for a period of t*. Utilizing the mathematical solutions of transient heat conduction in a sphere with constant surface temperature [36], one can write

$$h_L=\frac{\rho_L c_{P,L} d_D}{6t^*}\{1-6\sum_{n=1}^{\infty}\frac{1}{\beta_n^2}\exp(-\frac{4\alpha_T\beta_n^2 t^*}{d_D^2})\} \tag{118}$$

$$\beta_n=n\pi$$

The characteristic surface renewal time period, t*, is assumed to be determined by the droplet internal circulation period, or the droplet oscillation period, which ever is shorter. For droplets for which the Reynolds number is of the order of 100 the recirculation velocity at the droplet surface is approximately $0.1(|U_G - U_L|)$ [37], resulting in

$$t^{*} \approx \frac{d_D}{0.1(|U_G-U_L|)}$$

For oscillating droplets $t^{*} \approx 1/f$, where f is the oscillation frequency. When $\rho_L \gg \rho_G$, the dominant natural oscillation frequency is [38]

$$f=\left[\frac{2\sigma}{\pi^2 d_D^3 \rho_L}\right]^{1/2}$$

Therefore:

$$t^{*}=\min\left\{\frac{d_D}{0.1(|U_G-U_L|)}, \frac{\pi d_D^{3/2}\rho_L^{1/2}}{\sqrt{2\sigma}}\right\} \tag{121}$$

The effective thermal diffusivity of the liquid is found from:

$$\alpha_T=2.75\frac{k_L}{\rho_L c_{P,L}} \tag{122}$$

where the coefficient 2.75 accounts for the effect of the droplet internal circulation [33].

Finally for pure annular regime we use the following correlation which applies to heat transfer in falling films [32].

$$h_L=0.04\frac{k_L}{\nu_L^2/g}Re_\delta^{0.2}Pr_L^{0.47} \tag{123}$$

where

$$Re_{\delta}=\frac{U_L\delta}{\mu_L} \tag{124}$$

where δ is the film thickness given in Equation (80).

III.A.4.f. Properties

Thermodynamic properties of water and steam used in this model are calculated using the National Bureau of Standards steam formulation [39]. This formulation is based on an analytic equation for each property, that is an approximation to the relevant Helmholtz function. The equation has the form

$$A = A(\rho,T) = A_{base}(\rho,T)+A_{residual}(\rho,T)+A_{ideal}(\rho,T) \tag{125}$$

where A represents the specific Helmholtz function.

The first part of Equation (125) describes the high temperature behavior at all densities, and dense fluid behavior at all temperatures. The second part of the equation provides corrections to the base. The third part of Equation (125) describes the ideal gas behavior of the fluid. Since this function is analytic, all other thermodynamic properties are easily derived using the first and second laws of thermodynamics.

Although this formulation is computationally expensive, it provides highly accurate results and a smooth continuous function near the saturation dome.

Other thermophysical properties can be derived using thermodynamic properties and Maxwell relations. For example, the specific heat at constant volume c_v and the specific heat at constant pressure c_p can be calculated as follows:

$$c_v = -T\frac{\partial^2 A}{\partial T^2}$$

$$c_p = c_v + \frac{T}{\rho^2}\frac{(\partial P/\partial T)^2}{\partial P/\partial \rho} \tag{127}$$

Transport properties for water and steam used in this model are calculated from polynomials based on the thermodynamic properties of water and steam and are approved by IAPS [39].

Properties for the noncondensible air are calculated from a package provided with the text *Fundamentals of Classical Thermodynamics* by G.J. Van Wylen and R.E. Sonntag [1].

III.A.5. Method of solution

III.A.5.a. Integration method

As previously discussed in Section III.A.3.f the conservation equations are expanded into a system of ordinary differential equations (ODE). This system is integrated with a software package that uses backward differentiation formulas (bdf-s) based on Gear's method [40].

Gear's method calculates solutions to an initial value problem for a system of ordinary differential equations (ODE) of the form

$$\frac{dy_i(z)}{dz} = f_i(\ y_1(z),\ \dots\ ,y_N(z),z) \tag{128}$$

where y and f are vectors and subject to the initial condition

$$y(z_0)=y_0 \tag{129}$$

One of the major advantages of Gear's method is it's ability to solve stiff ODE problems. An ODE system is considered stiff if the system includes terms that are changing very rapidly, together with terms that are changing very slowly. One property of stiff systems is that some of the "time constants" (functions of the eigenvalues of the Jacobian matrix for the system) are very small. These small time constants force the explicit integration step size to be small also. Thus, the problem cannot be solved in a reasonable amount of time. However, Gear's method is able to overcome this problem using implicit methods and powerful iteration techniques.

III.A.5.b. The JTMM computer code

The Johnson Tube Multi-Model (JTMM) computer code was developed based on the analytical model presented in Sections III.A.2 through III.A.4. Main features of this code are briefly described in this section. Appendix A.1 provides a listing of the code while the JTMM user's manual is given in Appendix A.2.

Calculations start by assuming known fixed conditions upstream of the nozzle (Station 1 in Figure 8). The critical flow rate through the nozzle is then calculated. The main body of the JTMM code contains four nested loops to control the flow of the program. The first loop, which is the outer-most loop, controls the iteration procedure for a Johnson Tube^{TM} Heat Pump (JTHP) cycle calculation. The second loop controls the section geometry specified by the user. The typical JTHP geometry includes the following 5 sections (see Figure 8): the nozzle (from z = 0, i.e. the nozzle throat, to Station 2), the load (from Station 2 to Station 3), the regenerator (from Station 3 to 4 for the two-phase side and Station 7 to Station 6 in the annulus), and the two-phase and one-phase diffusers (from Station 4 to Station 5). The third loop controls the integration within each section over the specified length of the section. The fourth and inner-most loop controls the file output of calculated results within each section. A flow chart for the main body of the JTMM code is provided in Figure 9.

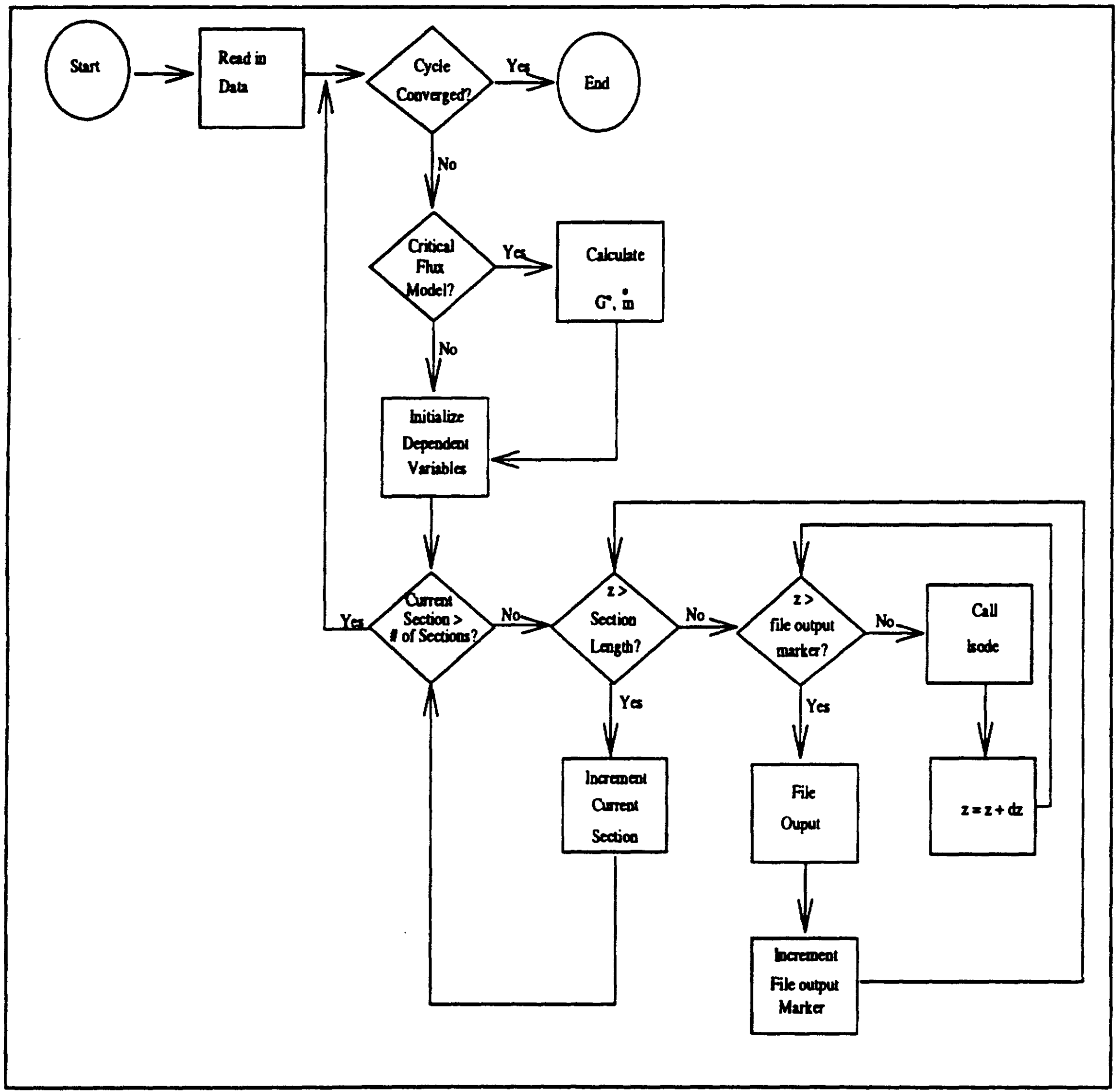

Figure 9: *JTMM Main Section Flow Chart*

JTMM interfaces with the bdf-s code through the driver subroutine LSODE, which makes frequent calls to set of user subroutines. LSODE [40] is a routine in the bdf-s package which performs the numerical integration of the ordinary differential equation system. To integrate the system, LSODE calls the subroutine FEX to calculate the vector Y (see Equation (40)). Subroutine FEX evaluates the parameters associated with the matrix *A* and the vector C, then using an LU decomposition with maximal column pivoting solves for the vector Y. A flow chart for subroutine FEX is shown in Figure 10.

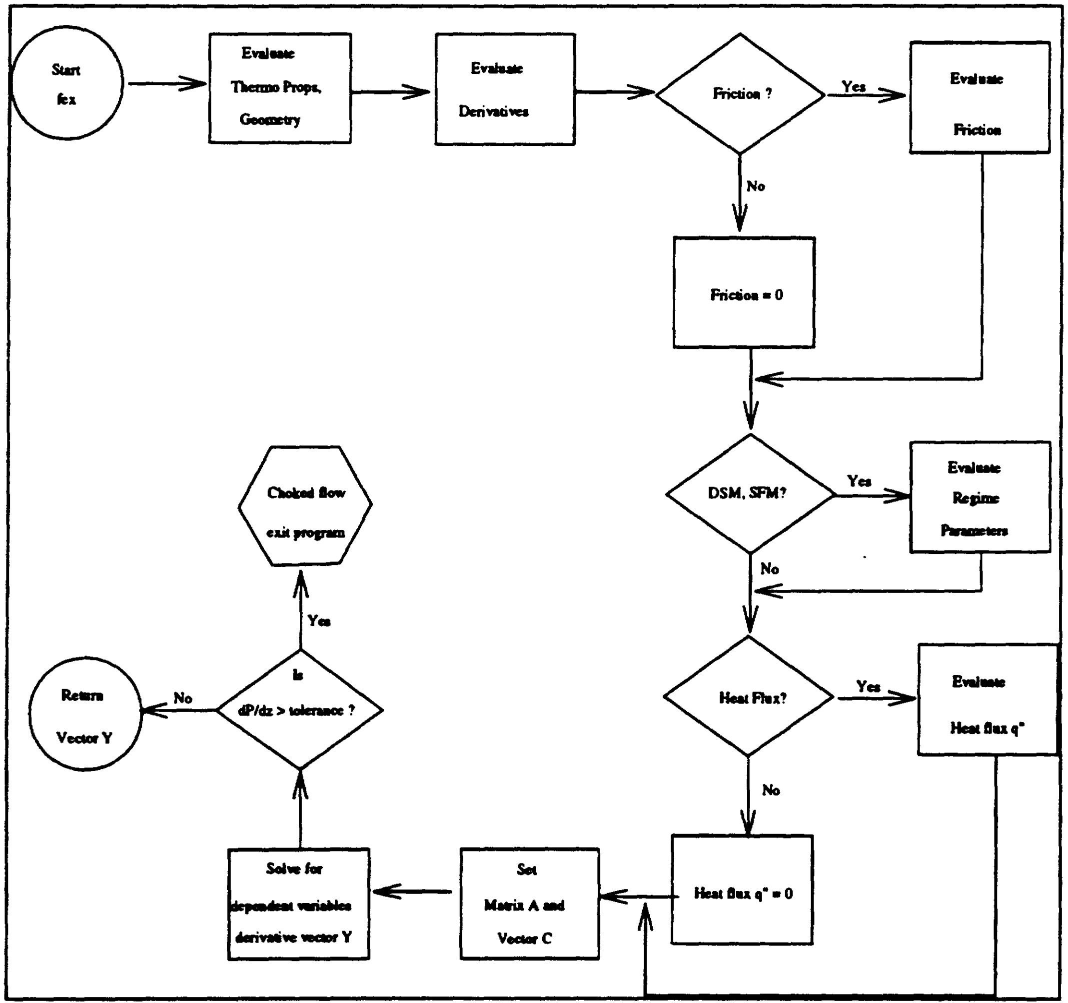

Figure 10: *Subroutine **FEX** Flow Chart*

To iterate on a Johnson Tube™ Heat Pump Cycle, the user specifies the stagnation pressure and temperature at Station 1 in Figure 8. The code will then apply the user selected critical flow model to calculate the mass flow rate if a nozzle throat flow area is specified, or the throat diameter for a user specified mass flow rate. Once the critical flow calculation is finished, the integration of the ODE system begins from the nozzle throat (z = 0, in Figure 8). As stated before, the subroutine LSODE controls the integration from the throat through the nozzle and the load section (from z= 0 to Station 3). The temperature at Station 7 (the exit temperature for the annular jacket) is guessed (starting from a user-specified initial guess) and the integration continues from station 3 to Station 5 for the two-phase side and from Station 7 to Station 6 in the annulus. The integrated result for the temperature at Station 6, $T_{6,i}$ is used to check for convergence of the cycle as explained below. The pressure at Station 5 is then used to estimate the pump work, W. Then, from an energy balance for the entire cycle, the heat rejection rate $\dot{Q}_{out}$, is calculated from

$$\dot{Q}_{out}=\dot{Q}_{in}+\dot{W} \tag{130}$$

Knowing $\dot{Q}_{out}$, the fluid state at Station 6 can be calculated using energy conservation and assuming no pressure loss in the heat exchanger. The calculated temperature for Station 6, $T_{6,c}$ can then be compared to the integrated value, $T_{6,i}$ for convergence using

$$|T_{6,i}-T_{6,c}|\le\epsilon \tag{131}$$

where ε is a convergence tolerance specified by the user in the input card. If Equation (131) is satisfied then the cycle calculations have converged and the program stops, otherwise a new value for the temperature at Station 7 is calculated based on linear interpolation. This iterative scheme is shown graphically in Figure 11.

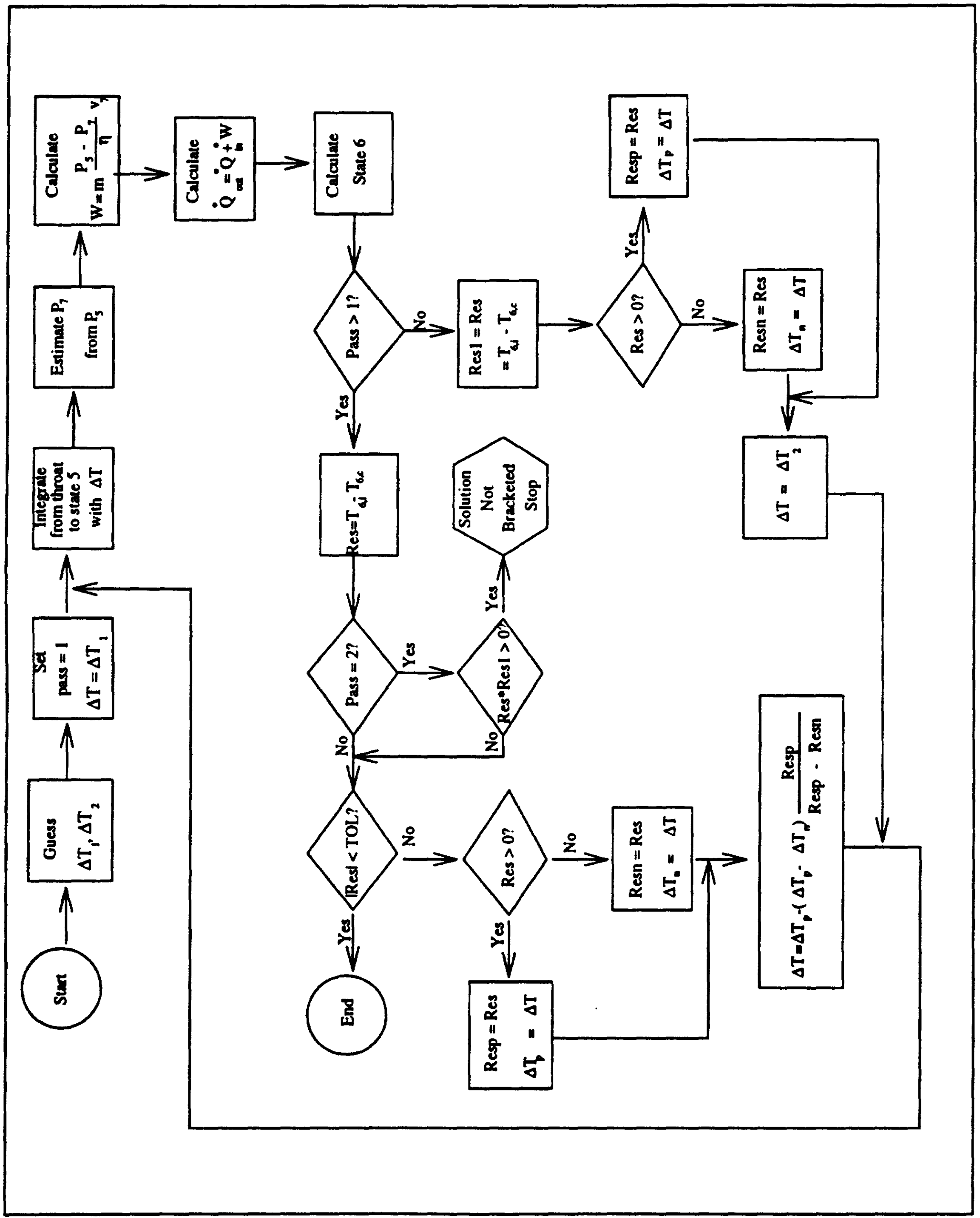

Figure 11: *JTMM Iterative Scheme Flow Chart*

III.B. Thermodynamic Model

III.B.1. Solution strategy

The thermodynamic model comprises a single closed flow loop as illustrated in Figure 12. Table 1 outlines the included components.

Table 1: *Thermodynamic Model Components*

Inlet State	Outlet State	Component Description
7	1	Liquid pump with efficiency η_p
1	2	Adiabatic two-phase nozzle with efficiency η_n
2	3	Deceleration and compression (diffusion) with low temperature heat input
3	4	Deceleration and compression with recuperative heat exchange
4	5	Adiabatic deceleration and compression
5	6	Heat rejection at higher temperature
6	7	Recuperative heat transfer from liquid

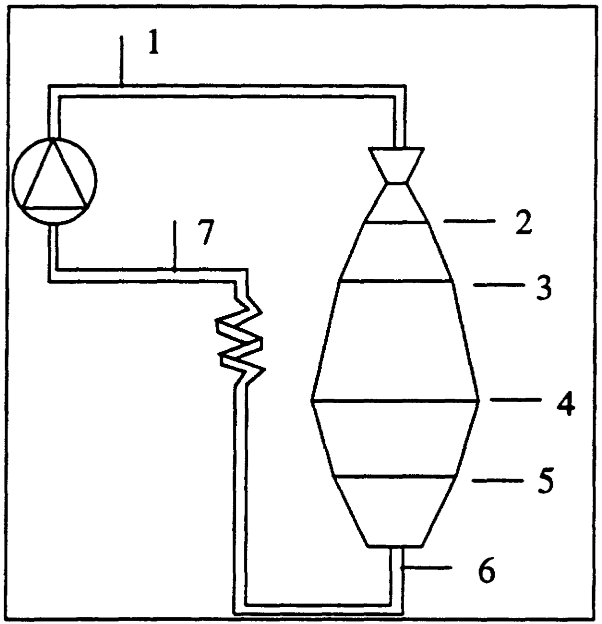

Figure 12: *Schematic Diagram for the Johnson Tube™ Heat Pump*

III.B.2. Methodology for thermodynamic model

In this model, one dimensional quasi-static flow was assumed. Component parameters based on data from existing literature were used to model the non-ideal effects in the various components. The algorithm for the thermodynamic computer model is as follows:

1. State 7 is guessed. This is a low pressure, low velocity state.

2. The pressure, P_1, provided by the pump is specified.

3. The pump work, w_p, can then be calculated from

   $w_p = v(P_1 - P_7)/\eta_p$

   where v = specific volume
   η_p = pump efficiency

4. State 1 can be established from

   $h_1 = h_7 + w_p$

5. Nozzle calculations were performed for an adiabatic nozzle. The adiabatic nozzle has a well established model relying on a nozzle efficiency, η_n, such that:

   $V_2^2 = \eta_n V_{2s}^2$, where V_{2s} is the velocity after isentropic expansion, and

   $h_2 = h_1 - V_2^2/2$

   An energy balance gives the velocity at the nozzle exit. This establishes State 2.

6. Unlike the pump and nozzle, no well-established elementary model exists for the two-phase decelerating and compressing flow with heat transfer that prevails from Station 2 to Station 3 and elsewhere in the drift tube diffuser. In the absence of a simple model, we have used a multiple stage component model that combines, in each stage, two distinct substages: an incremental heat transfer process which is modeled with the usual LMTD formulation followed by an incremental adiabatic pressure increase modeled by the traditional pressure recovery coefficient. This concept is illustrated in Figure 13 which is a Mollier chart (h-s diagram) for one stage of the diffuser.

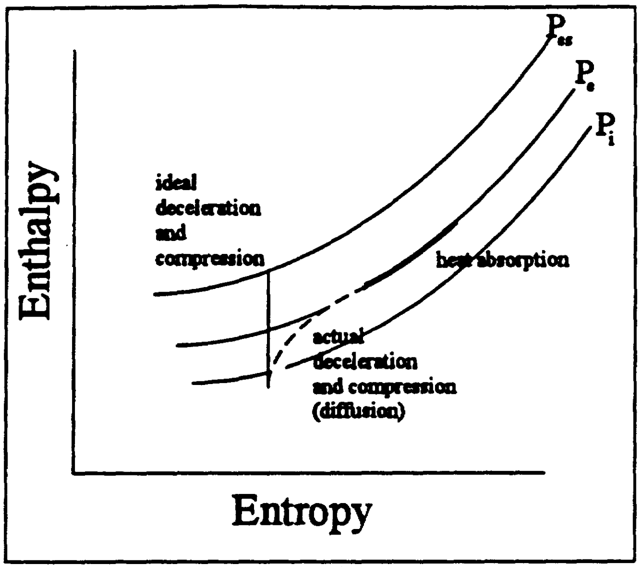

Figure 13: *Mollier Diagram for Diffusion with Heat Transfer*

For the heat transfer substage, the heat transfer was modeled with the usual formulation:

$q = U_jA_j\, F_g$ LMTD, and $h_e = h_i + q$

where: U_jA_j is the overall conductance for stage j
F_g is the usual geometric correction factor if needed (e.g. for cross flow)
LMTD is the usual Log Mean Temperature Difference

This fractional heat input is assumed a constant pressure process with no velocity loss. We now have the pressure and enthalpy at this substage and so the state at this substage is known. Now, diffusion occurs with isentropic pressure increase to get a new pressure, with the same entropy. For a specified velocity decrease, the ideal isentropic pressure rise would be from the inlet pressure P_i to the ideal exit pressure:

P_{es} at $s_e = s_i$ and $h_e = h_i - (V_e^2 - V_i^2)/2$

The actual pressure rise is then computed with the usual pressure recovery coefficient, K_p, such that:

$P_e - P_i = K_p\,(P_{es} - P_i)$

This calculation gives the new pressure after the diffusion substage assuming the enthalpy is the same. It was possible to accurately model the entire process of deceleration and compression with heat transfer in the low temperature heat input section as long as a sufficient number of steps were taken.

7. The decelerating and compressing flow from Station 3 to Station 4 in the drift tube diffuser involves recuperating heat transfer from the higher pressure liquid. The model for this process is analogous to the model for the heat input section, but the situation is more complicated as the heat source temperature cannot be taken as fixed. The heat source temperature depends itself on the upstream heat exchange with the two phase process. Hence, the regenerator is represented by an iterative loop within the main program. (The iterative loop encompasses Steps 7 through 9). The basic process is the technique is described in Step 6 above with the following modifications. The temperature difference across the regenerator is guessed. Using this temperature difference and calculating by substages down the regenerator, State 4 can be calculated as well as the temperature T_6 of the liquid entering the outside of the regenerator.

8. From Station 4 to Station 5 is an adiabatic diffuser. The exit velocity is small, so the enthalpy can be obtained from the energy equation. For the ideal case, the entropy remains the same as for Station 4. The non-ideal pressure can be modeled using a single pressure recovery coefficient. State 5 is then determined.

9. Next, heat is removed between Stations 5 and 6. The heat removal process can be modeled with the usual LMTD formulation. The heat removal was determined from:

   $$q_H = \varepsilon\, C_{p,ref}\, \Delta T$$

   where
   ε = heat transfer effectiveness
   $C_{p,ref}$ = specific heat of refrigerant
   ΔT = temperature difference between inlet and outlet of refrigerant

   $$h_6 = h_5 - q_H$$

   Now, the temperature at Station 6 can be compared to that calculated above in Step 7. The temperature difference should be updated to agree with this value, and Steps 7 through 9 iterated on. After a few iterations, consistently steady profiles for both the inner and outer fluids are invariably obtained.

10. The properties at Station 7 can be calculated from:

    $$h_6 - Q_{regen} = h_7$$

    No pressure loss is assumed to occur from Station 6 to 7. Check to be sure that the properties at Station 7 are the same as those originally used in Step 1.

The thermodynamic system model is sufficiently detailed and flexible to allow the parametric design studies necessary for developing the prototype and for further preliminary design studies such as component sizing and selection. The evaluation of alternative working fluids is possible since the thermodynamics property package includes detailed data for several widely used working fluids and provisions for estimating the properties of less familiar fluids.

IV. EXPERIMENTAL WORK

Three types of experiments were conducted during the course of this investigation. The first type, hereafter referred to as nozzle performance experiments, were aimed at quantifying the nozzle performance within the range of variables (inlet temperature, pressure, and velocity) expected in the proof-of-concept experimental facility. The second type of experiments were aimed at measuring the two-phase velocities at the nozzle exit using laser Doppler velocimetry. In the third type of experiments, a proof-of-concept test facility for the entire Johnson Tube™ was constructed and tested. The three types of experiments are described in Sections IV.A, IV.B, and IV.C, respectively.

IV.A. Nozzle Performance Experiments

IV.A.1. Purpose of experiments

The nozzle is a critical component of the Johnson Tube™ heat pump. However, the two-phase computer models may not accurately predict the flow in the nozzle chosen for the experiments. The small throat diameter of the test nozzle (0.030 inches), together with the high level of subcooling at the nozzle inlet, is not encompassed by the semi-empirical models available in the literature [4,5,6,7]. The test nozzle contains an inlet swirl to enhance atomization, which also affects the flow in the nozzle. Therefore, the nozzle behavior must be characterized experimentally and the computer model modified accordingly.

IV.A.2. Experimental design and construction

Figure 14 and Figure 15 illustrate the nozzle performance test apparatus. The nozzle test apparatus consists of a clear plastic molded nozzle with a swirl insert, which is attached to a straight plastic drift tube mounted onto a water reservoir. Water flow and pressure is provided by a brass Teel Rotary Vane Pump Model 3P752 with a 1/2 horsepower motor. The pump was sealed to prevent air leakage under vacuum. The pump exit pressure can be controlled by adjusting the amount of fluid bypassing the pump. The flow rate is measured using an Omega 150 mm rotameter with a steel float. A Vulcan 1000 Watt bushing immersion heater provides the heat input required to adjust the nozzle inlet temperature. The experimental apparatus was designed to be flexible by allowing the nozzle, and drift tube to be changed. In addition, the inlet temperature and pressure can be easily varied. The data acquisition system is presented in Appendix B (a copy of the data acquisition software is also given). Initially, a straight drift tube configuration was chosen for the nozzle experiments. Figure 15 illustrates the detailed configuration for measuring the pressures in the drift tube section.

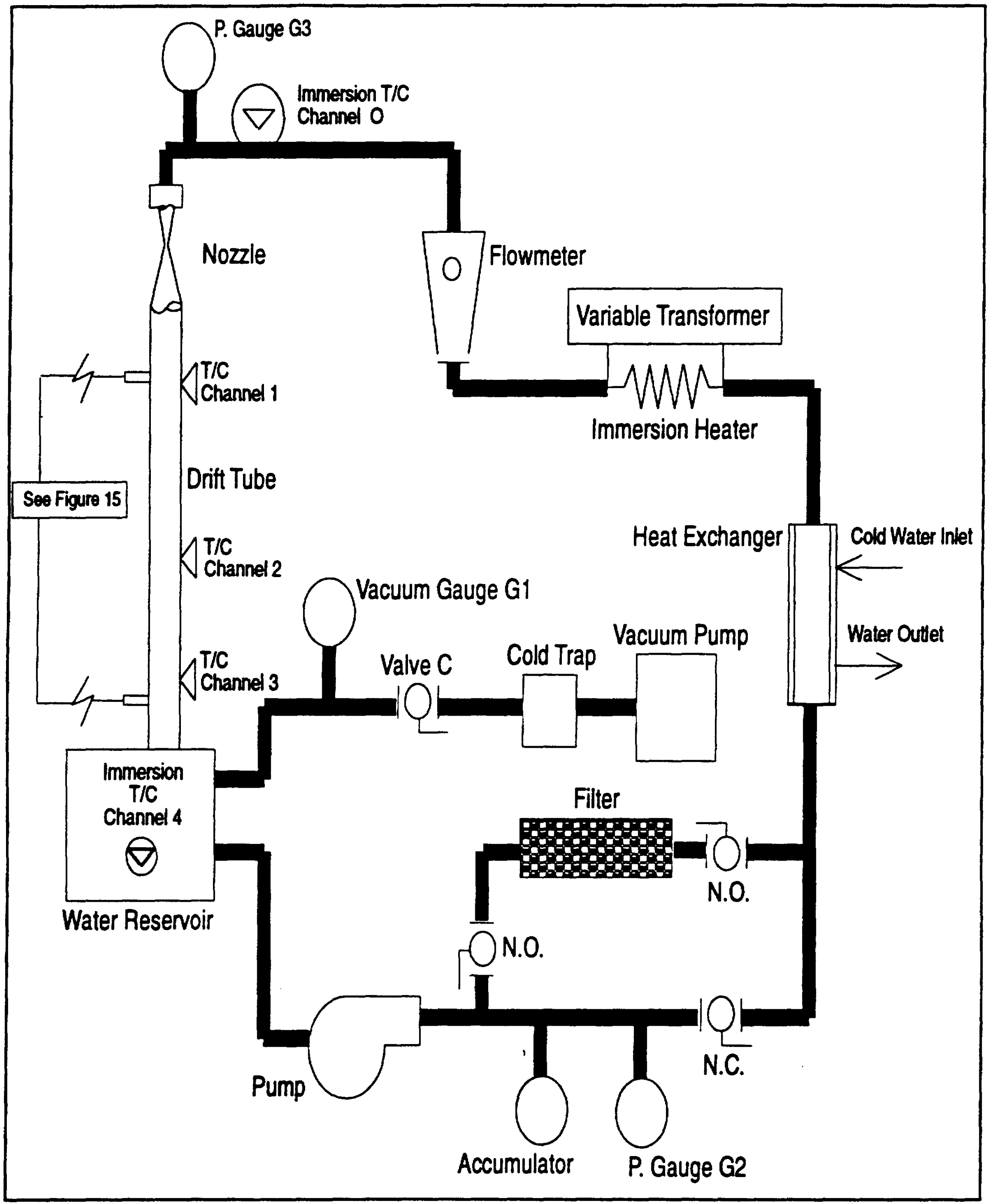

Figure 14: *Nozzle Experiment Test Apparatus*

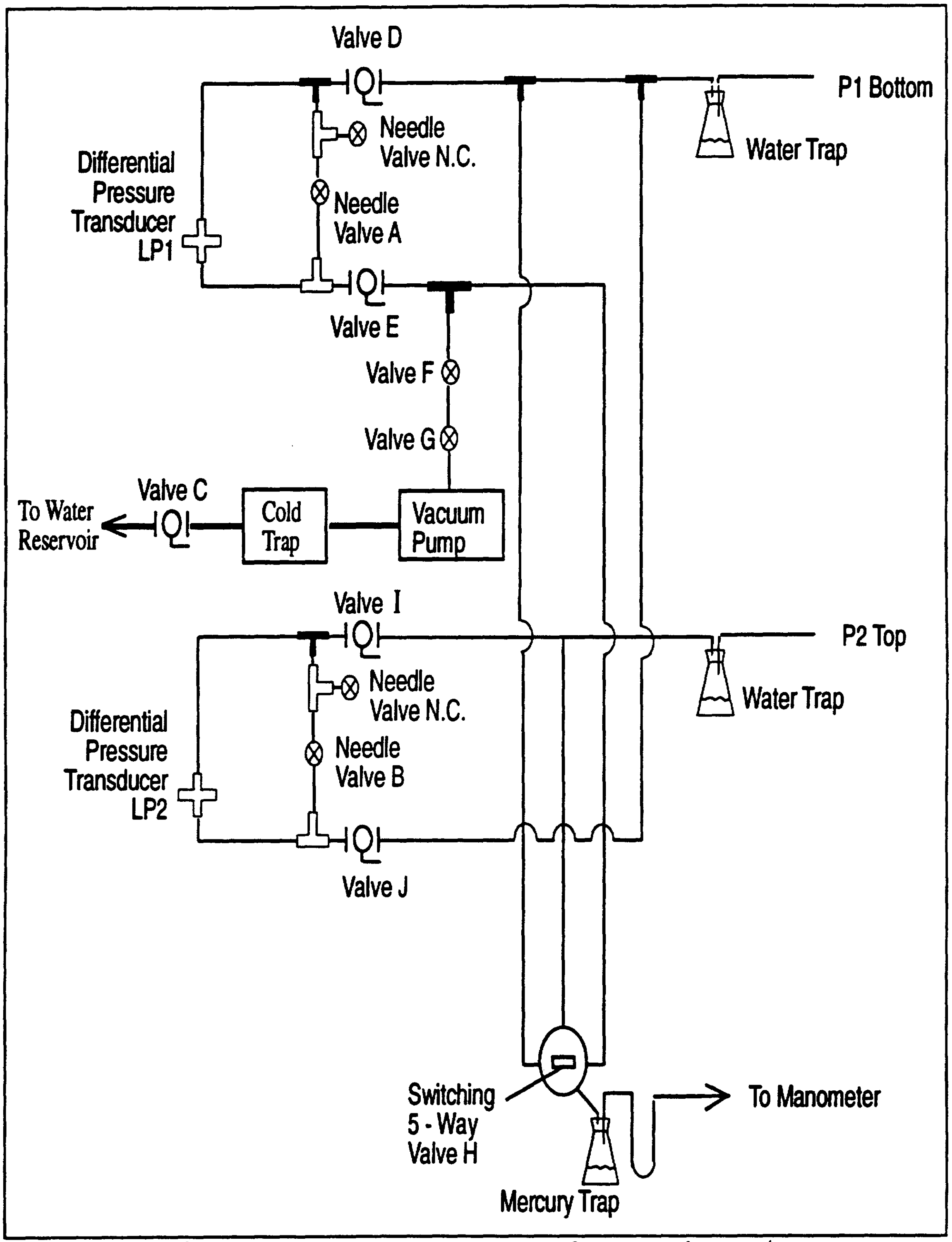

Figure 15: *Pressure Transducer Schematic*

IV.A.3. Experimental test conditions

A matrix of the nozzle performance tests conducted is shown in Table 2. A conical nozzle with straight sides and a 10 degree total included angle was used for these tests. In addition to these experiments, nozzles with insert swirl angles of 5°, 15°, and 20° were tested. All tests were repeated with atmospheric pressure at the nozzle outlet. A total of 72 steady state experiments were performed. These tests fully characterized the behavior of the 10 degree nozzle and will allow the computer codes to be validated within this range of variables.

Table 2: *Nozzle Parametric Experiments*

TEST	P Inlet	T Inlet	Swirl Angle	Vapor Pressure of Nozzle Outlet
1	0.5 MPa	30 °C	10°	0.004246 MPa
2	1.0 MPa	30 °C	10°	0.004246 MPa
3	1.5 MPa	30 °C	10°	0.004246 MPa
4	0.5 MPa	40 °C	10°	0.007383 MPa
5	1.0 MPa	40 °C	10°	0.007383 MPa
6	1.5 MPa	40 °C	10°	0.007383 MPa
7	0.5 MPa	50 °C	10°	0.01235 MPa
8	1.0 MPa	50 °C	10°	0.01235 MPa
9	1.5 MPa	50 °C	10°	0.01235 MPa

Preliminary experimental results showed that the temperature immediately downstream of the nozzle was greatly affected by the reservoir temperature. This is probably because the "drift tube" was directly connected to the reservoir, causing the vapor pressure in that region to approach that of the reservoir. To investigate this effect, two transient tests were conducted. The 10° nozzle with insert swirl angle of 10° was used while maintaining an exit pressure equal to the vapor pressure of the water in the system. The nozzle inlet temperature was maintained at

40 degrees C and the reservoir temperature was allowed to gradually heat up from room temperature, or about 27 degrees C. Data were recorded every 5 minutes to reveal the dependence of nozzle exit temperature on reservoir temperature. Additional measurements were taken for a nozzle inlet temperature maintained at 30 degrees C.

IV.A.4. Experimental procedure for nozzle tests

The following procedure was used to perform the nozzle tests. (Please refer to Figure 14 and Figure 15.)

1. Verify that Valves A and B that isolate the pressure transducers are open. (This is to prevent damage to the pressure transducers, which have a differential pressure limit of 5 psi.)

2. Open ball valves I and J which connect the two sides of pressure transducer LP2 to the system.

3. Fill the cold trap with liquid nitrogen. Periodically refill the cold trap.

4. Start the vacuum pump.

5. Open Valve C from the system to the vacuum pump. Pull the system pressure down to approximately 20 inches of mercury vacuum, as measured on vacuum gauge G1. Close Valve C.

6. Close Valve D from pressure transducer LP1 to the system and open Valves E, F, and G. Valves E, F, and G connect the tubing on either side of pressure transducer LP1 to the vacuum pump. Be sure that the switching valve, Valve H, is turned to the line coming from Valve E. This allows the vacuum pump to pull a hard vacuum for the reference pressure for pressure transducer LP1. The switching valve insures that the mercury manometer is connected to that reference vacuum side.

7. Start the system pump. It will not start below about 25 inches of mercury due to cavitation in the pump.

8. Turn the immersion heater on by adjusting the variable transformer that supplies voltage to the heater.

9. Pull the system vacuum down as far as it will go. This is limited by the vapor pressure of the water in the system. This step should periodically be repeated, but not while data is being recorded.

10. Start the cold water in the heat exchanger. The water is supplied by building cold water lines. Operation at extremely low pressures causes the pump to cavitate and add heat to the system. The heat exchanger removes this added pump heat.

11. Adjust the heater output and the heat exchanger cold water flow rate until the nozzle inlet temperature (Channel 0) is within 2 degrees C of the water reservoir temperature (Channel 4). Wait five minutes for the temperatures to stabilize.

12. Close Valves E, F, and G. Now close Valve A, which activates differential pressure transducer LP1 by closing the tubing that connects the two sides. Open Valve D to read the difference between the system pressure and the reference pressure.

13. Read the reference pressure from the mercury manometer, and enter the reference pressure in the data acquisition program.

14. Close Valve B, which activates differential pressure transducer LP2 by closing the tubing that connects the two sides of this device.

15. Collect the data not automatically obtained by the data acquisition system. This includes the pump exit pressure from gauge G2, the nozzle inlet pressure from gauge G3, and the flow rate from the flowmeter. These values are entered into the data acquisition file as comments. Then the thermocouple and pressure transducer data are recorded using the data acquisition software.

16. The pump exit pressure is controlled by adjusting the bypass valve for the pump using a screwdriver.

17. The inlet temperature is increased by increasing the voltage to the immersion heater with the variable voltmeter. The temperature is decreased by increasing the water flow to the heat exchanger.

18. Data was taken according to the chart of desired data given in Table 2 above. This encompassed 80, 140, and 200 psi pump exit pressures and 30, 40 and 50 degree C nozzle inlet temperatures. As noted above, nozzle swirl angles of 5°, 10°, 15°, and 20° were tested, as well as nozzle exit pressures at the water vapor pressure and atmospheric pressure. This corresponds to a total of 72 tests.

19. Transient tests were run as the tests above with the following exceptions. The heater was adjusted so that the nozzle inlet temperature was the desired value (40 or 30 degrees C). The reservoir temperature was allowed to heat up. Data was taken every 5 minutes until the nozzle inlet temperature and reservoir temperature were within 2 degrees C of each other.

20. Steady-state atmospheric exit pressure tests were referenced to atmospheric pressure, and so the vacuum pump was not needed. The system was opened to the atmosphere until just before the data was taken, as heating and cooling of the water changed the nozzle exit pressure.

IV.B. Velocity Measurements

Two series of laser Doppler velocimeter (LDV) measurements have been conducted in an attempt to verify the performance of the nozzles being developed during Phase I of the research and in preparation for more extensive investigations proposed for Phase II. The proposed measurements should provide important information for optimizing the nozzles during the Phase II research.

IV.B.1. Experimental design

The LDV is unrivaled among velocity instruments for its fundamental simplicity and for its capacity for unintrusive measurement. In the typical dual-beam LDV operating in the differential Doppler mode, a single laser beam is split into two parallel beams which are then focused to cross and interfere in the region where velocity measurements are to be measured. The region where the beams cross is called the measurement volume, and this volume is where the velocity dependent signal is generated. The crossing beams develop a standing pattern of interference fringes which are essentially bright or dark layers in the measurement volume. These fringes are regularly spaced along a line perpendicular to the optical axis, and this is the line along which the velocity component is measured. The principle of operation is quite simple.

A small particle entrained in the flow, such as a water droplet carried along by water vapor, passes from bright fringe to bright fringe and thereby scatters light into a photodetector. In the forward scattering system used in this experiment, the photodetector is mounted on the optical axis opposite the laser. Since the fringes are regularly spaced, the frequency of the light signal scattered into the photodetector as a particle traverses the measurement volume, a so-called "Doppler burst", is proportional to the velocity of the entrained particle and by inference the velocity of the fluid.

A schematic of the LDV test setup is shown in Figure 16. All measurements were conducted using the dual-beam LDV in the Georgia Tech School of Mechanical Engineering shown in Figure 17. This instrument uses a He-Ne laser generating a wavelength of 632.8 nm. Conventional bulk optics are employed including a dual prism beam splitter with a beam spacing of 50 mm and a dual achromatic converging lens assembly with a nominal focal length of 250 mm. These optics result in a measured half-angle of convergence, κ, of 5.558 degrees. This combination of optics and laser results in a fringe spacing, D_f, of 3.267 μm in the measurement volume. This fringe spacing yields a overall sensitivity ratio of entrained particle velocity to Doppler burst frequency of 3.267 m/sec per Mhz. The overall LDV system, comprising photodetector, signal conditioning amplifier, analog to digital converter, and signal processing hardware and software, has a bandwidth of approximately 0 to 50 MHz. This combination of sensitivity and bandwidth implies that a maximum velocity of approximately 150 m/sec could be detected. This maximum velocity should be adequate for all of the nozzle and diffuser flow velocities anticipated in experimental and practical Johnson Tube heat pumps.

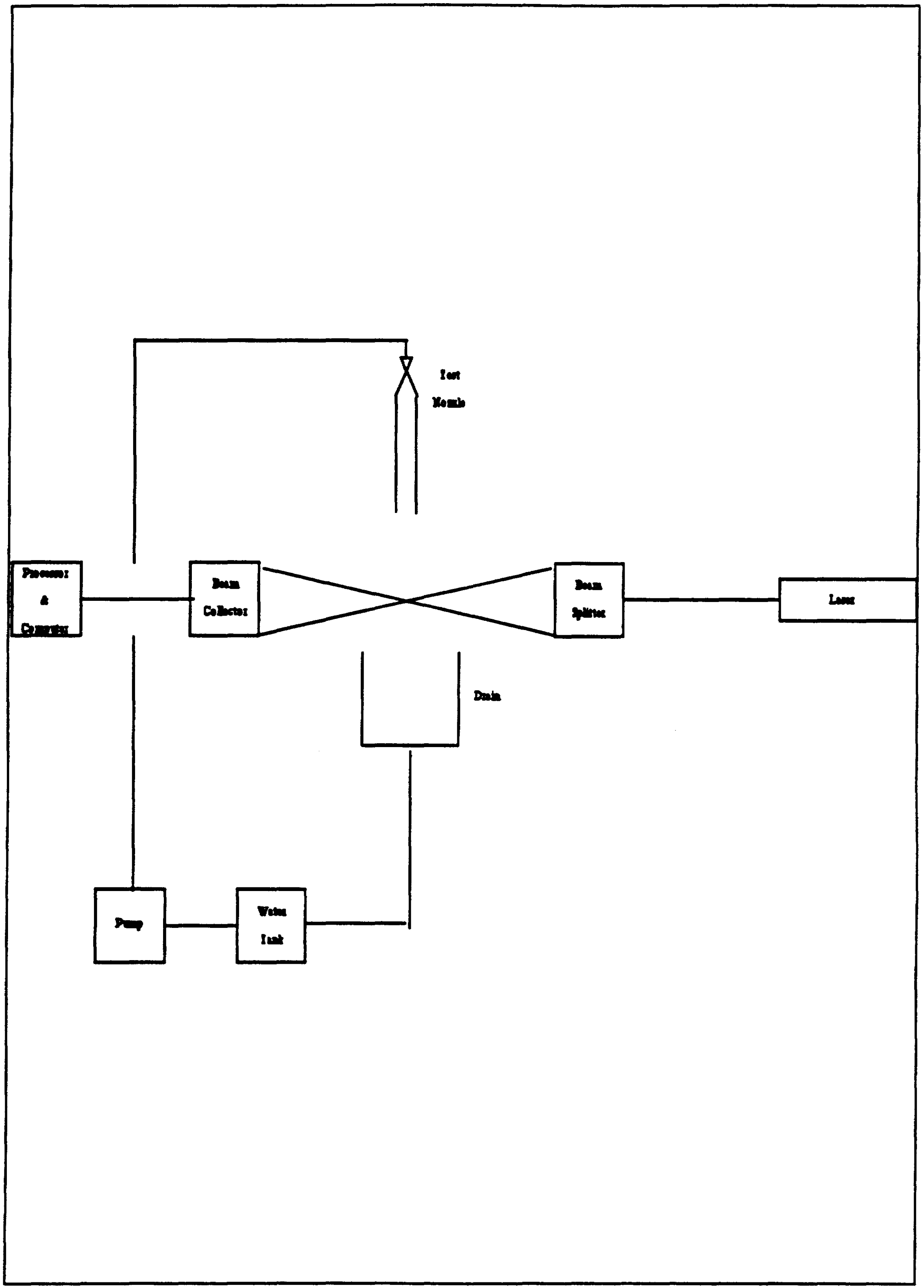

Figure 16: *Test Setup for Measuring Velocity Using Laser Doppler Velocimeter*

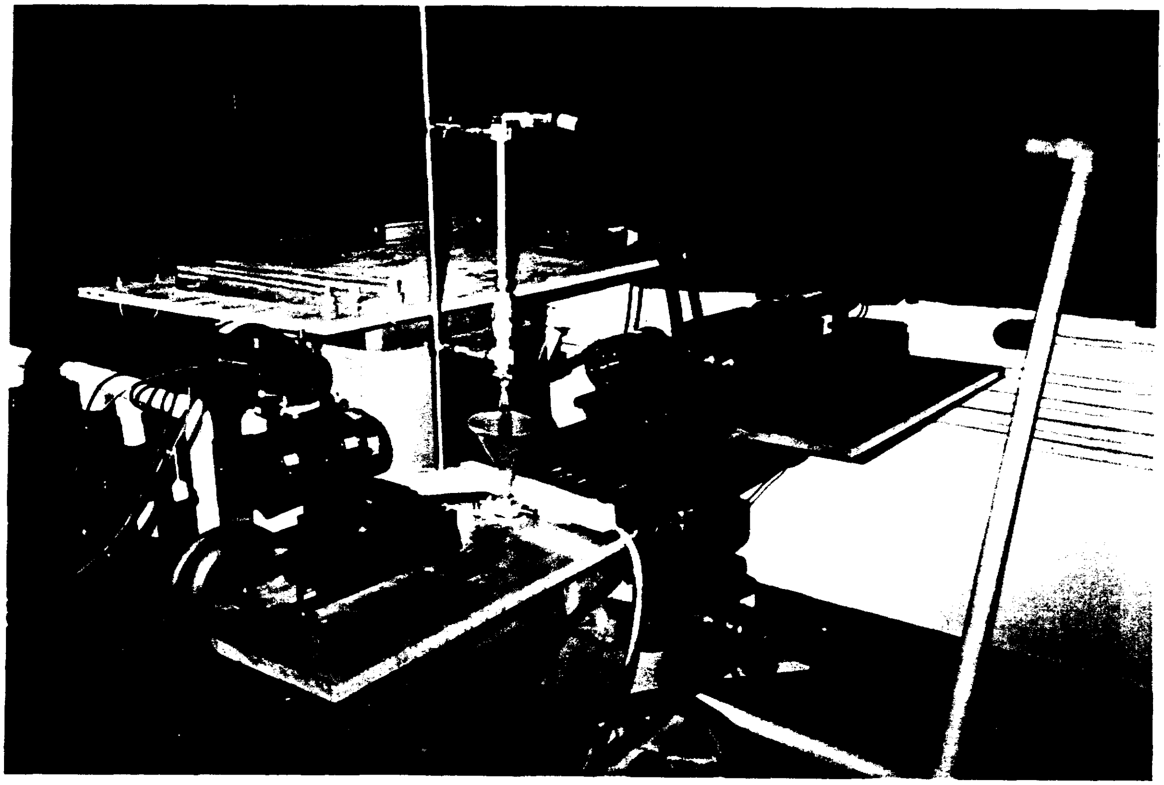

Figure 17: *The Dual-Beam LDV at the Georgia Tech School of Mechanical Engineering*

IV.B.2. Experimental test conditions

The first group of measurements were conducted using a specially designed apparatus which is primarily a 3 inch nominal clear acrylic tube which serves as a receiver and reservoir with an adapter to hold the nozzle block. The nozzle block consisted of a one-half inch diameter clear polymer tube. A high pressure gear pump is provided to recirculate distilled water from the receiver back to the nozzle to allow for continuous operation. While this system was found to be functionally very adequate, the optical quality of the commercial acrylic tube was found to be marginal. Very few Doppler bursts were transmitted to the photodetector, especially when the inner surface of the acrylic tube was covered with a film or droplets of condensed liquid. Since any solution of the optical problems was judged to be problematical and expensive, this system was abandoned in favor of a system to be operated in open air.

In the open air system, drawn glass nozzles discharging into a open sump are used. A more detailed view of one of the glass nozzles is shown in Figure 18. The water is recirculated using a gear pump to recirculate the water. The pressure of the recirculated water is controlled using a combination of the internal bypass in the gear pump and a needle valve in the discharge. Particulate contamination, which could clog the very small diameter throat of the test nozzle, is prevented by a combination of a pipeline strainer and a 15 μm stainless steel filter. The hydraulic subsystem is shown in Figure 19. This overall system was found to be optically adequate but functionally problematical since the discharge back pressure is limited to atmospheric pressure. It would be possible to add a condensing receiver to lower the back pressure, but time and resources did not allow for this additional step. This system did demonstrate that both water droplets in the vapor driven flow and vapor bubbles in a liquid flow could be detected. This important finding indicates that a suitable LDV and appropriate hydraulic and optical system could be used to generate useful diagnostics during Phase II of the proposed research.

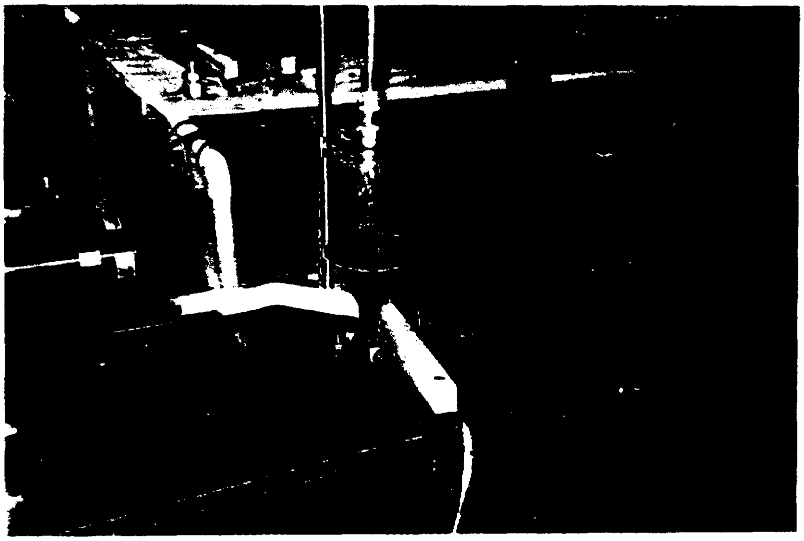

Figure 18: *Detailed View of a Typical Glass Nozzle During LDV Measurements*

(Note the bright red laser light scattered by the flow leaving the nozzle.)

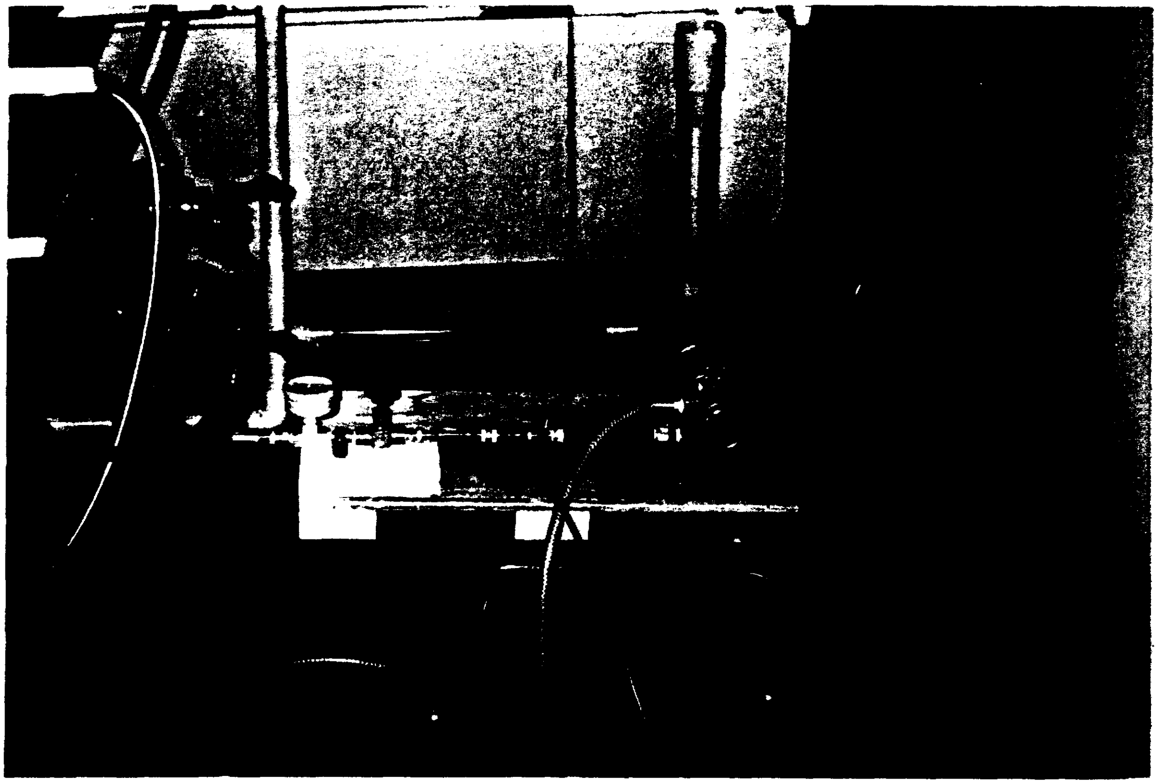

Figure 19: *Hydraulic Subsystem To Supply High Pressure Water During LDV Measurements*

(Note the pump, strainer, filter, needle valve, and pressure gage.)

IV.C. Proof-of-Concept Experiments

IV.C.1. Purpose of experiments

The theoretical predictions made by the computer models are very encouraging regarding the efficiency of the Johnson Tube^{TM} heat pump. Model predictions were based on the homogeneous equilibrium assumptions. In reality, however, the two phases of the fluid may not be in equilibrium. Further, frictional losses in the drift tube and poor heat exchange in the regenerative heat exchanger can significantly affect the performance. Therefore, an overall proof-of-concept experimental facility is needed to determine the actual performance of the Johnson Tube^{TM}. In addition, the test facility can be used to examine the performance of another critical component of the system, namely the adiabatic diffuser at the bottom of the drift tube. This is another component where computer modelling needs to be validated by experimental data since considerable uncertainty exists in the nature of the flow regime within that component.

IV.C.2. Experimental design and construction

A proof-of-concept experimental apparatus was designed using the results of the parametric studies performed with the two-phase computer model along with the nozzle data obtained in the separate effects experiment described in Section IV.A. The existing nozzle test apparatus was modified to incorporate a heat input section, a diffuser, and an annular regenerative heat exchanger section. A bell shaped nozzle with a 10 degree swirl insert was used for these tests. A profile of this shape is illustrated Figure 20. A diffuser section was placed at the bottom of the drift tube. The first diffuser configuration to be tested has a parabolic shape with a 0.041" throat diameter. The throat diameter of the diffuser can be increased, if necessary, during later experiments, to allow the fluid to drain freely from the tube. These experiments will characterize the behavior of the entire Johnson Tube™ heat pump and will allow the computer model to be validated.

Figure 21 shows a schematic of the proof-of-concept experiment. Again, the inlet temperature and pressure are easily varied. The heat input to the load section is provided by nichrome wire wrapped around the copper tubing. The heater is insulated to prevent heat loss. Power is provided to the wire by a variable transformer, which can be adjusted to vary the heat input. The annular regenerative section consists of a 5/8" copper pipe inside a 1" copper pipe. Heat rejection is accomplished by running cool (27 degree C) water through the heat exchanger shown in Figure 21. Thermocouples and pressure taps are located as shown in the schematic. The power input to the load section is obtained by measuring the current and the voltage drawn by the nichrome wire. Temperature measurements at the inlet and exit of the annular regenerative jacket will allow calculation of the heat transferred across the drift tube.

IV.C.3 Experimental test conditions

These experiments characterized the performance of the Johnson Tube™ heat pump. The inlet pressure for the 10 degree linear nozzle and 10 degree inlet swirl that gave the largest temperature drop for the nozzle experiments was 200 psi. The heat rejection temperature was chosen to be 27 °C for comparison with the computer model. A heat input (load section) of 85 W was tested. Measurements of heat input and heat rejected along with a measurement of heat added by the pump were made. Other measurements of temperatures, pressures, and flow rate were also made.

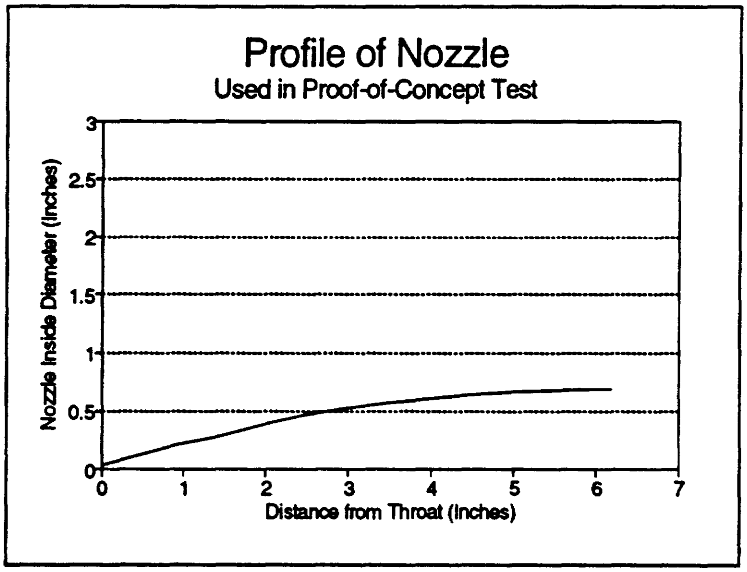

Figure 20: *Profile of Nozzle Used in Proof-of-Concept Experiment*

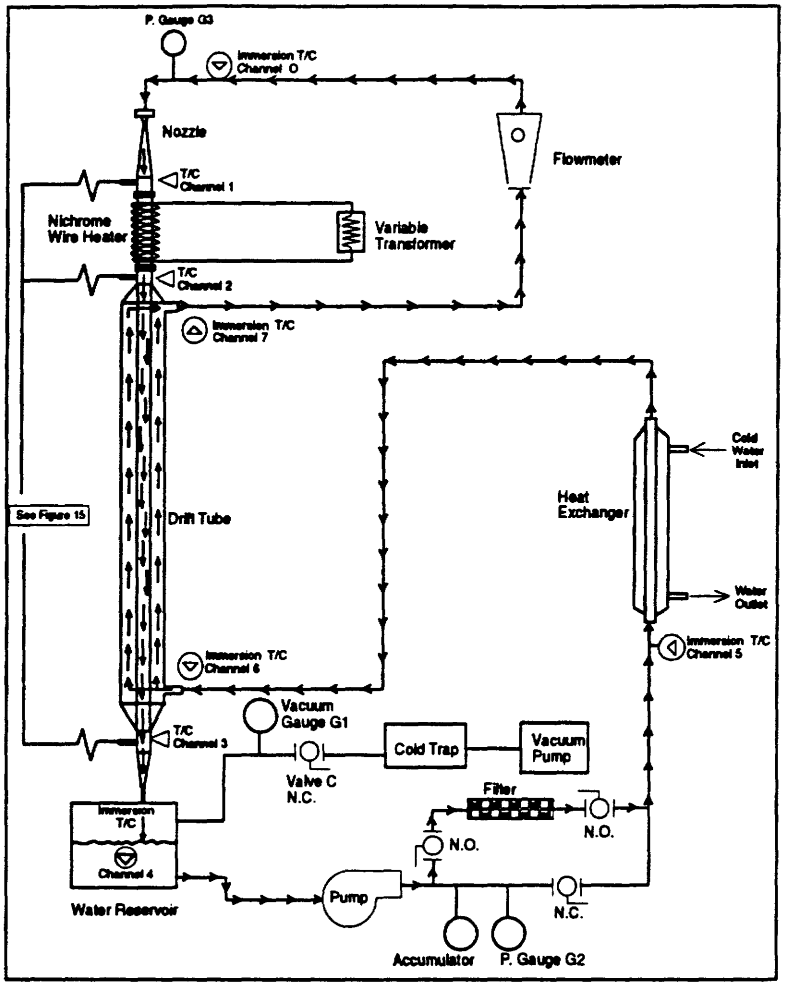

Figure 21: *Proof of Concept Experimental Apparatus*

IV.C.4. Experimental procedure for system tests

The following procedure was used to perform the system tests. (Please refer to Figure 21 and Figure 15.)

1. Verify that Valves A and B that isolate the pressure transducers are open. (This is to prevent damage to the pressure transducers, which have a differential pressure limit of 5 psi.)

2. Open ball valves I and J which connect the two sides of pressure transducer LP2 to the system.

3. Fill the cold trap with liquid nitrogen. Periodically refill the cold trap.

4. Start the vacuum pump.

5. Open Valve C from the system to the vacuum pump. Pull the system pressure down to approximately 20 inches of mercury vacuum, as measured on vacuum gauge G1. Close Valve C.

6. Close Valve D from pressure transducer LP1 to the system and open Valves E, F, and G. Valves E, F, and G connect the tubing on either side of pressure transducer LP1 to the vacuum pump. Be sure that the switching valve, Valve H, is turned to the line coming from Valve E. This allows the vacuum pump to pull a hard vacuum for the reference pressure for pressure transducer LP1. The switching valve insures that the mercury manometer is connected to that reference vacuum side.

7. Start the system pump. It will not start below about 25 inches of mercury due to cavitation in the pump.

8. Turn the load section heater on by adjusting the variable transformer that supplies voltage to the heater. Adjust the voltage until the desired power is being input to the system.

9. Pull the system vacuum down as far as it will go. This is limited by the vapor pressure of the water in the system. This step should periodically be repeated, but not while data is being recorded.

10. Start the cold water in the heat exchanger. The water is supplied by building cold water lines. Operation at extremely low pressures causes the pump to cavitate and add heat to the system. The heat exchanger removes this added pump heat. The heat exchanger will also serve as the heat rejection portion of the cycle. Adjust the water flow rate until the temperature entering the annular regenerator (T6) is 27 °C.

11. Allow five minutes for the system to stabilize and reach steady-state.

12. Close Valves E, F, and G. Now close Valve A, which activates differential pressure transducer LP1 by closing the tubing that connects the two sides. Open Valve D to read the difference between the system pressure and the reference pressure. The pressure line from this valve is connected to two pressure taps, one below the nozzle and one below the load input (heater) section. The pressure of either tap can be measured by clamping off the other hose with hemostats.

13. Read the reference pressure from the mercury manometer, and enter the reference pressure in the data acquisition program.

14. Close Valve B, which activates differential pressure transducer LP2 by closing the tubing that connects the two sides of this device.

15. Collect the data not obtained by the data acquisition system. This includes the pump exit pressure from gauge G2, the nozzle inlet pressure from gauge G3, and the flow rate from the flowmeter. These values are entered into the data acquisition file as comments. Then, the thermocouple and pressure transducer data is recorded using the data acquisition software. The pressure of the two taps connected to Valve D cannot be measured at the same time, so one should be recorded with an appropriate comment and then the other immediately following.

16. The pump exit pressure was controlled by adjusting the bypass valve for the pump using a screwdriver. For these tests, the inlet pressure was set to 200 psi.

17. Data was taken for a heat inputs of 85 W.

V. THEORETICAL RESULTS

V.A. Model Validation

An intensive literature survey revealed the existence of a limited amount of experimental data from a two-phase supersonic nozzle experiment [8]. The data from that experiment were used to verify the thermal-hydraulic computer models developed in this investigation. The inlet temperature of the water was 60 °C while the inlet pressure was 68 kPa. The throat diameter was approximately 1.9 mm, the exit diameter was 18 mm, and the nozzle angle was 6.9°. The vapor exit velocity was about 200 m/s, while the liquid droplet velocity was only about 40 m/s. The exit pressure and temperature were 2 kPa and 303 K, respectively.

The computer models developed under this contract were used to predict nozzle exit conditions for the same geometry and inlet conditions used in the experiment. The homogeneous-equilibrium model predicted a velocity of 50 m/s at the nozzle exit, which, as expected, is between the measured separate phase velocities. A plot of mixture velocity versus axial position from the nozzle throat as predicted by the homogeneous-equilibrium model is shown in Figure 22. Our dynamic slip model predicted a gas velocity of 370 m/s and a liquid droplet velocity of 40 m/s at the nozzle exit, which are in reasonably good agreement with the experimental values of 200 m/s and 40 m/s. The predicted results of vapor and liquid velocities versus axial position down the nozzle are shown in Figure 23. For both analyses presented above (Figure 22 and Figure 23) the critical flow conditions at the nozzle throat were calculated using the homogeneous-equilibrium option.

The exit pressures were also calculated and compared with the experimental data. Variation of pressure with axial position along the nozzle as predicted by the homogeneous-equilibrium model is shown in Figure 24; similar results for the dynamic slip model are shown in Figure 25. The homogeneous-equilibrium model predicted an exit pressure of 10 kPa, while the dynamic slip model predicted an exit pressure of 2 kPa. The actual measured exit pressure was 4 kPa. Again, the dynamic slip model gives good results when compared with the experiment. Exit temperatures predicted by the homogeneous-equilibrium model and the dynamic slip model were 320 K and 293 K respectively. The experimentally measured exit temperature was 303 K, again agreeing reasonably well with the dynamic slip model prediction.

In conclusion, the theoretical models have been verified by comparison with two-phase supersonic water flow experimental data.

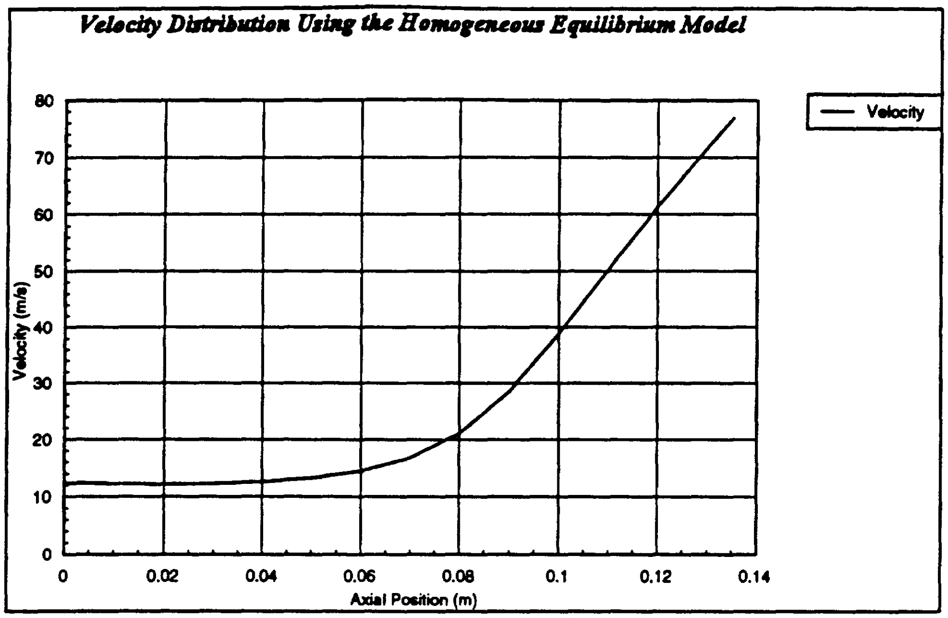

Figure 22: *Predicted Velocity Distribution Using the HEM*

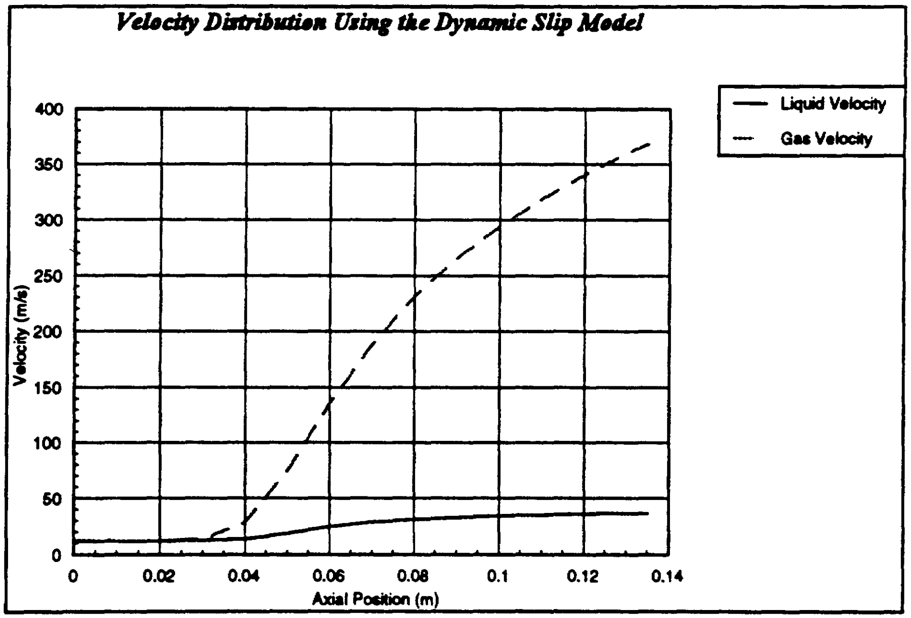

Figure 23: *Variation of the Liquid and Vapor Velocities with Axial Position for the DSM*

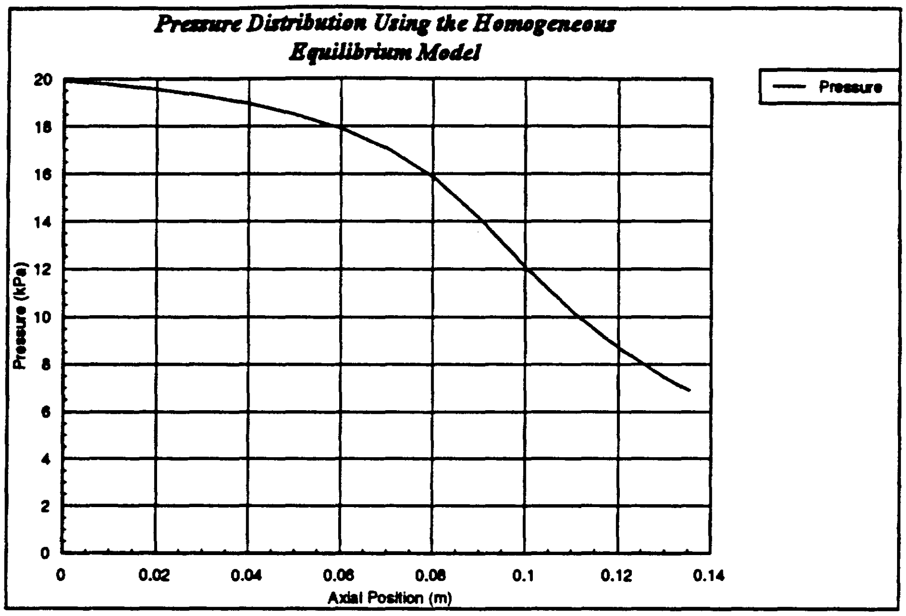

Figure 24: *Predicted Pressure Distribution Using the HEM*

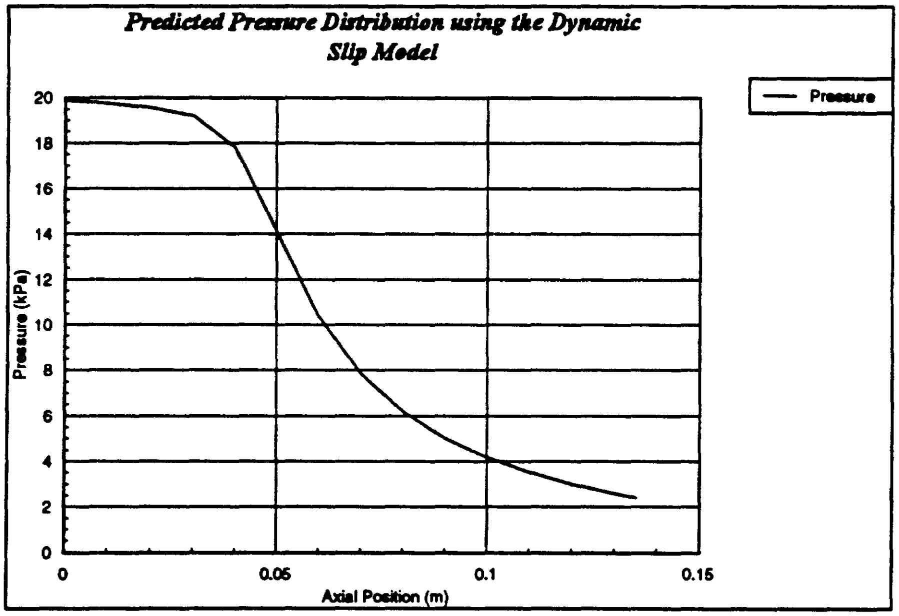

Figure 25: *Predicted Pressure Distribution Using the DSM*

V.B. Parametric Studies

The two-phase computer model was used to perform parametric studies to predict nozzle performance. In addition, the integrated two-phase and thermodynamic model was used to parametrically assess the performance of the entire Johnson Tube™ cycle and its sensitivity to friction and regenerative heat exchange effectiveness. Theoretical results of the nozzle performance study and overall system performance are described below.

V.B.1. Two-phase parametric study of nozzle performance

Nozzle efficiency is crucial to the performance of the Johnson Tube™ heat pump. The nozzle performance is determined by the inlet conditions of the fluid as well as the geometry of the nozzle. Preliminary experiments using different throat to exit diameter ratios have shown that a 10 degree (total included angle) linear nozzle with a 10 degree inlet swirl produces good performance with significant atomization at the nozzle exit. Therefore, parametric calculations were performed for this nozzle geometry (throat to exit diameter ratio) to characterize the effects of the inlet conditions on nozzle performance. Inlet pressures were varied from 0.5 to 2.0 MPa while the inlet temperature was varied from 10 °C to 50 °C, for a total of twenty cases. The nozzle throat diameter was kept constant and equal to 0.030 inches. Typical results are given in Figures 25 - 28. The results show the predicted values of mass flow rate, exit temperature, temperature drop across the nozzle, and exit velocity for each case. As one would expect, Figure 26 illustrates that the mass flow rate is nearly independent of the inlet temperature and, conversely, is highly dependent on the inlet pressure. Figure 27 and Figure 28 illustrate the significant effect of both inlet pressure and temperature on the temperature difference across the nozzle. Figure 29 illustrates the effect of the inlet pressure and temperature on the nozzle exit velocity. The data points depicted in Figures 25 - 27 represent our nozzle test results described in Section VI.A.

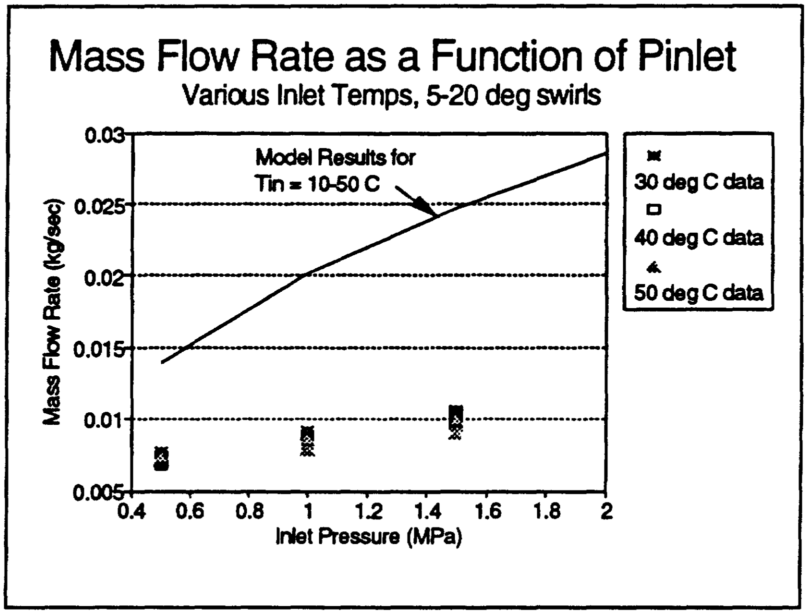

Figure 26: *Mass Flow Rate versus Nozzle Inlet Pressure*

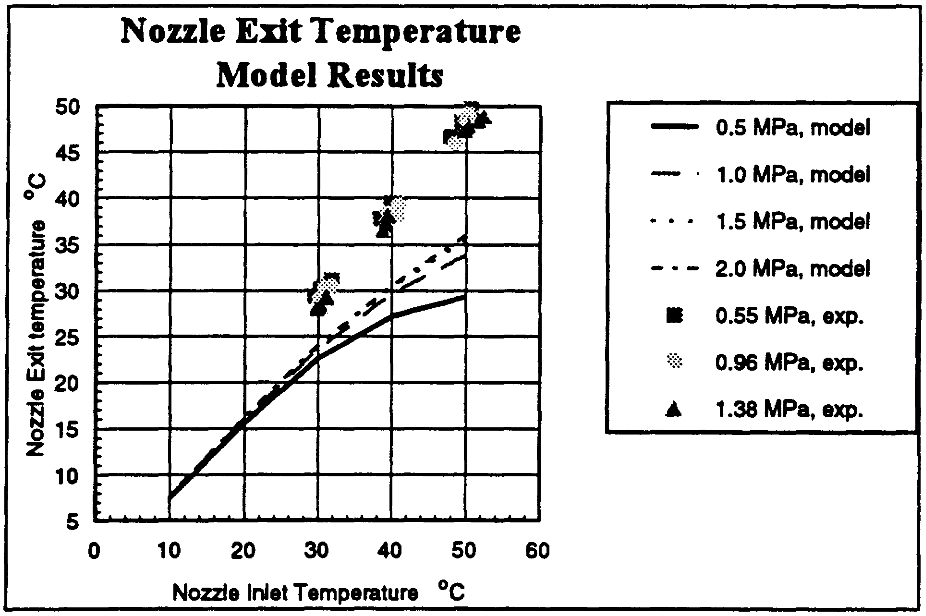

Figure 27: *Nozzle Exit Temperature versus Inlet Pressure*

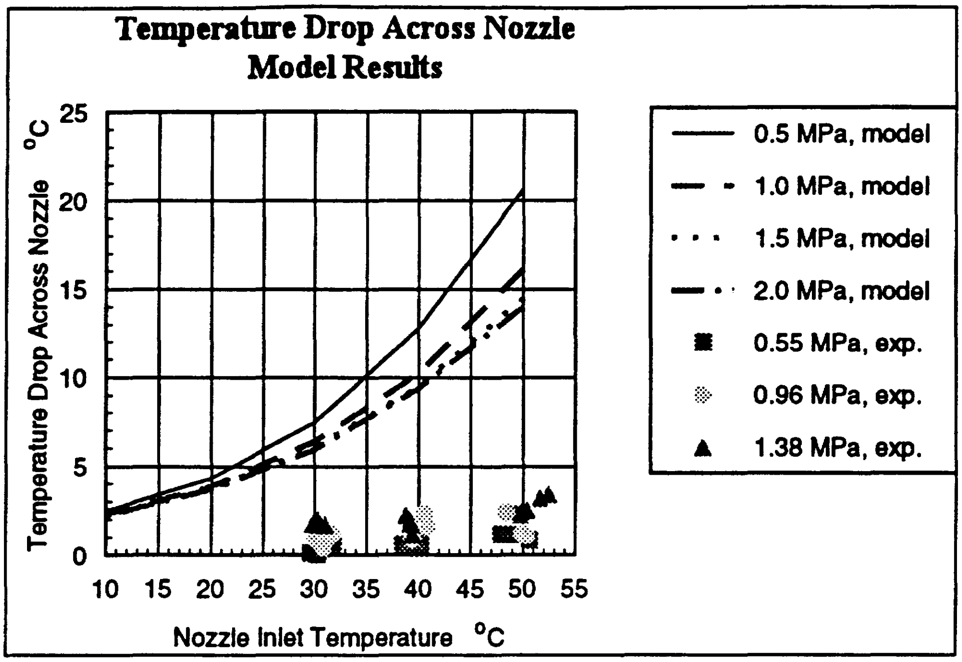

Figure 28: *Temperature Drop Across Nozzle*

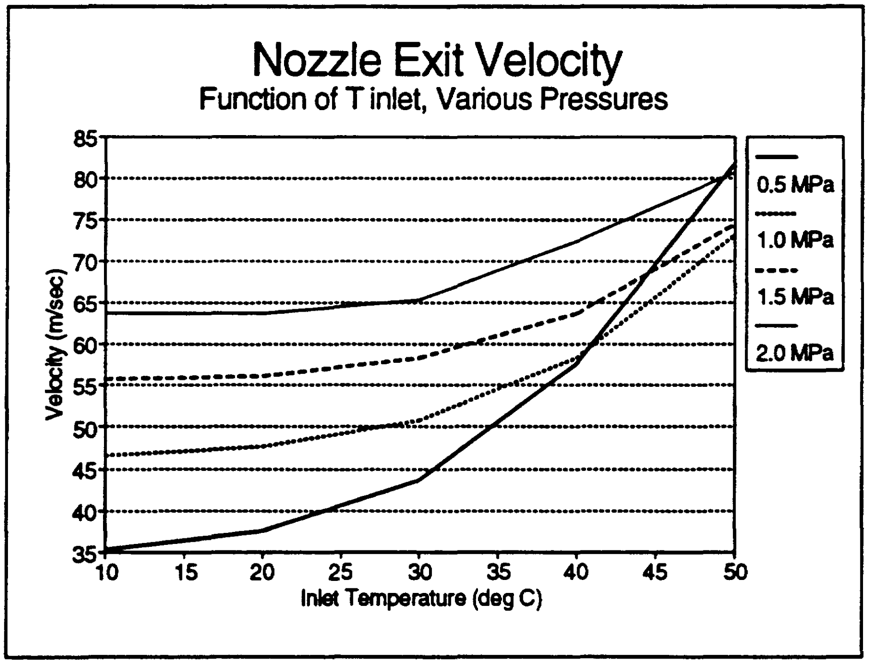

Figure 29: *Nozzle Exit Velocity versus Inlet Pressure*

V.B.2. Parametric studies for overall system performance

The two-phase computer model described in Section III.A was integrated into the thermodynamic model described in Section III.B. In this manner, the detailed computations for the nozzle, drift tube, and diffuser, including regenerative heat exchange in the drift tube, were included in an overall system model. This model was used to investigate the effects of nozzle inlet conditions on the overall performance of the cycle. Parametric studies were performed for an inlet temperature of 20 °C and inlet pressures ranging from 0.5 MPa to 2.0 MPa. In order to provide a consistent means for comparing the results, the heat sink temperature (T_6 in Figure 2) was fixed at 27 °C. For each set of inlet conditions (pressure and temperature), several computer runs were performed using different heat inputs. These values were then used to determine the heat input for each inlet condition which resulted in a minimum heat rejection temperature (T_6) of 27 °C (See Figure 30). A plot of the heat input versus inlet pressure is shown in Figure 31. The corresponding coefficient of performance was then determined and plotted in Figure 32. The Carnot efficiency calculated for these cases using the average heat input and rejection temperatures varies from 26.0 to 29.0.

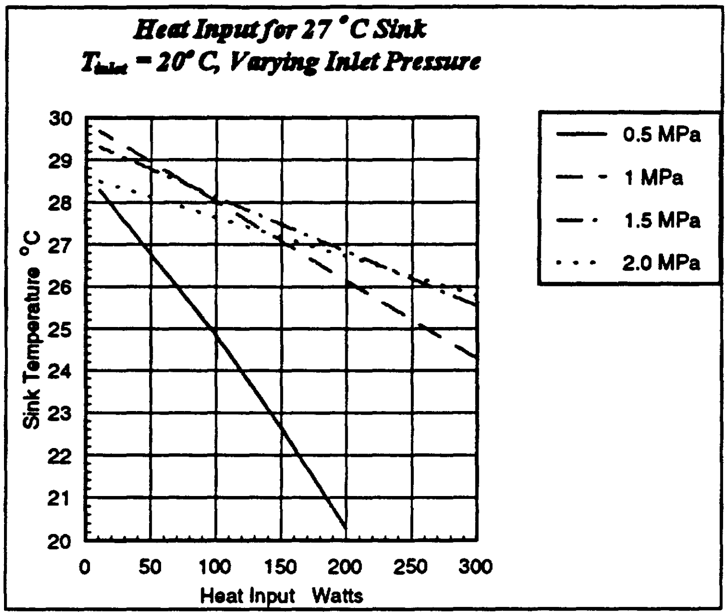

Figure 30: *Select Heat Input for 27°C Sink Temperature*

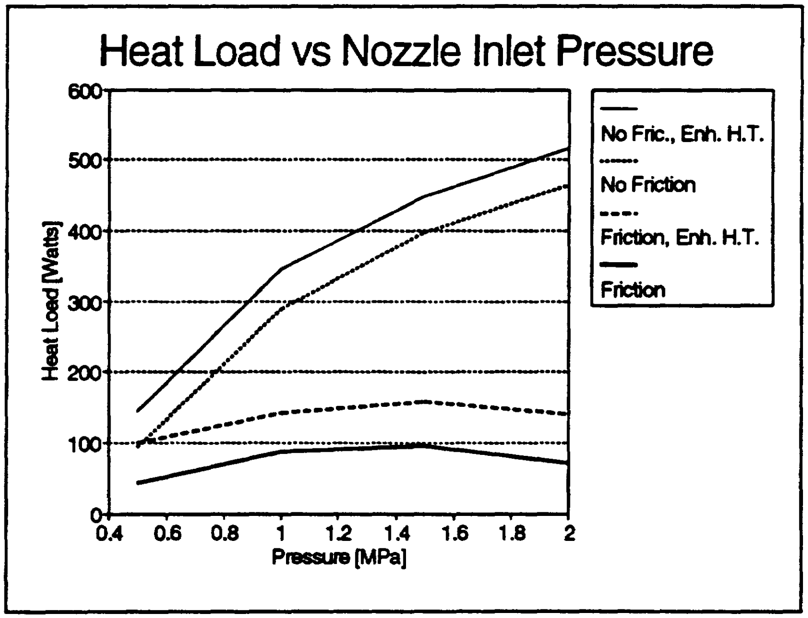

Figure 31: *Heat Load versus Nozzle Inlet Pressure*

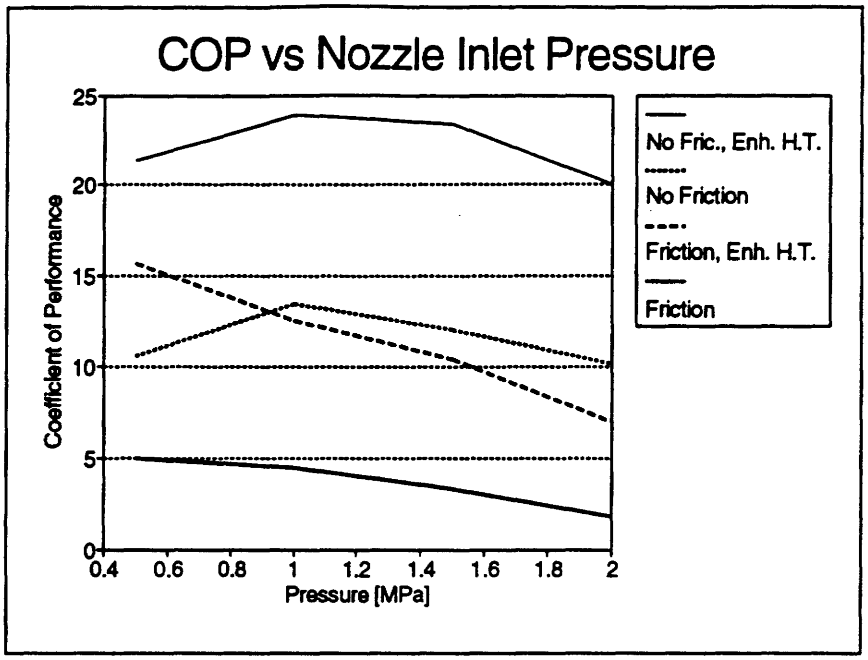

Figure 32: *COP versus Nozzle Inlet Pressure*

V.B.2.a. Effects of friction and heat transfer enhancement

The effects of friction and regenerator heat transfer enhancement on system performance were examined for a 20 °C inlet temperature with inlet pressures ranging from 0.5 MPa to 2.0 MPa. Computer runs were performed with and without friction and with and without enhanced heat transfer. The friction and heat transfer were calculated using the correlations in the computer model (Section III.A). The heat transfer coefficients on both sides of the regenerator were multiplied by a factor of 10 to give the "enhanced heat transfer" values. The pump was estimated to be 80% efficient. Figure 31 shows the effects of friction and the overall heat transfer coefficient in the regenerative heat exchanger on the thermal load corresponding to a minimum heat rejection temperature of 27 °C. In Figure 32, the detrimental effects of friction and poor heat transfer on the overall cycle COP are obvious. The Carnot efficiency calculated using the average heat input and rejection temperatures of these cases ranges from 26.0 to 29.0.

For cases with no friction and enhanced regenerative heat exchange, the COP for the Johnson Tube^{TM} approaches the corresponding values for the Carnot cycle.

V.B.2.b. Optimum operating conditions for experimental system

Based on the parametric studies described above, it is clear that for a given nozzle inlet temperature and heat sink temperature, there is an optimal nozzle inlet pressure. Referring to Figure 32 (for a nozzle inlet temperature of 20 °C and heat sink temp of 27 °C), the optimum inlet pressure for the selected Johnson Tube^{TM} geometry ranges from 1.0 MPa for the case of enhanced heat transfer and no friction to 0.5 MPa for nominal heat transfer and nominal friction. The proof-of-concept experimental facility described in Section IV.C was designed in a flexible manner to allow operation over a wide range of conditions including the optimum conditions identified in the parametric study. It is also apparent that the overall performance of the system can be significantly improved by decreasing friction and increasing the overall heat transfer coefficient in the regenerative heat exchanger.

VI. EXPERIMENTAL RESULTS

VI.A. Nozzle Performance Tests

To date, several different nozzle configurations have been tested. The nozzle with the best performance, among those examined so far, has a 10 degree total included angle. Experimental data indicate that the nozzle can produce a temperature drop of up to 3.5 °C with significant atomization indicated by the appearance of a fine white mist downstream from the nozzle. The results of the nozzle tests described in Section IV.A are given below.

VI.A.1. Steady state tests

Figures 33 - 37 illustrate the effect of inlet pressure and temperature on the nozzle temperature drop. The ten degree nozzle discussed above was used here with inlet swirl inserts with various swirl angles. The results from each swirl angle are plotted separately in Figure 33 - 36; the data are combined in Figure 37. These tests were run with a nozzle exit pressure equal to the vapor pressure of water at the reservoir temperature. These data show that although there is a small difference in nozzle temperature drop for the different swirl angles, the ten degree swirl gives consistently higher temperature drops at the higher inlet pressures. The data show that the nozzle temperature drop increases with inlet temperature and inlet pressure. As predicted theoretically, Figure 38 shows that the mass flow rate is essentially independent of inlet temperature, but strongly dependent on inlet pressure.

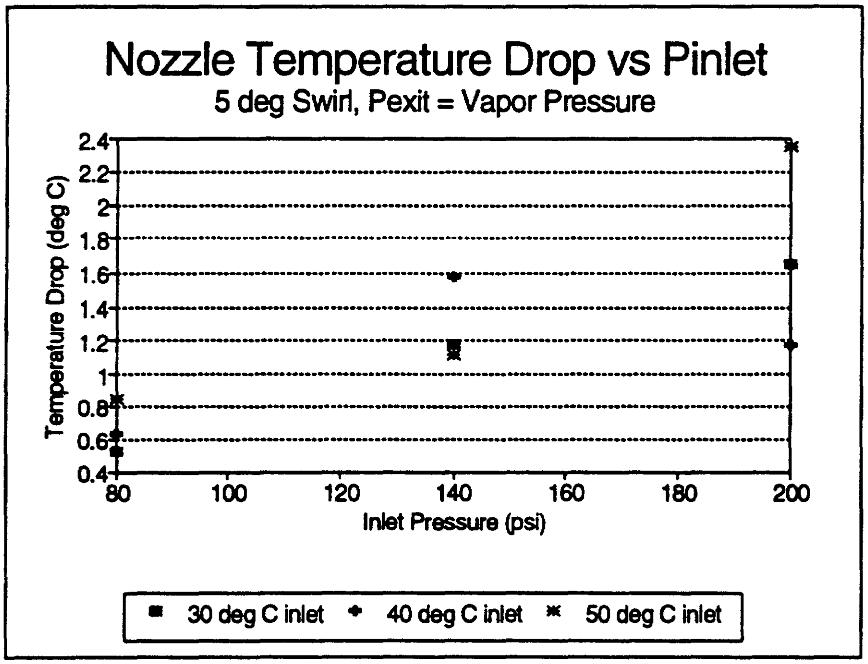

Figure 33: *Temperature Drop Across Nozzle, Five Degree Swirl,*
P_{exit} = *Vapor Pressure*

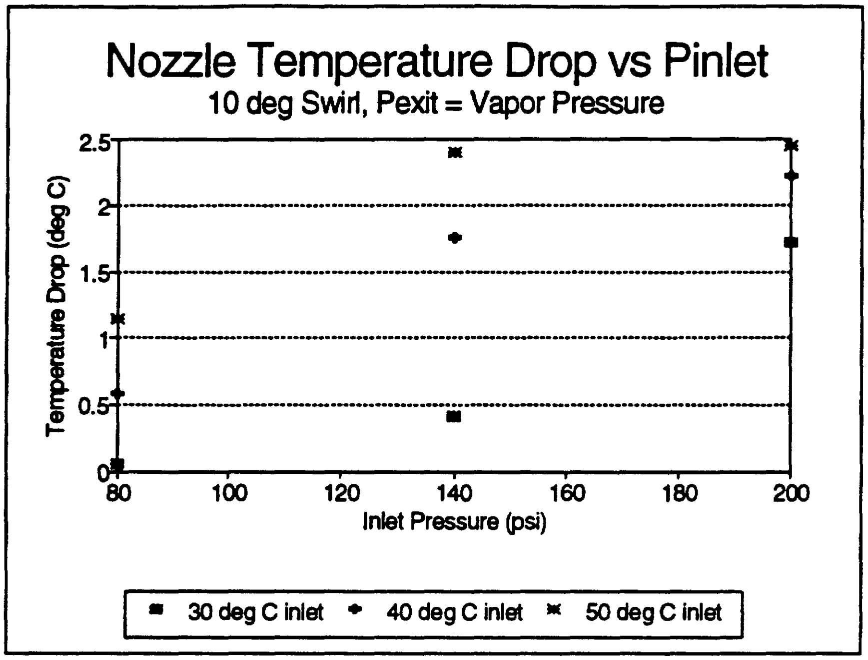

Figure 34: *Temperature Drop Across Nozzle, Ten Degree Swirl,* P_{exit} *= Vapor Pressure*

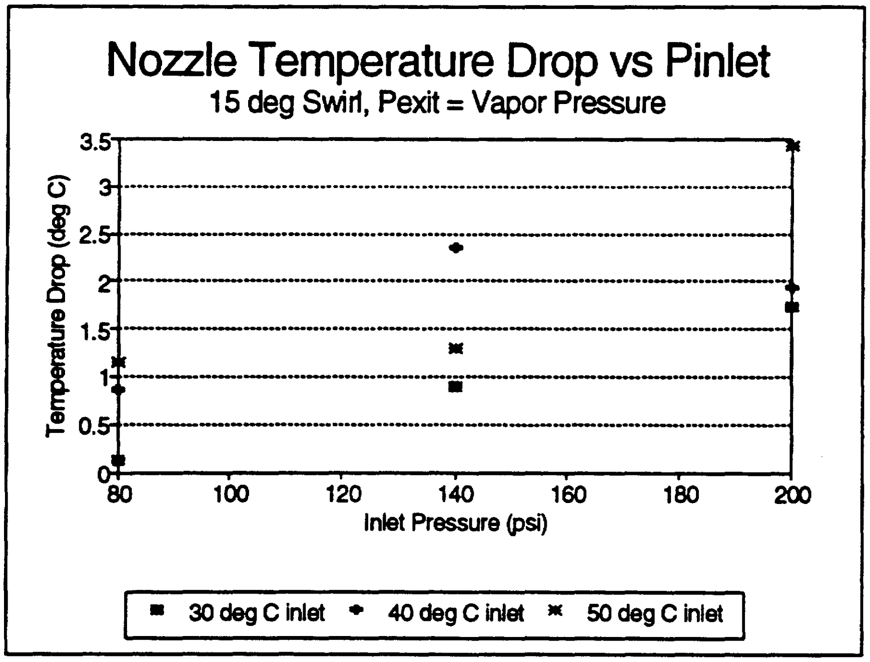

Figure 35: *Temperature Drop Across Nozzle, Fifteen Degree Swirl,* P_{exit} *= Vapor Pressure*

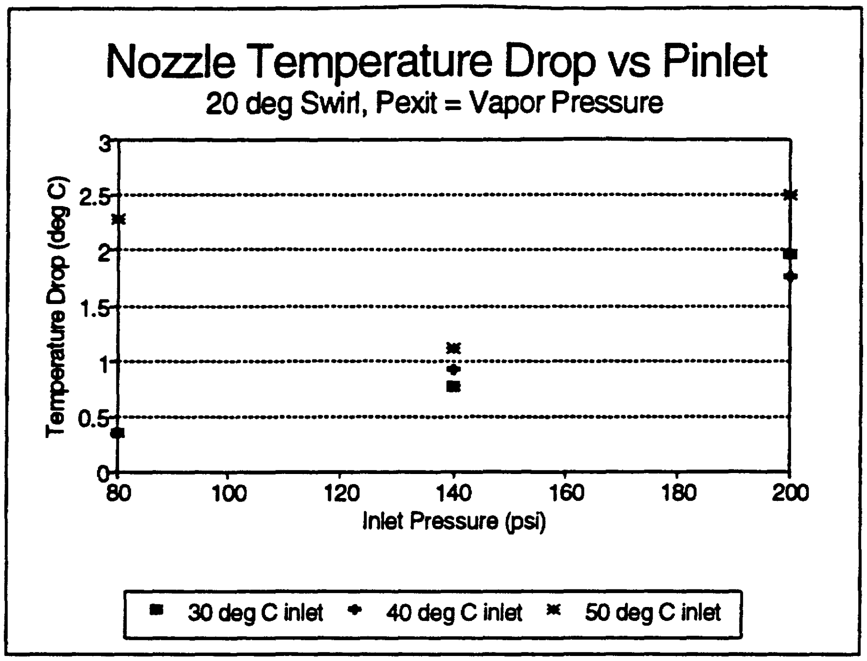

Figure 36: *Temperature Drop Across Nozzle, Twenty Degree Swirl, P_{exit} = Vapor Pressure*

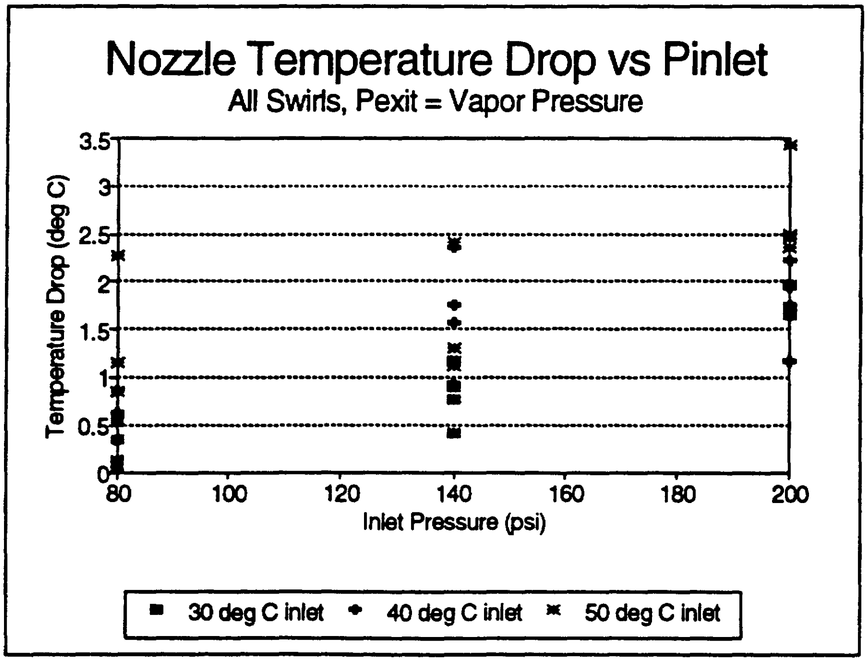

Figure 37: *Temperature Drop Across Nozzle, All Swirls, P_{exit} = Vapor Pressure*

VI.A.2. Transient tests

Transient experiments were conducted to investigate the effect of the water reservoir temperature on the nozzle exit temperature. Tests were run using a 1.38 MPa (200 psi) inlet pressure and inlet temperatures of 40 and 30 degrees C. The results, plotted in Figures 38 - 41, respectively, show that the nozzle exit temperature is strongly dependent on the water reservoir temperature. Values of the temperature drop across the nozzle are significantly higher than those obtained in the steady state tests presented in Section VI.A.1.

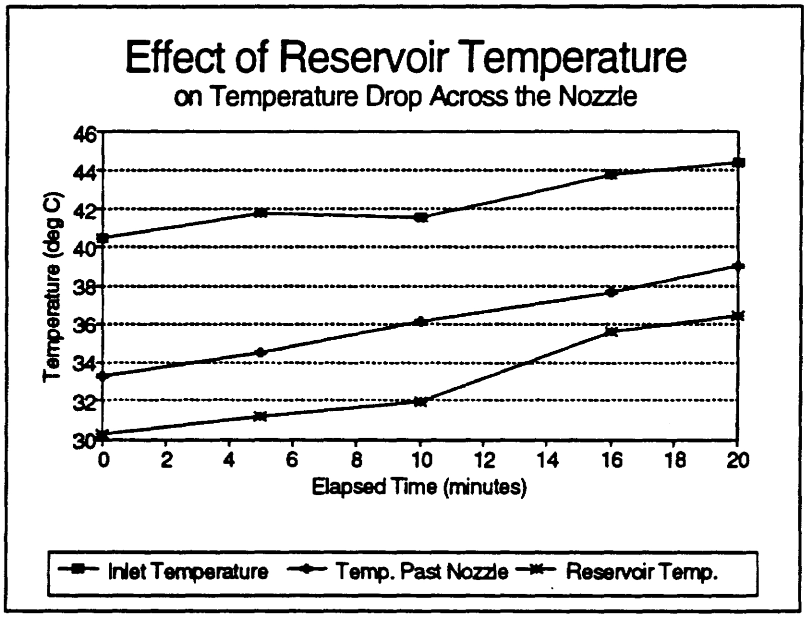

Figure 38: *Effect of* $T_{reservoir}$ *on Temperature Drop Across Nozzle (40 °C Inlet Temperature)*

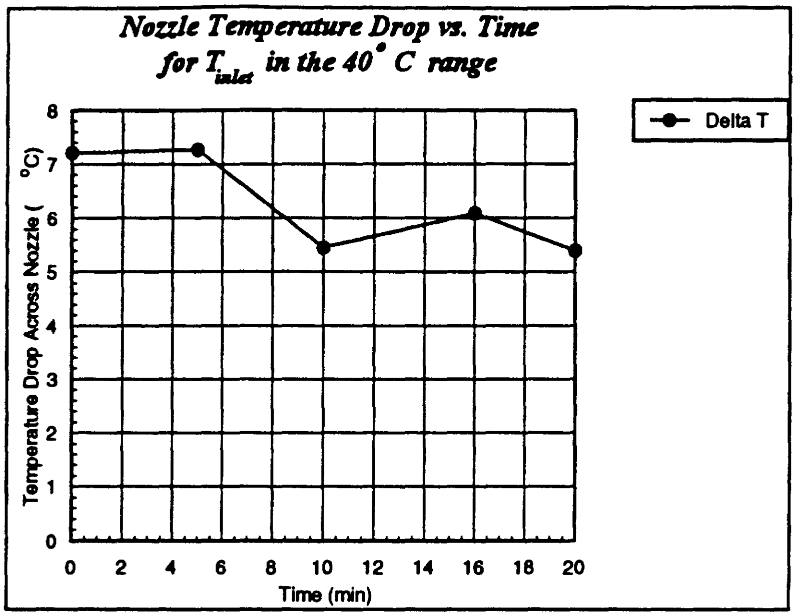

Figure 39: *Transient Temperature Drop Across Nozzle for T_{inlet} in the 40°C range*

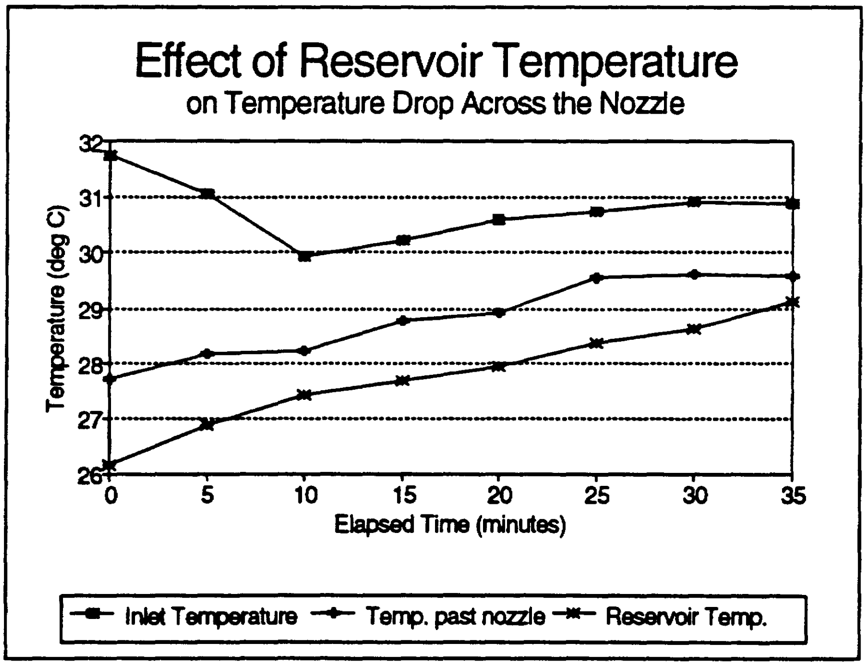

Figure 40: *Effect of $T_{reservoir}$ on Temperature Drop Across Nozzle (30 °C Inlet Temperature)*

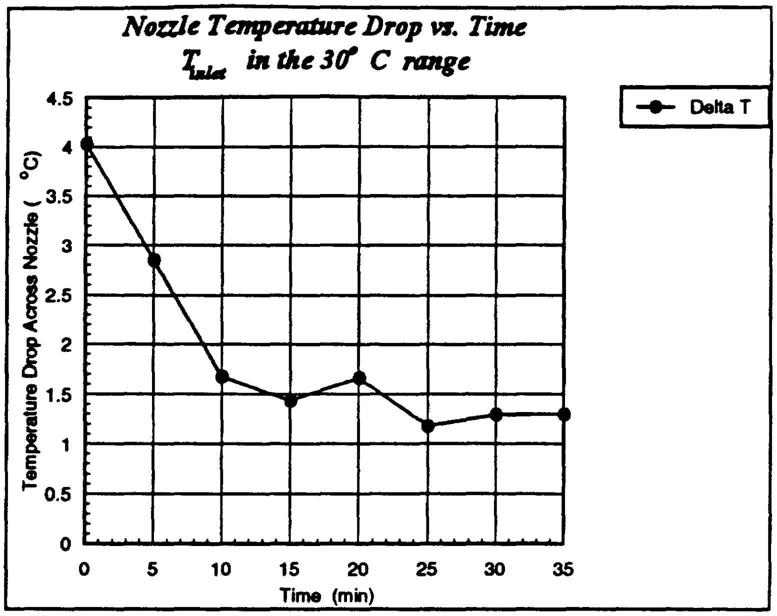

Figure 41: *Transient Temperature Drop Across Nozzle for T_{inlet} in the 30°C range*

VI.A.3. Atmospheric exit pressure tests

Figures 42 - 45 illustrate the effect of inlet pressure and temperature on the temperature drop across the nozzle. The ten degree nozzle with various swirl inlet angles was tested with atmospheric exit pressure. These data show that the temperature drop across the nozzle increases with inlet temperature and decreases with increasing inlet pressure. Figure 46 shows that the mass flow rate is essentially independent of inlet temperature, but strongly dependent on inlet pressure, as predicted theoretically. As expected, the temperature drops across the nozzle for atmospheric exit pressure are significantly lower than those attained with the exit pressure under vacuum.

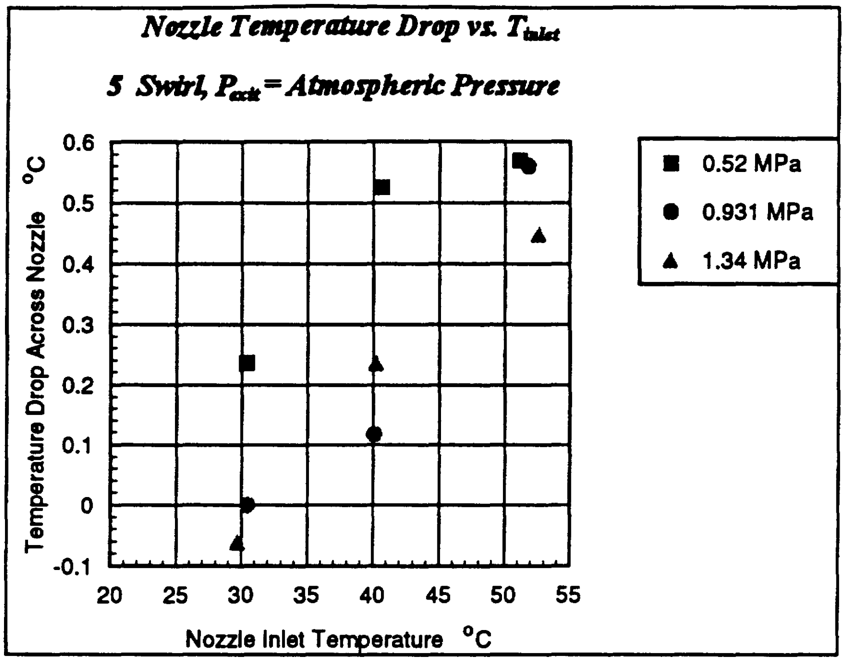

Figure 42: *Temperature Drop Across Nozzle, Five Degree Swirl, P_{exit} = Atmospheric Pressure*

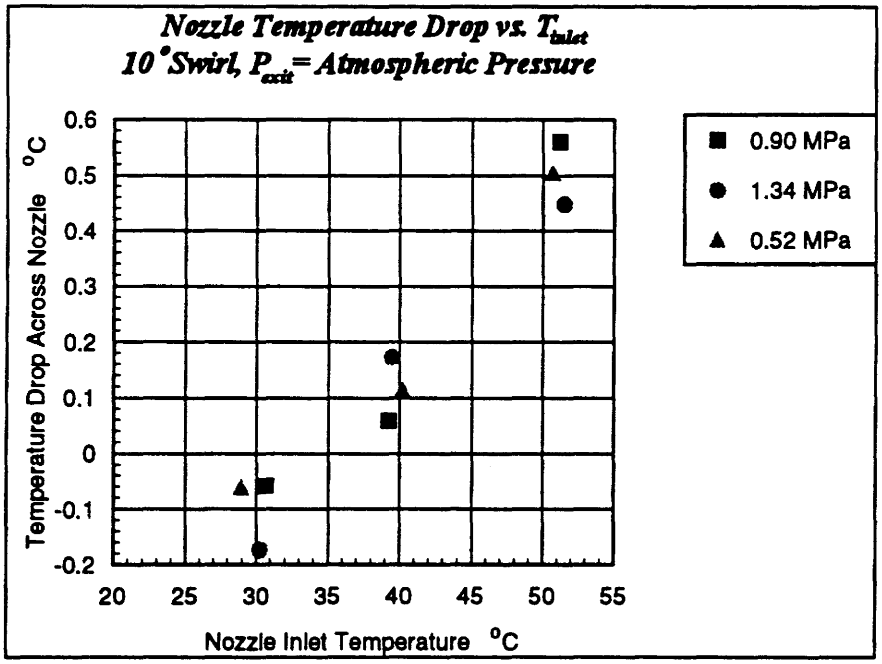

Figure 43: *Temperature Drop Across Nozzle, Ten Degree Swirl, P_{exit} = Atmospheric Pressure*

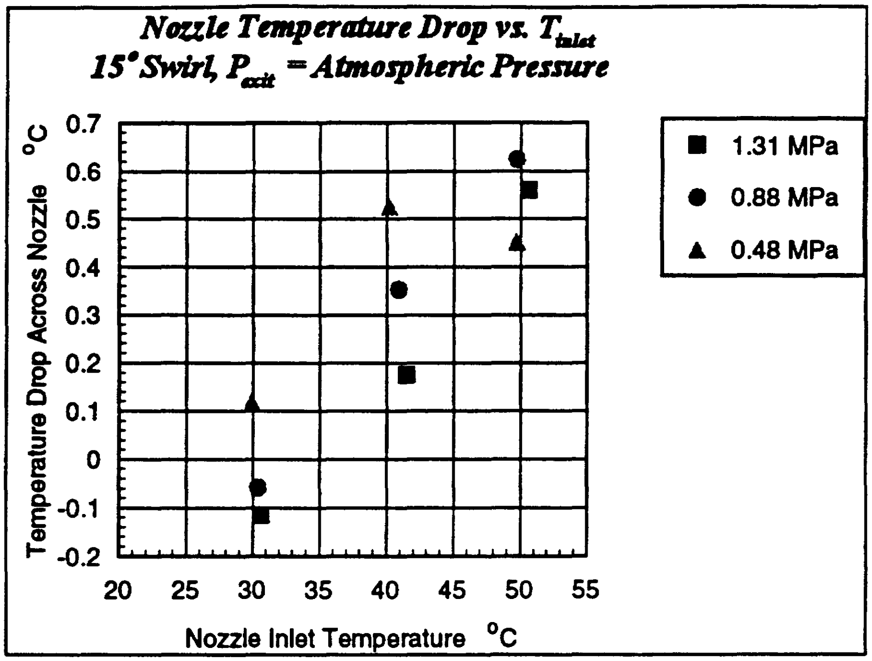

Figure 44: *Temperature Drop Across Nozzle, Fifteen Degree Swirl, P_{exit} = Atmospheric Pressure*

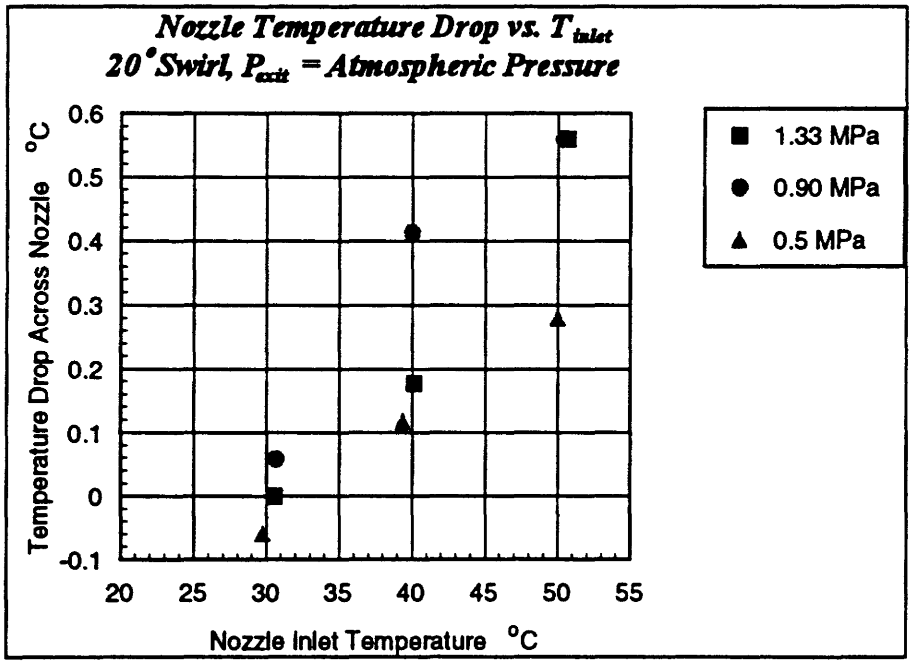

Figure 45: *Temperature Drop Across Nozzle, Twenty Degree Swirl, P_{exit} = Atmospheric Pressure*

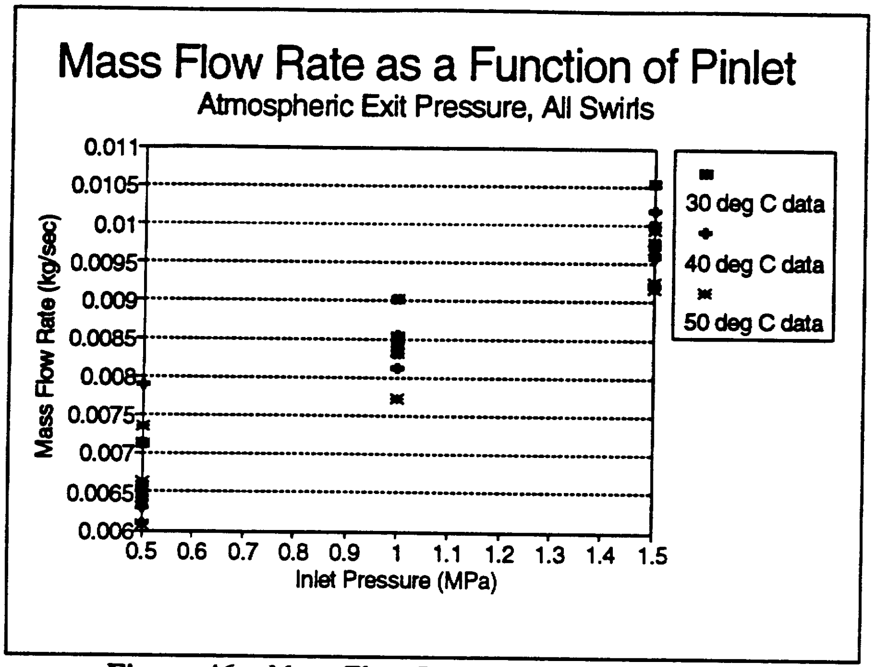

Figure 46: *Mass Flow Rate as a Function of* P_{inlet},
P_{exit} = *Atmospheric Pressure*

VI.B. LDV Velocity Measurements

The two glass nozzles tested demonstrated quite different performance as might be expected since there was no opportunity to optimize the design or fabrication of the nozzles. The first nozzle test generated only a rather distinct jet; a separated flow with little atomization. Even so, we were able to observe very distinct Doppler bursts and generated the velocity histogram shown in Figure 47. The low velocity indicated that this is a low performance nozzle as might be surmised from the fact that the nozzle only generated a jet. The cylindrical bore in the throat of this nozzle was possibly too long. The long cylindrical bore would lead to excessive losses and separation explaining the poor performance. The second nozzle exhibits entirely different behavior. Rather than a separated jet, an attached region of predominantly liquid flow with dispersed vapor bubbles and some evidence of recirculation was formed. Possibly this nozzle has a throat that is too short, approximating an orifice. Even though the flow was dramatically different, excellent Doppler bursts were observed as seen in the example given in Figure 48.

The experience with the LDV measurements indicates that either type of two phase flow, distributed droplets of liquid or distributed bubbles of vapor, can be investigated with the available instrumentation. While neither glass nozzle exhibited the desired high velocity and effective atomization, it is apparent that in one case the throat was too long and in the other too short. A nozzle with a geometry intermediate of the two units tested would no doubt perform much better. Overall then, the development of an effective nozzle and its successful characterization by LDV measurements during Phase II both appear to be highly probable.

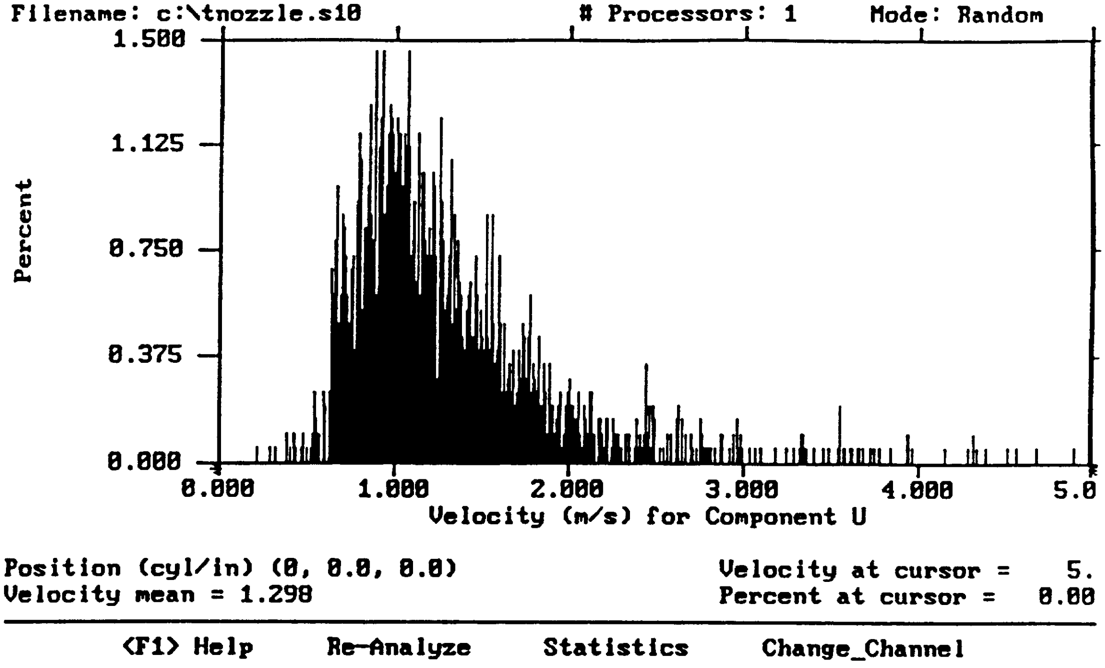

```
Filename: c:\tnozzle.s10              # Processors: 1      Mode: Random

Position (cyl/in) (0, 0.0, 0.0)                 Velocity at cursor =    5.
Velocity mean = 1.290                           Percent at cursor =   0.00
```

Figure 47: *Velocity Histogram Generated During Test of First Nozzle*

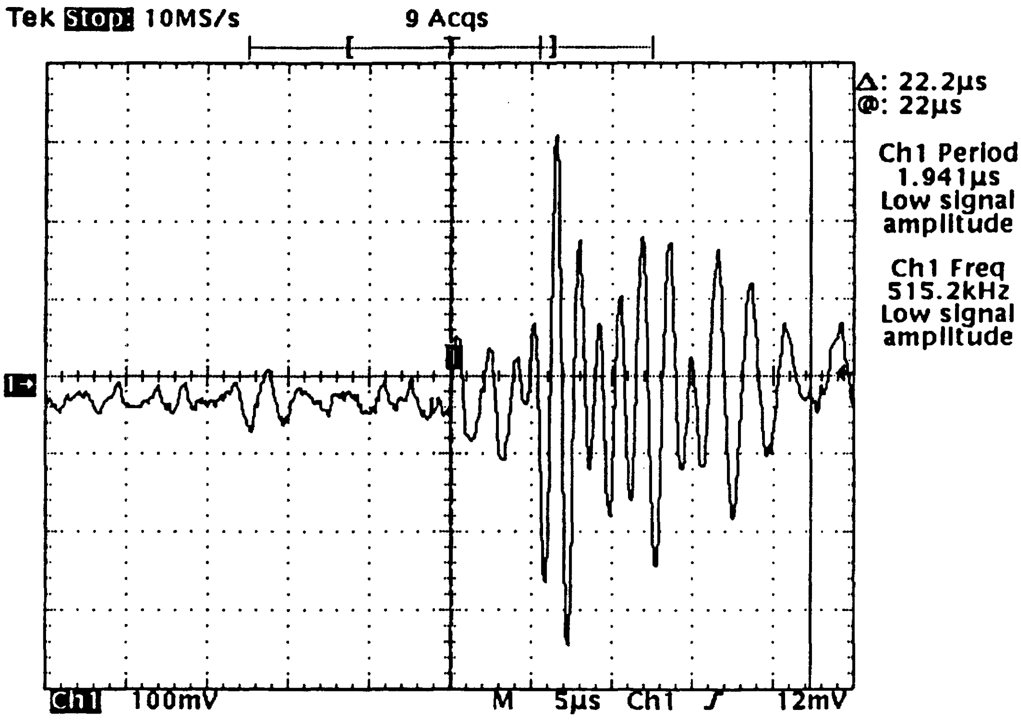

Figure 48: *Doppler Burst Observed During Test of Second Nozzle*

VI.C. Overall System Results

Experimental results of the overall Johnson Tube^{TM} system showed that separated two-phase flow occurs in the nozzle and drift tube. Homogeneous flow, as well as enhanced regenerative heat transfer are needed for proper performance of the device. Experimental data are given in Appendix C.

VII. DISCUSSION AND CONCLUSIONS

VII.A. Theoretical Work

Two-phase thermal hydraulic models for flow in the nozzle, drift tube, and diffuser based on either a homogeneous equilibrium model, a dynamic slip mode, and a fully separated flow model have all been developed. These models have been incorporated into a general thermodynamic model of the Johnson Tube^{TM} heat pump.

Predictions of the two-phase flow models developed in this investigation were compared with the published data for two-phase flow in a supersonic convergent divergent nozzle [8]. The dynamic slip model predicted a gas velocity of 370 m/s and a liquid droplet velocity of 40 m/s at the nozzle exit, which are in reasonably good agreement with the experimental values of 200 m/s and 40 m/s. The homogeneous equilibrium model predicted a velocity of 50 m/s at the nozzle exit, which, as expected, is between the measured separate phase velocities. The homogeneous equilibrium model predicted a nozzle exit pressure of 10 kPa, while the dynamic slip model predicted an exit pressure of 2 kPa. The measured exit pressure was 4 kPa. Again, the dynamic slip model gives good agreement with the experimental values confirming its validity.

Model results were also compared with data from the nozzle performance experiments conducted under this contract. Although the mass flow rate of the nozzle was lower than that predicted by the model, both experimental and theoretical trends were the same. The mass flow rate through the nozzle increased with increasing inlet pressure and only increased slightly with increasing temperature as predicted theoretically. The temperature drop across the actual nozzle was smaller than that predicted by the model. Some of this difference was probably due to the sensitivity of the experimental temperature drop to changes in temperature (i.e. vapor pressure) in the water reservoir at the bottom of the drift tube.

Parametric studies were performed to quantify the effects of various parameters on the overall performance of the Johnson Tube^{TM} heat pump. The results indicate that COPs near those for a Carnot cycle can be theoretically achieved. The actual performance is affected significantly by both frictional losses in the system and the heat transfer effectiveness in the regenerator section, as illustrated in Figure 32. The results indicate that for a given geometry and nozzle inlet temperature, there is an optimum nozzle inlet pressure which maximizes the cycle COP. For the parameters selected (T_1 = 20° C and T_6 = 27° C), the optimum value for the cycle maximum pressure ranged from 0.5 MPa for a nominal friction and regenerative heat exchanger to 1.0 MPa for a negligible friction and enhanced regenerative heat exchanger.

The model was used to select the design and operational parameters for the proof-of-concept test facility.

VII.B. Experimental Work

Three types of experiments were conducted during Phase I. Experiments of the first type were aimed at quantifying the performance of various nozzle designs within the range variables expected in the proof-of-concept facility. The data showed an increase in temperature drop across the nozzle with increasing inlet temperature, as predicted theoretically. However, while the model predicts a slight increase in temperature drop with decreasing inlet pressure, the experiment yielded the opposite results. Based on these experiments, an appropriate nozzle design for the proof-of-concept facility was selected.

The second type of experiments were aimed at measuring the two-phase velocities at the nozzle exit using laser doppler velocimetry. Preliminary velocity measurements were made for the selected nozzle design; the results indicate the suitability of this experimental technique for nozzle design optimization.

In the third type of experiments, a proof-of-concept test facility for the entire Johnson Tube™ heat pump was constructed and tested. Experimental results showed a need for enhanced regenerator heat transfer as predicted by the models. Also, the results showed a need for more homogeneous flow behavior. This homogeneous flow behavior can be achieved by reducing the drop size as predicted in the dynamic slip model. The COPs can be greatly improved by optimizing the various Johnson Tube™ components in accordance with the model predictions. Enhancement of the regenerator heat transfer will be necessary to approach Carnot efficiency.

Extensive theoretical calculations for the Johnson Tube™ heat pump is a highly efficient device, suitable for external thermal control of manned spacecraft. Experimental results show that homogeneous two-phase flow and improved heat transfer in the regenerator are required for proper operation of the Johnson Tube™. The feasibility of the Johnson Tube™ has been shown. The device's potentially high efficiency, simplicity, and lack of CFC's make it very attractive for both commercial and spacecraft applications. Future work will focus on optimization of the device's components to improve its efficiency and establish its economic viability.

VII.C. Future Work

The theoretical and experimental work performed under this contract has resulted in significant progress toward realizing a practical working model of a Johnson Tube heat pump. The key areas on which follow on work must focus have been identified. Specifically these areas include:

Enhanced heat transfer in the regenerative heat exchanger

Heat transfer in the regenerative heat exchanger is crucial for achieving the temperature lifts desired for this system. The model developed is based on conventional convective heat transfer relations. However, enhanced heat transfer based on phenomenon such as mass transport (heat pipe) technology and ultrasonically enhanced convective heat transfer needs to be investigated. A longer drift channel would have improved the performance significantly. The short length of the drift channel used in the experiment did not allow sufficient thermal coupling between the two phase mixture in the drift channel and the counter flowing liquid in the annulus. Although the desired temperature drop occurred at the nozzle exit, inside the drift channel, the induced temperature change in the annular flow was only a few tenths of a degree.

Selection of design features that minimize friction losses

Scaling the system up (increasing its physical size) should reduce losses associated with friction significantly. The diffuser and nozzle become much more effective and friction losses will per unit mass flow will be reduced. Friction losses could not be observed in the experiment. Limited heat transfer in the regenerative heat exchanger limited operation of the heat pump to such an extent that other performance parameters were obscured.

Increasing the diameter of the drift channel will reduce the ratio of wall surface area to mass flow and thereby reduce friction loses per unit mass.

Improved homogeneous behavior of the two phase fluid in the drift channel

Our observations along with the limited data available from literature suggest that performance of the drift channel could be improved significantly by reducing the drop size of the liquid phase in the drift channel sufficiently to achieve homogeneous behavior. In addition to optimizing the design of the nozzle, ultrasonics could be introduced to achieve a drop size on the order of one micron which would give homogeneous behavior.

The observed performance without homogeneous behavior indicates the only a limited pressure difference between the inlet and exit ends of the drift channel could be realized. Significant pressure differences would result in counter flow of vapor up the drift channel and thereby mitigate itself along with the corresponding temperature difference between the two ends. A smaller drop size would eliminate this problem.

The problem is also reduced with increased length of the drift channel. The pressure gradient over a longer channel would be less given the same temperature and pressure difference b between the ends. The longer channel will allow more time for heat transfer and momentum coupling between the two phases. Optimized pressurization pump design Constant temperature heat transfer between the heat source and sink. Test results from the experimental set up confirmed model predictions to the extent that the minimal performance achieved could be measured. Model predictions indicate that performance will be minimal unless there is enhanced heat transfer near homogeneous behavior of the working fluid and reduced friction losses. The results achieved were consistent with model predictions.

VIII. REFERENCES

1. Van Wylen, G.J., and Sonntag, R.E., *Fundamentals of Classical Thermodynamics*, John Wiley and Sons, Inc., (1967).

2. Fairchild, P.D., Fischer, S.K., and Hughes, P.J., "Global Warming Impacts of CFC Alternative Technologies: Combining Fluorocarbon and CO_2 Effects," IEA Heat Pump Center Workshop Report, Merlinger, Switzerland, October 12-13, 1992, prepared by the Oak Ridge National Laboratory for the U.S. Department of Energy.

3. Johnson, L.G., "Johnson Tube^{TM}, a Thermodynamic Heat Pump," U.S. Patent Number 4,724,683, February 16, 1988.

4. Moody, F.J., "Maximum Flow Rate of a Single Component, Two-Phase Mixture," J. Heat Transfer, 1965, pp. 53-58.

5. Henry, R.E., and Fauske, H.K., "The Two-Phase Critical Flow of One-Component Mixtures in Nozzles, Orifices, and Short Tubes," J. Heat Transfer, 1971, pp. 179-187.

6. Leung, J.C., "A Generalized Correlation for One-Component Homogeneous Equilibrium Flashing Choked Flow," AIChE J., 1986, Volume 32, p. 1743.

7. Leung, J.C., and Grolmes, M.A., "A Generalized Correlation for Flashing Choked Flow of Initially Subcooled Liquid," AIChE J., 1988, Volume 34, p. 688.

8. Hijikata, K., Mori, Y., Nagasaki, T., and Sonada, Y., "Fundamental Study on Production of High-Speed Mist Flow by Expansion of Low-Temperature Hot Water," Nippon Kikai Gakkai Ronbunshu B Hen 51, n 463, Mar 1985, pp. 1017-1025.

9. R.V. Liles et al., "TRAC-PF1/MOD1: An Advanced Best Estimate Computer Program for Pressurized Water Reactor Thermal-Hydraulic Analysis." US Nuclear Regulatory Commission Report *NUREG/CR-3858* (1986).

10. V.H. Ransom, R.J. Wagner, J.A. Trapp, L.R. Feinaner, G.W. Johnsen, D.M. Kiser, and R.A. Reimke. "RELAP5/MOD2 Code Manual, Volume 1: Code Structure, Systems Models, and Solution Methods." US Nuclear Regulatory Commission Report *NUREG/CR4312* (1985).

11. J.H. McFadden, et al., "RETRAN-03: A Program for Transient Thermal-Hydraulic Analysis of Complex Fluid Flow Systems, Vol. 1: Theory and Numerics," Electric Power Research Institute Report EPRI NP-7450 (1992).

12. J.C. Leung and M. Epstein, "Flashing Two-Phase Flow Including the Effect of Noncondesible Gases," J. Heat Transfer, Vol. 113, pp. 269-272.

13. S. Levy, "Predictions of Two-Phase Critical Flow Rate," J. Heat Transfer, Vol. 87, pp.53-58 (1965).

14. H.J. Richter, "Separated Two-Phase Flow Model: Application to Critical Two-Phase Flow," Int. J. Multiphase Flow," Vol. 9, pp.511-530 (1983).

15. F. Dobran, "Nonequilibrium Modelling of Two-Phase Critical Flows in Tubes," J. Heat Transfer, Vol. 109, pp. 731-737 (1987).

16. G. Yadigaroglu and R.T. Lahey, Jr., "On the Various Forms of the Conservation Equations in Two-Phase Flow," Int. J. Multiphase Flow, Vol. 2, pp. 477-494 (1977).

17. R.T. Lahey, Jr., and F.J. Moody, *The Thermal-Hydraulics of a Boiling Water Reactor*, 2nd ed., American Nuclear Society, 1993.

18. M. Soliman, J.R. Schuster, and P.J. Berenson, "A General Heat Transfer Correlation for Annular Flow Condensation," J. Heat Transfer, Vol. 90, pp. 267-276 (1968).

19. J.G. Collier, *Convective Boiling and Condensation*, 2nd ed., McGraw-Hill, 1981.

20. J.C. Chen, "A Correlation for Boiling Heat Transfer to Separated Fluids in Convective Flow," Paper presented at 6th National Heat Transfer Conference, Boston, 1963.

21. N.E. Todreas and M.S. Kazimi, *Nuclear Systems I*, Hemisphere (1990).

22. A.F. Mills, *Heat Transfer*, Irwin, Boston, Massachusetts, 1992.

23. V.V. Klimenko, "A Generalized Correlation for Two-Phase Forced Flow Heat Transfer," Int. J. Heat Mass Transfer, Vol. 31, pp. 541-552 (1988).

24. V. Gnielinski, "Neue Gleichungen für Wärme-und Stoffübergang in Turbulent Durchströmten Rohren und Kanälen," Forsh. Gelo. Ing Wes, Vol. 41, pp. 8-16 (1975).

25. M. Ishii and N. Zuber, "Drag Coefficient and Relative Velocity in Bubbly, Droplet or Particulate Flows," AIChE Journal, Vol. 25, pp. 848-855 (1979).

26. Y. Taitel, D. Bornea, A.E. Dukler, "Modelling Flow Pattern Transitions for Steady Upward Gas-Liquid Flow in Vertical Tubes," AIChE Journal, Vol. 26, pp. 345-354 (1980).

27. R. Clift, J.R. Grace, and M.E. Weber, *Bubbles, Drops, and Particles*, Academic Press, (1978).

28. K.W. McQuillan, and P.B. Whalley, "Flow Patterns in Vertical Two-Phase Flow," International Journal of Multiphase Flow Vol. 11, pp. 161-175 (1985).

29. R.S. Broadkey, *The Phenomena of Fluid Motion*, Addison-Wesely Press (1967).

30. G.B. Wallis, *One-Dimensional Two-Phase Flow*, McGraw-Hill (1969).

31. L. Von Wijngaarden, "Hydrodynamic Interaction Between Gas Bubbles in Liquids," J. Fluid Mechanics, Vol. 77, pp. 27-44 (1976).
32. D.K. Edwards, V.E. Denny, and A.F. Mills, "Transfer Processes, 2nd Ed.," Hemisphere Publishing Corp., New York (1979).

33. R. Kronig and J.C. Brink, "On the Theory of Extraction from Falling Droplets," Applied Scientific Res., Vol A2, pp. 142-154 (1951).

34. W.E. Ranz and W.R. Marshall, "Evaporation from Drops," Chem. Eng. Progress, Vol. 48, pp 141-146 (1952).

35. P.V. Danckwerts, "Significance of Liquid-Film Coefficients in Gas Absorption," Ind. Eng. Chem., Vol. 43, pp. 1460-1467 (1951).

36. H.S. Carlslaw and J.C. Jaeger, *Condition of Heat in Solids*, 2nd Edition, Oxford Science Publications, 1959.

37. L.J. Huang and P.S. Ayyaswamy, "Heat and Mass transfer Associated with a Spray Drop Experiencing Condensation: A Fully Transient Analysis," Int. J. Heat Mass Transfer, Vol. 30, pp. 881-891 (1987).

38. Sir H. Lamb, *Hydrodynamics*, 6th Ed., Cambridge University Press, (1932).

39. L. Haar, J.S. Gallagher, and G.S. Kell, *NBS/NRC Steam Tables*, Hemisphere Publishing Company, Washington (1984).

40. A.C. Hindmarsh, "LSODE and LSODI. Two New Initial Value Ordinary Differential Equation Solvers," *ACM Newsletter*, Vol. 15, No. 4, pp.10-11 (1980).

NOMENCLATURE

A	cross sectional area [m^2]
$\boldsymbol{A}$	coefficient matrix as defined in Equation (40)
C	column vector as defined in Equation (40)
C_d	drag coefficient [-]
c_{fi}	interface friction factor in annular flow regime [-]
c_p	constant pressure specific heat [J/kg K]
c_v	constant volume specific heat [J/kg K]
C_{VM}	virtual mass force coefficient [-]
d	bubble or droplet diameter [m]
$\boldsymbol{D}$	binary mass diffusivity [m^2/s]
D_h	hydraulic diameter [m]
e	total enthalpy [J/kg]
f	fanning friction factor : frequency [-] : [1/s]
F	frictional force per unit mixture volume: constant in Chen's correlation [N/m^3]:[-]
g	gravitational constant [m/s^2]
G	mass flux [kg/m^2]
$\hat{h}$	specific enthalpy [J/kg]
h	convective heat transfer coefficient [W/m^2 K]
j	superficial velocity [m/s]
k	thermal conductivity [W/m K]
K	Interface momentum transfer coefficient: convective mass transfer coefficient [kg/m^2 s]
L_c	Laplace constant [m]
M	molecular mass number [kg/kg mole]

$\dot{m}$	mass flow rate [kg/s]
Nu	Nusselt number [-]
P	pressure [Pa]
$\mathcal{P}$	channel perimeter [m]
Pr	Prandtl number [-]
q''	heat flux [W/m^2]
Q_{in}	cycle heat input rate [W]
Q_{out}	cycle heat output rate [W]
$\mathbf{R}$	Universal gas constant [J/kg mole K]
Re	Reynolds number [-]
R	radius [m]
s	entropy [J/kg K]
S	Suppression factor in Chen's correlation [-]
Sc	Schmidt number [-]
Sh	Sherwood number [-]
T	temperature [K]
t^*	characteristic surface renewal time period [s]
U	velocity [m/s]
v	specific volume [m^3/kg]
We	Weber number [-]
W_p	pump work rate [W]
x	quality [-]
x_n	mass fraction of noncondensible in the gas phase [-]
X	mole fraction [-]

X_{tt}	Martinelli factor [-]
Y	column vector as defined in Equation (40)
z	axial coordinate [m]

Greek

α	void fraction : thermal diffusivity [-] : [m^2/s]
Γ	phase change mass flow rate, per unit mixture volume [kg/m^3]
δ	film thickness [m]
ε	error tolerance [-]
θ	angle of inclination with respect to the horizontal plane [-]
μ	dynamic viscosity [N s/m^2]
ν	kinematic viscosity [m^2/s]
ξ	regime interpolation parameter [-]
ρ	density [kg/m^3]
σ	surface tension [N/m]
Φ	Two-phase friction coefficient multiplier [-]

Superscripts

"	flux
*	corresponding to vapor partial pressure
T	transpose
$\cdot$	high mass transfer

Subscripts

ann	annular regime
B	bubble
C	forced convection
cond	condensation
cr	critical
D	droplet
disp	dispersed regime
evap	evaporation
f	saturated liquid
g	saturated vapor
G	gas phase
h	homogenous
i	interface
J	annular jacket
L	liquid phase
m	mixture
n	noncondensible
NB	nucleate boiling
sat	saturation
T	tube
tot	total
v	vapor
WG	wall gas

WL	wall liquid
WM	wall mixture